Unclassified

SECURITY CLASSIFICATION OF THIS PAGE (When Data Entered)

REPORT DOCUMENTATION PAGE

READ INSTRUCTIONS
BEFORE COMPLETING FORM

1. REPORT NUMBER
IIHR Report No. 305

2. GOVT ACCESSION NO.

3. RECIPIENT'S CATALOG NUMBER

4. TITLE (and Subtitle)
Computation of Viscous Flow Around Propeller-Shaft Configurations

5. TYPE OF REPORT & PERIOD COVERED
Technical Report
March 1985 - December 1986

6. PERFORMING ORG. REPORT NUMBER
IIHR Report No. 305

7. AUTHOR(s)
Frederick Stern, Hyoung-Tae Kim, Virendra C. Patel, and Hamn-Ching Chen

8. CONTRACT OR GRANT NUMBER(s)
N00014-85-K-0347

9. PERFORMING ORGANIZATION NAME AND ADDRESS
Iowa Institute of Hydraulic Research
The University of Iowa
Iowa City, Iowa 52242

10. PROGRAM ELEMENT, PROJECT, TASK AREA & WORK UNIT NUMBERS
432a - 002

11. CONTROLLING OFFICE NAME AND ADDRESS
Office of Naval Research
800 North Quincy Street
Arlington, Virginia 22217

12. REPORT DATE
December 1986

13. NUMBER OF PAGES
87

14. MONITORING AGENCY NAME & ADDRESS(if different from Controlling Office)
Office of Naval Research
536 South Clark Street
Chicago, Illinois 60605

15. SECURITY CLASS. (of this report)
Unclassified

15a. DECLASSIFICATION/DOWNGRADING SCHEDULE

16. DISTRIBUTION STATEMENT (of this Report)
Approval for Public Release; Distribution Unlimited

17. DISTRIBUTION STATEMENT (of the abstract entered in Block 20, if different from Report)

18. SUPPLEMENTARY NOTES

19. KEY WORDS (Continue on reverse side if necessary and identify by block number)
Propellers, Propeller-Hull Interaction, Partially-Parabolic Equations, Computational Fluid Dynamics

20. ABSTRACT (Continue on reverse side if necessary and identify by block number)

A recently developed method for predicting propeller-hull interaction, in which a numerical method for calculating the viscous flow over the stern and in the wake of a ship is coupled with a propeller-performance program in an interactive and iterative manner to predict the combined flow field, is validated by performing comparisons between computational results and extensive available experimental data for propeller-shaft configurations. The steady-flow results are in excellent agreement with the data and show that the present

DD FORM 1 JAN 73 1473 EDITION OF 1 NOV 65 IS OBSOLETE
S/N 0102-LF-014-6601

Unclassified

SECURITY CLASSIFICATION OF THIS PAGE (When Data Entered)

procedures are able to accurately predict many details of the flow field. The dependence of the flow field on propeller loading, including the formation of the hub vortex, and the influence of hub length, are accurately simulated. Also, the robustness of the solution procedure is demonstrated by performing calculations for off-design (large-loading) conditions. The unsteady-flow calculations, which simulate the fanning action of a rotating finite-bladed propeller and are in reasonable agreement with the experimental data, point out the difficulties of accurately resolving the complex blade-to-blade flow and the need for investigating alternative approaches.

COMPUTATION OF VISCOUS FLOW AROUND PROPELLER-SHAFT CONFIGURATIONS

by

F. Stern, H. T. Kim, V. C. Patel, H. C. Chen

Sponsored by
Office of Naval Research
Accelerated Research Initiative (Special Focus) Program
in Propeller-Hull Interaction
Contract No. N00014-85-K-0347

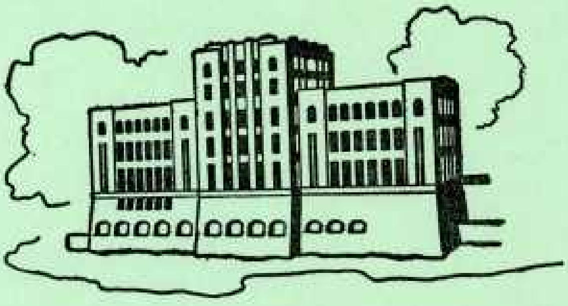

IIHR Report ~~No.~~ 305

Iowa Institute of Hydraulic Research,
~~The~~ University of Iowa
Iowa City, Iowa 52242

December 1986

Approved for Public Release: Distribution Unlimited

COMPUTATION OF VISCOUS FLOW AROUND PROPELLER-SHAFT CONFIGURATIONS

by

F. Stern, H. T. Kim, V. C. Patel, H. C. Chen

Sponsored by

Office of Naval Research
Accelerated Research Initiative (Special Focus) Program
in Propeller-Hull Interaction
Contract No. N00014-85-K-0347

IIHR Report No. 305

Iowa Institute of Hydraulic Research
The University of Iowa
Iowa City, Iowa 52242

December 1986

Approved for Public Release: Distribution Unlimited

ABSTRACT

A recently developed method for predicting propeller-hull interaction, in which a numerical method for calculating the viscous flow over the stern and in the wake of a ship is coupled with a propeller-performance program in an interactive and iterative manner to predict the combined flow field, is validated by performing comparisons between computational results and extensive available experimental data for propeller-shaft configurations. The steady-flow results are in excellent agreement with the data and show that the present procedures are able to accurately predict many details of the flow field. The dependence of the flow field on propeller loading, including the formation of the hub vortex, and the influence of hub length, are accurately simulated. Also, the robustness of the solution procedure is demonstrated by performing calculations for off-design (large-loading) conditions. The unsteady-flow calculations, which simulate the fanning action of a rotating finite-bladed propeller and are in reasonable agreement with the experimental data, point out the difficulties of accurately resolving the complex blade-to-blade flow and the need for investigating alternative approaches.

ACKNOWLEDGEMENTS

This research was sponsored by the Office of Naval Research, Accelerated Research Initiative (Special Focus) Program in Propeller-Hull Interaction, under Contract N00014-85-K-0347. The Graduate College of The University of Iowa provided a large share of the computer funds.

LIST OF SYMBOLS

Alphabetical Symbols

C_T	thrust loading coefficient (= $T/\frac{1}{2}\rho U_o^2 \pi R_p^2$)
$C_\mu, C_{\varepsilon 1}, C_{\varepsilon 2}$	turbulence model coefficients
D_p	propeller diameter
D_s	propeller shaft diameter
f	imposed frequency
$\underline{fb}$	body force per unit volume
G	turbulence generation term
$G(r)$	nondimensional circulation distribution (= $\Gamma(r)/\pi U_o D_p$)
G_θ	axial flux of tangential momentum
G_x	axial flux of axial momentum
J	advance coefficient (= U_o/nD_p)
K_T	thrust coefficient (= $T/\rho n^2 D_p^4$)
K_Q	torque coefficient (= $Q/\rho n^2 D_p^5$)
k	turbulent kinetic energy
L	body length
n	revolutions per second of propeller or shaft
p	pressure
Q	propeller torque
R	rotation parameter (= $\omega R_h/U_o$)
Re	Reynolds number (= $U_o L/\nu$)
R_{eff}	effective Reynolds number
R_h	propeller hub radius
R_p	propeller radius
S	swirl number (= $G_\theta/G_x R_p$)
S_i	inlet boundary of calculation domain
S_o	outer boundary of calculation domain
S_h	body surface
S_f	waterplane
S_w	wake centerplane
S_e	exit boundary of calculation domain
S_{ph}	propeller hub surface
T	propeller thrust

t	time
U,V,W	velocity components
U_{CL}	centerline velocity
U_{max}	maximum value of U profile at each station
U_τ	wall-shear velocity (= $(\tau_w/\rho U_o^2)^{1/2}$)
U_o	free-stream velocity
$\overline{uu}$, $\overline{vv}$, etc	Reynolds stresses
W_{max}	maximum value of W profile at each station
x,r,θ	cylindrical-polar coordinates
$x_s(r,\theta)$	x-coordinate of suction side of propeller blade
$x_p(r,\theta)$	x-coordinate of pressure side of propeller blade
y^+	dimensionless distance from the wall (= $\frac{U_\tau y}{\nu}$)

Greek Symbols

α_p	underrelaxation factor for pressure calculation
α_t	time underrelaxation factor
β	nondimensional frequency parameter (= $f\delta/U_o$)
δ	boundary-layer thickness
ε	rate of turbulent energy dissipation
$\theta_{le}(r)$	θ - coordinate of propeller leading edge
$\theta_{te}(r)$	θ - coordinate of propeller trailing edge
η_o	propeller open-water efficiency (= $JK_T/2\pi K_Q$)
ν	kinematic viscosity
ν_t	eddy viscosity
ρ	density
$\sigma_k,\sigma_\varepsilon$	turbulence model constants
τ_w	wall-shear stress
ω	propeller angular velocity

TABLE OF CONTENTS

I. INTRODUCTION

For practical reasons marine propellers are located at the stern of a ship; consequently, they operate in the thick stern boundary-layer and near wake. The flow field around the propeller-hull combination is unsteady, three dimensional, and turbulent. It is also interactive, insofar as the propeller-induced flow is dependent on the hull flow which is itself altered by the presence of the propeller. Historically, methods for the analysis of the propeller-induced flow and those for the hull boundary layer and wake have been developed separately with relatively little attention given to the interaction.

The propeller-induced flow is usually calculated under the assumption that the propeller operates in an infinite ideal fluid, but with a specified spatially varying potential inflow which represents the hull boundary layer and wake. Quite advanced inviscid-flow methods have been developed to implement this propeller theory. Consistent with the underlying assumptions of the theory, these methods have been found to perform best for uniform inflow conditions. A complete evaluation of the theory is made difficult by the lack of knowledge of the effective inflow which is usually assumed to be the nominal wake of the bare hull. In the absence of reliable methods for the prediction of the latter, recourse is had to model experiments in towing tanks. The flow over the stern and in the wake cannot be treated by the usual thin-boundary-layer equations and is influenced by both appendages and free-surface waves. The theoretical developments on this topic have generally focused on the bare hull and without the effects of the free-surface waves, and it is only very recently that the level of sophistication required for handling practical bare hull geometries has been reached.

Recently, the authors (Stern et al., 1985 and 1986), have taken a comprehensive approach in which methods of modern computational fluid dynamics have been brought to bear on the problem of propeller-hull interaction. The partially-parabolic method of Chen and Patel (1985) for calculating ship-stern flow has been coupled with a propeller-performance program in an interactive and iterative manner to predict the combined flow field. A body-force distribution is used to represent the propeller in the partially-parabolic method. The overall computational method is applicable to the most general situation of unsteady turbulent flow about propeller-driven three-dimensional bodies.

Some calculations for axisymmetric and three-dimensional bodies were reported in Stern et al. (1985, 1986). The latter reference also provided typical results for the simple geometry of a propeller-shaft configuration.

This report is concerned specifically with computations for propeller-shaft configurations. In this case, the upstream body is simply the propeller shaft. Although this is clearly an idealization of the practical circumstance, it will be shown that the flow field exhibits all the distinctive features of interest. Furthermore, the simplicity of the geometry makes it possible to identify and isolate the important features of the propeller-induced flow field. No doubt, it is for this reason that the most extensive experimental data that is available for propeller flow fields is for such a configuration.

II. COMPUTATIONAL METHOD

Consider the boundary layer and wake of a ship which is advancing at constant speed U_o under the action of a propeller rotating at constant angular velocity ω . The free-surface waves are ignored and the free surface is considered a plane of symmetry (zero-Froude-number approximation). The flow field may be divided into four regions, as depicted in figure 1. In region I, which is outside the boundary layer and wake, the flow is considered inviscid and irrotational. Region II contains the propeller. Region III is the thin boundary layer on the hull, and ends at a station x^* where the boundary-layer approximations are no longer valid. Region IV ($x > x^*$) includes the thick boundary-layer and wake. Herein, the primary focus is on region IV and the interactive analysis to obtain the combined propeller-hull flow field.

A. Method for Calculating Ship-Stern Flow.

In the thick boundary layer over the stern and in the wake the usual thin boundary-layer assumptions are no longer valid and the review of Patel (1982) indicates that the partially-parabolic Reynolds equations, in which only the streamwise diffusion terms are neglected, are more appropriate. The primary effect of an operating propeller on this flow field is to accelerate the fluid in the vicinity of the propeller in both the axial and tangential directions, and this reinforces the partially-parabolic assumptions. Recently, Chen and Patel (1985) have developed a method for solving the partially-parabolic equations. This method has been modified to include the effects of an operating propeller. The details of the basic method for bodies without a propeller have been provided by Chen and Patel (1985) and will not be reproduced here. However, for completeness, and to aid in understanding the necessary modifications and procedures for the incorporation of an operating propeller, a brief review is given below.

The method of Chen and Patel solves the transport equations for momentum, turbulent kinetic-energy k, and its dissipation-rate ε, in conjunction with the continuity equation, for the mean velocity components (U,V,W), pressure p, and turbulence parameters k and ε. The continuity equation and the five transport equations for (U,V,W,k,ε) are written in cylindrical polar coordinates (x,r,θ) in the physical domain as follows:

$$\frac{\partial U}{\partial x} + \frac{1}{r}\frac{\partial}{\partial r}(rV) + \frac{1}{r}\frac{\partial W}{\partial \theta} = 0 \qquad \text{(II-1)}$$

$$\frac{\partial U}{\partial t} + U\frac{\partial U}{\partial x} + V\frac{\partial U}{\partial r} + \frac{W}{r}\frac{\partial U}{\partial \theta} + \frac{\partial}{\partial x}(p + \overline{uu}) + \frac{\partial}{\partial r}(\overline{uv})$$
$$+ \frac{1}{r}\frac{\partial}{\partial \theta}(\overline{uw}) + \frac{\overline{uv}}{r} - \frac{1}{Re}\nabla^2 U + fb_x = 0 \qquad \text{(II-2)}$$

$$\frac{\partial V}{\partial t} + U\frac{\partial V}{\partial x} + V\frac{\partial V}{\partial r} + \frac{W}{r}\frac{\partial V}{\partial \theta} - \frac{W^2}{r} + \frac{\partial}{\partial x}(\overline{uv}) + \frac{\partial}{\partial r}(p + \overline{vv})$$
$$+ \frac{1}{r}\frac{\partial}{\partial \theta}(\overline{vw}) + \frac{\overline{vv}}{r} - \frac{\overline{ww}}{r} - \frac{1}{Re}\left(\nabla^2 V - \frac{2}{r^2}\frac{\partial W}{\partial \theta} - \frac{V}{r^2}\right) = 0 \qquad \text{(II-3)}$$

$$\frac{\partial W}{\partial t} + U\frac{\partial W}{\partial x} + V\frac{\partial W}{\partial r} + \frac{W}{r}\frac{\partial W}{\partial \theta} + \frac{WV}{r} + \frac{\partial}{\partial x}(\overline{uw}) + \frac{\partial}{\partial r}(\overline{vw})$$
$$+ \frac{1}{r}\frac{\partial}{\partial \theta}(p + \overline{ww}) + 2\frac{\overline{vw}}{r} - \frac{1}{Re}\left(\nabla^2 W + \frac{2}{r^2}\frac{\partial V}{\partial \theta} - \frac{W}{r^2}\right) + fb_\theta = 0 \qquad \text{(II-4)}$$

$$\frac{\partial k}{\partial t} + U\frac{\partial k}{\partial x} + V\frac{\partial k}{\partial r} + \frac{W}{r}\frac{\partial k}{\partial \theta} = \frac{\partial}{\partial x}\left(\frac{1}{R_{eff}}\frac{\partial k}{\partial x}\right)$$
$$+ \frac{1}{r}\frac{\partial}{\partial r}\left(\frac{1}{R_{eff}}\, r\frac{\partial k}{\partial r}\right) + \frac{1}{r^2}\frac{\partial}{\partial \theta}\left(\frac{1}{R_{eff}}\frac{\partial k}{\partial \theta}\right) + G - \varepsilon \qquad \text{(II-5)}$$

$$\frac{\partial \varepsilon}{\partial t} + U\frac{\partial \varepsilon}{\partial x} + V\frac{\partial \varepsilon}{\partial r} + \frac{W}{r}\frac{\partial \varepsilon}{\partial \theta} = \frac{\partial}{\partial x}\left(\frac{1}{R_{eff}}\frac{\partial \varepsilon}{\partial x}\right)$$
$$+ \frac{1}{r}\frac{\partial}{\partial r}\left(\frac{1}{R_{eff}}\, r\frac{\partial \varepsilon}{\partial r}\right) + \frac{1}{r^2}\frac{\partial}{\partial \theta}\left(\frac{1}{R_{eff}}\frac{\partial \varepsilon}{\partial \theta}\right)$$
$$+ C_{\varepsilon 1}\frac{\varepsilon}{k}G - C_{\varepsilon 2}\frac{\varepsilon^2}{k} \qquad \text{(II-6)}$$

with $\nabla^2 = \frac{\partial^2}{\partial x^2} + \frac{\partial^2}{\partial r^2} + \frac{1}{r}\frac{\partial}{\partial r} + \frac{1}{r^2}\frac{\partial^2}{\partial \theta^2}$

(x,r,θ) are the dimensionless coordinates with (x,r) normalized by a characteristic length L, and t is the time normalized by L/U_o. U,V,W are, respectively, the longitudinal, radial, and circumferential components of mean velocity normalized by the characteristic velocity U_o; p is the pressure normalized by ρU_o^2; $Re = U_o L/\nu$ is the Reynolds number defined in terms of U_o, L and molecular kinematic viscosity ν; the barred quantities $\overline{uu}$, $\overline{uv}$, etc. are the Reynolds stresses normalized by U_o^2; $\nu_t = c_\mu k^2/\varepsilon$ is the eddy viscosity; R_{eff} is the effective Reynolds number,

$$\frac{1}{R_{eff}} = \frac{1}{Re} + \frac{\nu_t}{\sigma_\phi} \qquad \text{(II-7)}$$

in which $\phi = k$ for the k-equation (II-5) and $\phi = \varepsilon$ for the ε - equation (II-6); and G is the turbulence generation term,

$$G = \nu_t \{2 [(\frac{\partial U}{\partial x})^2 + (\frac{\partial V}{\partial r})^2 + (\frac{1}{r}\frac{\partial W}{\partial \theta} + \frac{V}{r})^2] + (\frac{1}{r}\frac{\partial U}{\partial \theta} + \frac{\partial W}{\partial x})^2$$

$$+ (\frac{\partial V}{\partial x} + \frac{\partial U}{\partial r})^2 + (\frac{1}{r}\frac{\partial V}{\partial \theta} + \frac{\partial W}{\partial r} - \frac{W}{r})^2\} \qquad \text{(II-8)}$$

The terms $\underline{fb} = (fb_x, 0, fb_\theta)$ in the x- and z-momentum equations, respectively, are the components of the body force normalized by $\rho U_o^2/L$ which represent the influence of the propeller. These will be discussed subsequently in Section II.B.

In the two-equation k-ε turbulence model used in the present study, each Reynolds stress is related to the corresponding mean rate of strain by the isotropic eddy viscosity ν_t as follows:

$$-\overline{uv} = \nu_t (\frac{\partial U}{\partial r} + \frac{\partial V}{\partial x})$$

$$-\overline{uw} = \nu_t (\frac{\partial W}{\partial x} + \frac{1}{r}\frac{\partial U}{\partial \theta})$$

$$-\overline{vw} = \nu_t (\frac{1}{r}\frac{\partial V}{\partial \theta} + \frac{\partial W}{\partial r} - \frac{W}{r}) \qquad \text{(II-9)}$$

$$-\overline{uu} = \nu_t (2\frac{\partial U}{\partial x}) - \frac{2}{3} k$$

$$-\overline{vv} = \nu_t \left(2 \frac{\partial V}{\partial r}\right) - \frac{2}{3} k$$

$$-\overline{ww} = \nu_t \left(\frac{2}{r} \frac{\partial W}{\partial \theta} + 2 \frac{V}{r}\right) - \frac{2}{3} k$$

The model constants are:

$$C_\mu = 0.09,\ C_{\varepsilon 1} = 1.44,\ C_{\varepsilon 2} = 1.92,\ \sigma_k = 1.0, \text{ and } \sigma_\varepsilon = 1.3$$

In the present approach, the unsteady turbulent flow is treated by the so-called quasi-steady approximation insofar as the basic k-ε turbulence model derived from steady flows is retained. In other words, any direct interaction between the turbulence structure and the unsteadiness induced by the propeller, or its wake, is ignored. Little experimental or theoretical information is available at the present time to quantify this interaction for such complex flows. Generally, it is believed that the quasi-steady approximation is valid if the frequency parameter $\beta = f\delta/U_o$ (where f is the imposed frequency and δ is a characteristic boundary-layer thickness) is small compared to a characteristic turbulence frequency, such as the turbulent-burst frequency, which is of the order of .2. This has been observed experimentally for simple boundary layers with periodic external flows (Telionis, 1981; Cousteix, 1986). For the results to be presented, the value of the frequency parameter is $\beta \sim .03$, and therefore, a quasi-steady turbulence model appears to be justified, at least as a first approximation.

The governing equations (II-1) through (II-9) are transformed into numerically-generated, body-fitted, nonorthogonal, curvilinear coordinates such that the computational domain forms a simple rectangular region with equal grid spacing. The transformation is a partial one since it involves the coordinates only and not the velocity components (U,V,W). Referring to figure 1, for the general case of a three-dimensional body the specified boundaries of the solution domain are the hull surface S_h, the inlet plane S_i, the exit plane S_e, the symmetry planes S_w (wake centerplane) and S_f (waterplane), and the outer boundary S_o. The outer boundary is placed at a sufficiently large distance from the body so that uniform-stream conditions can be assumed there. This eliminates the need of both a potential-flow solution and a viscous-inviscid matching procedure. In other words, the solution domain encompasses regions I and IV of figure 1.

The transport equations are discretized using a staggered grid and the finite-analytic method which reduces numerical diffusion and instability as compared with more conventional methods. The velocity-pressure coupling is accomplished through the use of a two-step global pressure-correction procedure derived from the equation of continuity. The equations are written and solved in the unsteady form. For steady flow applications time simply serves as an underrelaxation iteration parameter.

The partially-parabolic assumption is made in the transformed coordinates; that is, second-derivatives of the transport quantities along the longitudinal coordinate are neglected. As a result of this assumption, only the pressure field p is fully elliptic and the velocity field is elliptic only in the transverse plane. A solution may be obtained by marching in the downstream direction if p is known or assumed; however, multiple global iterations are necessary for the influence of the downstream pressure to propagate upstream. The boundary conditions for a body without a propeller are as follows:

(1) on the inlet plane (S_i), (U,V,W,k,ε) are given from the thin boundary-layer (region III) and inviscid-flow (region I) solutions.

(2) on the outer boundary (S_o), the uniform-flow condition is applied, i.e., $U = U_o$, $W = k = \varepsilon = 0$.

(3) on the exit plane (S_e), a zero-pressure-gradient condition is applied, $\partial p/\partial x=0$.

(4) on the wake centerplane and waterplane symmetry planes (S_w and S_f), $W = 0$, $\frac{\partial}{\partial\theta}(U,V,k,\varepsilon) = 0$.

(5) on the body surface (S_h), a two-point wall-function approach is used to specify (U,V,W,k,ε).

For a body with a propeller the only other additional boundary condition required is that on the propeller hub S_{ph}: $W = \omega R_h$, where R_h is the hub radius. The hub boundary condition is applied by using the relative velocity in the "wall-function" approach used in the basic method. Thus, it is assumed that the log-law remains valid for a flow with a spinning boundary provided it is referenced to the boundary. This assumption is justified on the basis of the experiments of Lohmann (1976) even for large values of $\omega R_h/U_o$.

B. Representation of the Propeller and Interaction Procedure.

As discussed in Stern et al. (1985), there are a number of possible approaches for representing the propeller of region II in the partially-parabolic formulation of regions I and IV. In the present approach, the propeller is represented not by its actual physical presence but rather by a body-force distribution. In this approach, following Schetz and Favin (1977, 1979), and others, the influence of the propeller is accounted for by the addition of body force terms $\underline{fb} = \underline{fb}\,(x,r,\theta,t)$ in the source functions of the momentum equations (see equations (II-2) and (II-4)). It should be recognized that the body-force distribution is not a boundary condition but rather a discrete force field embedded in the flow field which represents the effects of the propeller. Modifications to the turbulence-model equations for the effects of the body force (or rotation) have not been made although, in principle, they can be readily introduced. The body-force distribution is obtained from the region II calculation for specified propeller geometry, operating conditions, and effective inflow velocities. The vortex-lattice lifting-surface method developed by Kerwin (Kerwin and Lee, 1978) for predicting propeller performance or more simple propeller models are used for this purpose. Since, in general, the body-force distribution depends on the effective inflow velocities (i.e., the viscous-flow solution) which, in turn, depends on the body-force distribution, the complete solution must be obtained iteratively.

The axial (fb_x) and the tangential (fb_θ) components of the body force are related to the propeller thrust T and torque Q as follows:

$$T(t) = \int_{R_h}^{R_p} \int_{\theta_{te}(r)}^{\theta_{le}(r)} \int_{x_p(r,\theta)}^{x_s(r,\theta)} fb_x \, dx r d\theta dr \qquad \text{(II-10)}$$

$$Q(t) = \int_{R_h}^{R_p} \int_{\theta_{te}(r)}^{\theta_{le}(r)} \int_{x_p(r,\theta)}^{x_s(r,\theta)} fb_\theta \; r dx r d\theta dr \qquad \text{(II-11)}$$

where the integration is over the volume of the propeller at its instantaneous position (see the List of Symbols for the definitions of the limits of integration). Equations (II-10) and (II-11) are the most general form appropriate for unsteady-flow simulations. For steady-flow simulation, it is more appropriate to use a distribution over a disc ($R_h \leq r \leq R_p$) of finite thickness (Δx), i.e.

$$T = 2\pi\Delta x \int_{R_h}^{R_p} fb_x \; r dr \qquad \text{(II-12)}$$

$$Q = 2\pi\Delta x \int_{R_h}^{R_p} fb_\theta \; r^2 dr \qquad \text{(II-13)}$$

Results have been obtained using both prescribed and interactive body-force distributions (Stern et al., 1985 and 1986). In the former case, the overall solution procedure is noniterative, i.e., the partially-parabolic solutions are carried out only once. This is because equations (II-10) and (II-11), or (II-12) and (II-13), are independent of the effective inflow. In the latter case, several iterations are required, on both the partially-parabolic and the propeller solutions, since $\underline{fb}$ depends on the effective inflow.

For the present investigation, only prescribed body-force distributions were used. The distributions are derived for conditions in which the propeller thrust coefficient C_T (or K_T), torque coefficient K_Q, speed of advance J, and radial circulation distribution $\Gamma(r)$ are known. In this case,

$$fb_x = \frac{C_T L\, R_p^2\, G(r)}{4\Delta x \int_{R_h}^{R_p} G(r)\, r dr} \qquad \text{(II-14)}$$

$$fb_\theta = \frac{4K_Q L\, R_p^3 G(r)}{\pi r J^2 \Delta x \int_{R_h}^{R_p} G(r)\, r dr} \qquad \text{(II-15)}$$

where L is the length of the body, and $G = \Gamma(r)/2\pi U_o R_p$. These distributions were derived assuming a lightly-loaded propeller.

III. FLOW GEOMETRY AND EXPERIMENTAL INFORMATION

The most basic geometry for the study of propeller-induced flow fields is a simple propeller-shaft configuration. This is because the underlying trailing-edge flow in the presence of a thin boundary layer is well documented, and consequently, it is possible to identify and examine in detail the important features of the propeller-induced flow field. Also, the most extensive experimental data that is available for propeller-induced flow fields is for this configuration. It is for these reasons that this geometry was selected for the present study.

Detailed laser-doppler velocimeter measurements of the flow field around propeller-shaft configurations have been made by Min (1978), Kobayashi (1981), Moyer and Billet (1982), Billet and Davis (1983), Okamura (1983), and Wang (1985). The latter reference is of particular interest since measurements were made for two distinctly different configurations: propeller P4660, which is a controllable pitch propeller from the DD963 class destroyer and has zero loading near the root; and propeller P4498, which is a research propeller and has finite loading near the root. P4660 has a larger hub ratio (.3) than P4498 (.2), and a lower pitch and camber at sections near the root. Steady, circumferentially-averaged, velocity profiles were obtained both in the immediate downstream vicinity of the propeller and in the near and intermediate wake regions. The most extensive steady-flow measurements are for design conditions. Some limited data was also obtained for off-design (large-loading) conditions and to investigate the influence of hub length. Unsteady, periodic, velocity measurements were also made in a plane immediately downstream of the propeller. Here again only limited experimental data are available. The focus of the experiments was on the formation of the hub vortex and its relationship to the loading characteristics near the root. Also, numerical predictions of the propeller circulation distribution, using a modified version of the Greeley and Kerwin (1982) lifting-surface propeller program to include hub effects, were shown to be in good agreement with circulation distributions obtained from the measured swirl velocity component and Kelvin's circulation theorem.

Herein, results are presented and comparisons are made with the complete set of experiments by Wang (1985). Previously (Stern et al., 1986), only an overview of the results was given. Also, improvements have been made in the unsteady-flow calculations such that the solutions are fully converged and extensions have been made for off-design (large-loading) calculations. The body-force distributions used in performing the calculations are based on the propeller circulation distributions presented by Wang. First, in Sections IV.A and IV.B, results are presented for design conditions for P4660 and P4498, respectively. Second, in Section IV.C, the influence of hub length for P4660 at the design condition is investigated. Third, in Section IV.D, results are presented for P4660 for off-design (large-loading) conditions. Lastly, in Section V, results are presented for unsteady flow for P4660 at the design condition.

The calculation conditions were selected to simulate the experimental conditions as closely as possible. However, this was made somewhat difficult due to the lack of sufficient information for viscous-flow calculations, particularly with regard to the upstream flow (e.g., boundary-layer thickness). It should be noted that the present conditions differ somewhat from those used previously by Stern et al. (1986). Upon performing the calculations for the off-design condition, an error was discovered in Table 6.1 of Wang (1985): the heading for column 9 should read η_o and not K_Q. Wang (1986) has provided the correct values for K_Q and these have been used in the present calculations.

In the presentation of the results and the discussion to follow, all coordinates are nondimensionalized using the shaft length L, with x = 0 at the shaft nose, and velocities and pressure are normalized using the free-stream velocity U_o and fluid density. In many of the figures the radial coordinate is normalized by the propeller radius R_p, and denoted by Y (= r/R_p), and the axial coordinate is also normalized by R_p and referenced to the propeller plane.

IV. STEADY FLOW

The results to be presented in this section were obtained using the rotationally symmetric version of the more general three-dimensional partially-parabolic method described in Section II (i.e., $\partial/\partial\theta = 0$ in equations (II-1) through (II-9)). This is appropriate for steady (circumferentially-averaged) flow around an axisymmetric body fitted with a propeller. For the design-condition calculations the following conditions were employed:

for P4660: $C_T = .746$, $K_T = .279$, $K_Q = .065$, $J = .976$, $\omega = 300$ rpm,
for P4498: $C_T = .780$, $K_T = .242$, $K_Q = .052$, $J = .889$, $\omega = 900$ rpm.

Based on these, and assuming a shaft length L=2m and a water temperature of 15°C, the shaft-length Reynolds numbers for P4660 and P4498 were determined as $Re = U_o L/\nu = 2.7 \times 10^6$ and 8×10^6, respectively.

The calculations were performed on a Prime 9950 minicomputer and took about 30 minutes of cpu time for the without-propeller condition. The calculations were begun with a zero pressure initial condition for the pressure field. A time underrelaxation factor $\alpha_t = .3$ was used on the body and $.03 \leq \alpha_t \leq .3$ for the wake. A total number of 80 global sweeps were used in order to insure that the solution was fully converged. For the with-propeller condition a modification of the above procedure was required because the addition of the body-force terms in the momentum equations results in a major modification of the flow field and can induce instability during the iterative solution procedure. Therefore, in order to obtain converged solutions for the with-propeller condition, the calculations were performed in stages, starting with the no-propeller condition and building up to the final values of C_T and K_Q. In this procedure, the entire pressure field, as well as the inlet velocity and turbulence parameter distributions, were specified from the previous solution along with the increased values of K_Q and C_T. For the design-condition calculations, five stages were required for P4660 and nine stages were required for P4498. For the off-design condition, some further modifications were required as will be discussed in Section IV.D.

A. Propeller P4660.

A partial view of the numerical grid used in the calculations for P4660 is shown in figure 2. Referring to figures 1 and 2 for notation: the inlet boundary S_i is at $x_u = .55$; the exit boundary S_e is at $x_d = 16$; the outer boundary S_o is at $r_o = .4$; the first grid point off the body surface is located in the range $50 \leq y^+ \leq 80$ where $y+ = U_\tau y/\nu$, U_τ is the wall-shear velocity, and y is the distance from the body; the number of axial grid points is 85; and the number of radial grid points is 48. This is considered a fine grid insofar as the first grid point off the body surface is as close as is allowed in the wall-functions approach and a sufficient number of grid points is located in the viscous flow region in order to resolve it accurately. Turbulent flat-plate boundary-layer profiles were used to specify the initial conditions with the inlet boundary-layer thickness estimated to be $\delta = .006$.

Calculations were performed for conditions corresponding to the shaft with a fixed hub and no propeller, the shaft with a spinning hub and no propeller, and the shaft with a spinning hub and propeller. For the with-propeller condition, two different body-force distributions were used. These are shown in figure 3. Both of these were derived from the circulation distributions presented by Wang (1985) using the procedures described in Section II.B. One of these corresponds to results from the lifting-surface propeller program modified to include hub effects (PSF2-HUB) and the other corresponds to the measured swirl velocity component and Kelvin's circulation theorem. Note that there are some differences between the two body-force distributions, particularly near the hub.

Figures 4 and 7 provide an overview of the results without and with the propeller, respectively, through the variation of some properties in the longitudinal direction. Figure 5 shows the swirl velocity profile for the no-propeller condition at the hub apex (which is located at $x/R_p = 1.053$). Figure 6 shows some characteristics of the solutions in the far wake. Figure 8 shows radial distributions of the various quantities of interest at some representative sections both upstream and downstream of the propeller.

Before discussing the influence of the propeller on the flow field it is of interest to examine the characteristics of the basic flow, i.e., without the propeller. Referring to figure 4, it is seen that for the shaft with a fixed hub, the flow characteristics are consistent with a trailing-edge flow in the presence of a thin boundary layer. The solution indicates a weak viscous-inviscid interaction and the other usual features associated with such a flow. Although the flow on the shaft with a spinning hub shows similar characteristics, there are some important differences. We observe a decrease in pressure in the vicinity of the tail such that the pressure recovery in the wake occurs with an adverse as opposed to a favorable gradient; a large increase in the magnitude of the shear stress on the spinning portion of the hub; the generation of swirl ($W \neq 0$); and an increase in turbulence levels in the near and intermediate wake (not shown here). The axial and radial velocities showed only a minimal influence of spin. This is indicated by the insignificant change in the wake centerline velocity. Consistent with expectation, the influence of increasing the hub angular velocity ω is a larger decrease in pressure, a larger increase in the magnitude of the shear stress on the spinning portion of the hub, an increase in W_{max}, and only rather small changes in U_{CL}. Figure 5 shows a comparison of the swirl velocity profiles at the hub apex for three values of the rotation parameter $R = \omega R_h/U_o$ (= .97, 1.26, 1.8) with the experimental data. Note that the R is related to the advance ratio J by $R = \pi R_h/JR_p$. The calculations show an increase in both swirl magnitude and radial extent with increasing R. Also, the radial position of W_{max} increases. The experimental data are somewhat scattered and only roughly follow the calculated trends.

Swirling turbulent shear flows are classified as weak or strong depending on the magnitude of the rotation parameter R defined above, or a swirl number S, defined by the ratio of the axial flux of the tangential and axial momenta, i.e.

$$S = G_\theta/G_x R_p \qquad \text{(IV-1)}$$

where

$$G_\theta = \int_0^\infty (\rho UW - \rho\overline{uw})\, r^2 dr$$

$$G_x = \int_0^\infty (\rho U^2 + \rho\overline{uu} + (p-p_o))\, r dr$$

The rotation parameter is appropriate for shear driven flows such as the shaft with a spinning hub (no propeller) while the swirl number is more appropriate for jets (with R_p = nozzle radius) and propeller flows. For weak swirl, i.e., R (or S) << 1, the axial velocity is not appreciably affected by swirl. Reynolds (1962) has shown that the asymptotic forms for weakly swirling wakes and jets are identical to the nonswirling cases due to the fact that the swirl decreases more rapidly than the axial velocity or velocity defect (see the asymptotic laws summarized on figure 6). This has been confirmed experimentally for swirling jets (Rose, 1962) and for wakes (Liu, 1971). The present results are plotted in the format of the asymptotic velocity decay laws in figure 6, in which: D_s = shaft diameter, D_p = propeller diameter, $\Delta U_{CL} = U_o - U_{CL}$ is the centerline velocity defect, and $\Delta U_{max} = U_{max} - U_o$ is the velocity excess. It is seen that the axial velocity defect follows the $x^{-2/3}$ power and the swirl velocity decays as x^{-1}, as indicated by asymptotic analysis. Experimental studies indicate that the axial velocity defect (or excess) is decreased by swirl, presumably due to an increase in entrainment and mixing. It should be recognized that such behavior is related to the structure of turbulence; since, for laminar flow, the axial and swirl velocities develop independently. The present results with the fixed and spinning hub only roughly follow the experimental trend with regard to the dependence of the axial velocity defect (or excess) on the rotation parameter (or swirl number). This is presumably because the swirl is relatively small and the basic k-ϵ turbulence model used here does not explicitly contain any effects of rotation.

Next, the influence of the propeller is examined. Referring to figure 7, it is seen that, as expected from physical considerations, a major influence of the propeller is an increase in pressure across the propeller plane, which is associated with the propeller thrust, and a large decrease in pressure along the wake centerline, which is due to the large propeller-induced swirl velocity. The distribution of the wall-shear velocity U_τ on the body indicates an increase over both the fixed- and spinning-hub conditions due to the propeller. Also, a sharp decrease is seen at the propeller plane. The wake centerline velocity also indicates an increase over the no-propeller conditions and an overshoot, i.e., values greater than the freestream velocity, are observed. The swirl velocity, which is of course zero in the absence of a propeller and for the fixed-hub condition, attains quite large values just downstream of the propeller, but decays with downstream distance. Finally, we note that the pressure variations are quite sensitive to the body-force distribution. The results for the PSF2-HUB body-force, which has larger values of fb_θ and fb_x near the hub, indicate a larger reduction in pressure and wall-shear velocity and larger swirl velocities in the near wake, than the results for the experimental body force. It is believed that the latter is more accurate, since for this application, PSF2-HUB appears to overpredict the circulation near the hub.

Figure 8 shows the radial distributions of the axial, radial, and tangential velocity components (U,V,W), pressure (p), and turbulence parameters (k,ε) at various stations both upstream ($x/R_p<0$) and downstream ($x/R_p>0$) of the propeller. Shown on figure 8 are the results for the conditions corresponding to the shaft with a spinning hub and no propeller, and the shaft with a spinning hub and propeller, and for both the experimental and PSF2-HUB body-force distributions. Recall that the solution for the former condition is similar to the solution for the shaft with a fixed hub except for the previously noted differences. Note that $x/R_p = .28$ (figure 8d) is just downstream of the propeller trailing edge and $x/R_p = 1.053$ (figure 8m) is at the hub apex. Comparisons are made with the experimental data wherever possible. The experimental data is for the mean velocity components (U,V,W) only; the corresponding turbulence measurements were not made. We see that the calculations are in excellent agreement with the experimental data for all three velocity components (figures 8d-8r) although some differences are seen in the W profile.

In general, all the results are consistent with the previous discussion and with expectations from physical considerations. The calculations indicate a negligible influence of the propeller for $x/R_p = -2$ (figure 8a). However, the influence of the propeller becomes significant as the propeller plane is approached (figure 8b-8c). The U velocity component shows a large increase across the propeller plane and decays slowly. At $x/R_p = 10$, the overshoot is still large (figure 8s). The V velocity component decreases due to the propeller-induced flow contraction. Note that the shape of the V profile close to the propeller is dominated by the propeller loading characteristics (figures 8c-8e) whereas further downstream its shape is more affected by the shaft trailing edge and transition into the wake (figures 8f-8p). The V velocity component decays more rapidly than the U component. At x/R_p = 2.052 (figure 8r) the calculations indicate that $V \sim 0$; however, the experimental data indicate a slower decay such that V is small but nonzero at x/R_p = 2.052. The propeller-induced swirl W is negligible upstream of the propeller (figures 8a-8c) and is large in and downstream of the propeller plane (figures 8d-8s). The shape of the W profile indicates that the propeller-generated swirl and the hub-generated swirl initially develop independently but subsequently merge through the action of turbulent diffusion. This effect is due to the fact that P4660 has zero loading at the hub (see figure 3). The experimental data indicates basically no interaction and merging of the propeller and spinning-hub swirl velocities even as far downstream as x/R_p = 1.252 (figure 8o). This is rather surprising since, from physical considerations, a more rapid mixing would have been expected. The W velocity component also decays slowly but more rapidly than the U component.

The pressure profiles indicate a jump in pressure across the propeller plane. This is associated with the propeller thrust. Just upstream of the propeller (figure 8c) the pressure is reduced and just downstream (figure 8d) it is increased. The downstream increase decays and diffuses outward (figures 8e-8m). Downstream of the propeller near the hub and wake centerline there is a large decrease in pressure due to the large swirl velocity (figures 8g-8s). This effect can be explained with reference to the V-momentum equation (II-3). Near the propeller axis (small r) and for large W the radial pressure gradient $\partial p/\partial r$ is dominated by the $-W^2/r$ term. Note that the decay of pressure in the wake can be correlated with the swirl velocity profile.

In general, the influence of turbulent diffusion is such that the velocity components are smoothed and diffuse outward as the flow evolves into the wake (figures 8n-8t). The calculations indicate that the turbulence parameters k and ε are greatly increased in the wake over the values observed without a propeller, especially near the wake centerline in the near wake and all across the wake in the intermediate and far wake. As mentioned previously, no experimental data are available to verify the turbulence predictions. The limited experimental data that are available for other configurations (Ravindranath and Lakshminarayana, 1981; Schetz and Jakubowski 1975; Jessup et al., 1984; Kotb and Schetz, 1985) indicate an increase in turbulence due to the propeller. This increase is due both to the larger mean-velocity gradients in the with-propeller condition and to the turbulence production on the propeller blades. However, we note that only the former effect is included in the present calculations.

The velocity components in the far wake with the propeller are also shown on figure 6. Here again, the correct asymptotic forms are recovered. Note that the swirl number calculated at $x/R_p = .28$ is $S = .12$. The fact that a propeller wake decays at the same rate as the nominal wake of a bare body has been confirmed experimentally by Aron (1960). However, we note that the analysis of Reynolds (1962) indicates that a momentumless swirling wake (the practical circumstance) decays at different rates than the condition considered here (figure 6). This has not been confirmed experimentally.

B. Propeller P4498.

Calculations were performed for P4498 using two different grids, i.e., a fine and a coarse grid. As will be discussed subsequently, the reason for using a coarse grid is that it was not possible to make calculations for the with-propeller condition with the finer grid due to the large loading near the root of P4498. The two grids are shown in figures 9 and 10, respectively. Note that $x/R_p = .208$ is just downstream of the propeller trailing edge and $x/R_p = .84$ is the hub apex. The fine grid was very similar to that described earlier for P4660. In the coarse grid the first grid point off the body surface was located in the range $170 \leq y^+ \leq 220$; the number of axial grid points was 70; and the number of transverse grid points was 40.

The initial and flow conditions for the P4498 calculations are similar to those described earlier for P4660. This is also true for the derivation of the body-force distributions which are shown in figure 11. The very different characteristics of the body-force distributions for P4660 and P4498 are evident from a comparison of figures 3 and 11. In particular, P4498 has finite and large values of fb_x and fb_θ at the root. Note that for this case the differences between the experimental and PSF2-HUB body-force distributions are minimal. The format for the presentation of the results for P4498 is similar to that described earlier for P4660. Also, many aspects of the two solutions are similar and will not be discussed again. The focus of the discussion to follow is on the differences between the two solutions.

A comparison of figures 12 and 7 shows that the drop in the pressure for P4498 is considerably larger than for P4660. This is the result of the increased swirl velocities for P4498, the maximum swirl velocity at the hub apex being almost twice as large than for P4660.

A comparison of figures 13 and 8 shows the differences in the detailed solutions for the two propellers. In this case the experimental data is restricted to the swirl velocity component only. Of particular interest is the development of the swirl velocity component which is quite different from that shown previously for P4660. For P4498 the propeller generated swirl and the spinning-hub generated swirl do not develop independently, but interact such that a large hub vortex is formed at the hub apex (figure 13j). Also, the axial velocity component for P4498 is much fuller near the root than for P4460. These effects are a direct result of the differences in the loading distributions. Note that the calculated swirl number at x/R_p = .208 is S = .12.

As mentioned previously, the results with the P4498 propeller were obtained using the coarser grid. Calculations were made using both grids for the spinning-hub condition. Results from both these calculations are shown on figure 14. It is seen that the coarse-grid solution leads to a large under prediction of the maximum swirl velocity and to an overprediction of the radial extent. Note that both solutions predict a considerably slower decay in the near wake (x= 1.307) than the experiment. Thus, if it had been possible to obtain a fine-grid solution with the propeller for P4498, it is expected that an even closer agreement with the experimental data would have resulted. The difficulties associated with the fine-grid solution for P4498 can be attributed to the use of "wall-functions" in the turbulence model. The present results underscore the need for further work on near-wall turbulence modeling in order to resolve the details of the solution in this region. Lastly for P4498, figure 15 shows the influence of rotation parameter for the spinning-hub condition. The swirl velocity profile at the hub apex is compared for three values of R (= .52, .73, .87). The calculations show similar trends as those discussed previously for the P4660 shaft-hub configuration (see figure 5). Also, just as was the case previously, the experimental data is somewhat scattered and only roughly follow the calculated trends. Note that the radial extent of swirl is greater for the P4660 shaft-hub configuration than P4498 due the larger values of rotation parameter R.

C. Influence of Hub Length.

Calculations were also performed for P4660 at the design condition and with a medium and long hub. The previous results, discussed in Section IV.A, are for a short hub. Partial views of the grids used in the calculations for the medium and long hubs are shown in figures 16 and 17, respectively. These are very similar to those described earlier for P4660 and shown in figure 2. Also, the initial and flow conditions, as well as the body-force distributions, were the same as before.

First, the influence of hub length on the solutions without the propeller are examined. Referring to figures 4, 18, and 19, which are for the short, medium, and long hubs, respectively, it is seen that for a shaft with a fixed hub, the influence of increasing hub length is to reduce the viscous-inviscid interaction. As the hub length is increased, the body curvature near the tail is reduced, resulting in smaller variations in pressure, and a more gradual reduction in U_τ associated with the thickening of the boundary layer. The wake centerline velocity is not influenced by changes in hub length. The influence of increasing rotation parameter for the medium and long hubs is identical to that described previously for the short hub. The influence of increasing hub length is only a slight reduction in the minimum pressure, the maximum U_τ, and the maximum swirl velocity. Figures 20 and 21 show a comparison of the swirl velocity profiles at the hub apex for two values of the rotation parameter R (= .97, 1.8) and for the medium and long hubs, respectively. The trends are indentical to those described previously for the short hub with reference to figure 5.

Second, the influence of hub length on the solutions for the with-propeller condition is examined. Referring to figures 7, 22, and 24, it is seen that in this case, the influence of increasing hub length is a further reduction in pressure in the near wake, a reduction in U_{CL} in the near wake, and a slight increase in W_{max} in the near wake. These effects are probably due to the increase in the length of the development of the boundary-layer flow downstream of the propeller for the longer hubs.

Lastly, figures 23 and 25 show the solution profiles at two stations downstream of the propeller for the medium and long hubs, respectively: x/R_p = .28 which is just downstream of the propeller trailing edge, and x/R_p = 1.616 and 2.577 for the medium and long hubs, respectively, which corresponds to the hub apex. These figures should be compared with the corresponding ones for the short hub shown in figures 8d and 8m, respectively. The trends shown on figures 23 and 25 are consistent with the previous discussions. Note that the comparison with the experimental data for the swirl velocity profile is not quite as good as that shown previously for the short hub. This is due to the fact that the body-force distributions used for the medium and long hubs are the same as those used previously for the short hub and are probably not accurate.

D. Off-Design Conditions.

Results are now presented for P4660 for off-design (large-loading) conditions. Although only limited experimental data are available for verifying the results and, as will be discussed subsequently, the accuracy is severely limited, such calculations are useful for demonstrating the robustness of the computational approach.

The open-water characteristic curves for P4660 are shown in figure 26 (Wang, 1986). The previous results were for the design condition, which is $J = .976$. For the off-design condition calculations, the following were employed:

$$C_T = 1.82,\ K_T = .402,\ K_Q = .0894,\ J = .750,\ \omega = 820,$$
$$C_T = 4.75,\ K_T = .522,\ K_Q = .1126,\ J = .529,\ \omega = 790.$$

The $J = .75$ condition is moderate loading whereas $J = .529$ represents a very heavily-loaded condition. The body-force distributions for $J = .529$ were derived as discussed previously and are shown on figure 27. Note that PSF2-HUB predicted substantially larger values of circulation near the propeller tip than those obtained from the measurements which accounts for the differences shown on figure 27. As discussed by Wang (1985), the measured circulation may be inaccurate due to the low data density at this high ω. Thus, the body-force distributions derived from the experiments may not be accurate. Additional inaccuracies may also result from the use of definitions (II-14) and (II-15) which were derived under the assumption of a lightly-loaded condition. Wang did not provide circulation distributions for $J = .75$. The body-force distributions shown for $J = .75$ were derived using the measured circulation distribution for $J = .529$ in equations (II-14) and (II-15) along with the correct values of C_T, K_Q, and J. A comparison of figures 3 and 27 shows that for reduced J the propeller loading is substantially increased, including larger values near the root for both fb_θ and fb_x.

Some further modifications of the basic partially-parabolic method from those described previously were required for performing the off-design condition calculations. This is because the specification of large values of fb_θ can lead to numerical instability, especially in the near-wake region, unless corrective measures are taken. In order to obtain convergent solutions the following procedures were investigated: (1) different types of source term linearization; (2) underrelaxation in the momentum, pressure-correction, and pressure equations; (3) changing the sequence of solving the momentum equations from U then V then W to U then W then V; and (4) using improved initial conditions, i.e., specifying the entire pressure (p), velocity (U,V,W), and turbulence parameter (k,ε,ν_t) fields from the previous solution along with the increased values for C_T and K_Q, while building up the solution in stages from lower to the final values of C_T and K_Q. The first two procedures allowed for calculations to be made for J = .75 whereas the basic program with the previously described modifications failed for J = .85. Both procedures three and four allowed for further reduction to J = .529. The two solutions showed some differences. In particular, procedure three predicted somewhat larger swirl velocities and lower wake centerline pressure in the near wake than procedure four. 16 stages were required to obtain the J = .529 solution using procedure four, and 17 with procedure three. Only the results from procedure four will be presented. Also, most of the results shown are for the experimental body-force distribution; since, the results for the PSF2-HUB body-force distributions were quite similar except for the swirl velocity profile at the outer propeller radii. Both results for the swirl velocity profile are shown for comparison.

A comparison of figures 28 and 7 shows the very large influence of large loading on the solution. For J = .529, it is seen that: the near-wake centerline pressure is reduced by almost an order of magnitude; the wall-shear velocity increases; the wake centerline velocity shows an overshoot of 2.4 in the very near wake followed by a rapid reduction to 1.6 at x = 1.5, a slight increase to 1.75 at x = 2.0, and finally a monotonic decrease to the freestream value; and the maximum swirl velocity in the near wake is increased by a factor of three. The large reduction in wake centerline pressure is a direct result of the increased swirl velocities, and is responsible for the previously described wake centerline velocity behavior which can be explained as follows: for J = .976 (figure 7), the initial wake centerline velocity increase is due to the effects of the initial favorable pressure gradient whereas the subsequent increase is due to turbulent diffusion (the $\partial \overline{uv}/\partial r$ term in equation (II-2)) which dominates over the effects of the subsequent adverse pressure gradient; for J = .75 and .529, the wake centerline velocity is affected both by the initial favorable (large overshoot) and subsequent adverse (large decrease) pressure gradients with turbulent diffusion not dominating until x > 1.5. Note that the swirl numbers calculated at x/R_p = .28 for J = .75 and .529 are S = .21 and .28, respectively. Swirling jet studies indicate reversed flow for S = .6 (Gupta et al., 1984).

Figure 29 shows the solution profiles at the propeller trailing edge (x/R_p = .28) and the hub apex (x/R_p = 1.053). A comparison of figure 29 with the corresponding ones in figure 8 (figures 8d and 8m) again shows the very large influence of increased loading on the solution. In particular, we note the following features: the overshoot in the U profile is increased by a factor of 2 (for J = .529) and is much fuller near the wall due to the finite root loading; the V profile minimum and W profile maximum are increased by a factor of 3 (for J = .529); the predicted swirl velocities are larger than the measured ones; consistent with figure 28 there is a large reduction in pressure; and the turbulence parameters show a large increase.

A part of the discrepancy between the predicted and measured swirl velocity can be attributed to experimental error. As pointed out previously, there were difficulties in the experiments for this large ω which may have affected the measurement of the swirl velocity profile and the subsequent calculation of circulation. Results are also shown on figure 29 for the swirl velocity profile obtained using the PSF2-HUB body-force distribution. Note the significant decrease in W for the outer radii due to the larger circulation predicted by PSF2-HUB near the tip than that obtained from the measurements.

V. UNSTEADY FLOW

The calculations presented and discussed in Section IV were for steady flow and neglect the effects of the individual blades and their rotation. In other words, the previous results correspond to an infinite-blade actuator disk representation of the propeller. In this section extension of the previous procedures for unsteady flow are discussed and results are presented for the design condition for propeller P4660. There are two principal effects due to a rotating finite-bladed propeller: (1) the fanning action of the propeller induces an oscillating pressure field all around the propeller; and (2) a complex periodic blade-to-blade flow field, including the individual blade boundary layers and wakes, is created in the near wake of the propeller. The former effect is responsible for propeller-induced hull vibration. The latter effect is important for the prediction of propeller noise and the details of the propeller slip stream. As will now be shown, only the former effect can be simulated with a body-force distribution for unsteady flow.

Recall that the basic viscous-flow solution method described in Section II is applicable to unsteady three-dimensional flow. This most general version which solves the complete equations (II-1) through (II-9) is required for unsteady-flow simulations. However, since this was the first application of this method for unsteady flow some modifications were required. First, in order to obtain fully converged unsteady-flow solutions a true iteration parameter was introduced and the use of time for this purpose was removed. Second, the specifications of the boundary conditions in the transverse plane required modification from the previously used symmetry conditions on the waterplane and keel. If the upstream flow is axisymmetric, as in the present application, then periodic boundary conditions are appropriate at blade spacing intervals.

In general, for unsteady flow, the body-force distributions are distributed over the volume of the propeller at its instantaneous position and are time dependent as indicated by equations (II-10) and (II-11). However, consistent with the axisymmetric inflow and the periodic boundary conditions used in the present application, the appropriate body-force distributions are independent of time but are imposed over the instantaneous position of the propeller blade. In other words, a rotating, constant strength, body-force distribution is used. Calculations were performed using both a coarse and a fine cross-sectional grid and propeller representation. It should be recognized that the propeller representation and the number of time steps per period are dependent on the cross-sectional grid spacing. In the case of the coarse cross-sectional grid, the propeller was represented by a single radial body-force distribution (see figure 30), and only three time steps per period were used. In the case of the fine cross-sectional grid, the propeller was represented by four radial body-force distributions (see figure 31), and six time steps per period were used. In both cases, the radial body-force distributions were based on the experimental circulation distribution as previously described (see figure 3). In the latter case, the chordwise loading was distributed based on the NACA .8 mean line.

The convergence of the solution for unsteady flow is influenced not only by the number of time steps per period but also by the number of global iterations per time step used in the partially-parabolic method, and the total number of periods calculated. Presently, 15 global iterations per time step and a total number of 12 periods (i.e., 37 time steps) have been used for the coarse cross-sectional grid and only 2 periods for the fine cross-sectional grid. The coarse cross-sectional grid solution is fully converged. However, the fine cross-sectional grid solution is not due to the limited number of periods calculated. Most of the results to be presented are for the coarse cross-sectional grid since they are sufficient to demonstrate the characteristics of an unsteady-flow simulation. Some limited results are presented to show the effects of the fine cross-sectional grid.

The initial and flow conditions used for the unsteady calculations were identical to those described earlier for steady flow and for the design condition. The radial grid distribution was somewhat coarser than that used for the steady-flow calculations (see figure 2) but similar to that described earlier for P4498 (see figure 10).

Figure 32 shows the body surface and wake centerline pressure distribution, and wall-shear, wake centerline, and maximum swirl velocities obtained at the 32nd time step and for all three grid lines over one blade spacing interval (i.e., one period). These are to be compared with the corresponding steady-flow results shown in figure 7. The unsteady solution shows distinct characteristics at each of the grid lines over the blade spacing interval: for grid line 2, the propeller is in the "right on" position, and its influence is maximum , i.e., the flow field variations are larger than the steady-flow solution; for grid line 3, the propeller has "not arrived" yet and the results are closer to the no-propeller solution; and for grid line 1, the propeller has "just passed" and the solution shows a residual influence of the propeller.

Figure 33 shows the radial distributions of (U,V,W,p,k,ε) at some representative stations both upstream and downstream of the propeller. The results shown are for grid line 2 and include all time steps except the first 3 (i.e., first period). The corresponding results for steady flow are shown in figure 8. The results in figure 33 clearly show the influence of blade position as described in reference to figure 32. Note that the solution is fully converged, i.e., although all periods are shown except the first, only three curves appear on each figure. Of particular interest, is the extent of the unsteady-flow effects. It is seen that upstream of the propeller the unsteady-flow effects are small. For $x/R_p = -1.$, the unsteady-flow effects cannot be discerned (figure not shown). As the propeller plane is approached $x/R_p = (-.5, -.25)$, only a gradual increase in unsteady-flow effects occurs. Very near the propeller plane ($x/R_p = .04$) and in the immediate slip stream $.0 < x/R_p < 1.$, the unsteady-flow effects are large. For $x/R_p > 1.$, the effects again become small. For $x/R_p = 2.$, the effects cannot be discerned (figure not shown). Thus, the present simulation indicates that the unsteady-flow effects are limited to $-1 \lesssim x/R_p \lesssim 2$. Although Wang's (1985) unsteady-flow data are not extensive enough to confirm this, the earlier MIT experiments of Min (1978) and Kobayashi (1981) seem to indicate a similar extent (excluding the tip vortex).

Figure 34 shows the time history of the velocity components (U,V,W) at $x/R_p=.28$ for two radial positions $Y=r/R_p=(.417, .833)$ and for grid line 2. Results are shown for both the coarse and the fine cross-sectional grid solutions. The results for the coarse cross-sectional grid correspond to the last complete propeller revolution (i.e., last 5 periods). Also shown for comparison are the experimental results. A blade angle coordinate $\theta = \omega t$ measured from the generator line of the key blade has been used instead of time for the abscissa. Referring to figures 30 and 31, $\theta = 0$ corresponds to the key blade at grid line 1. It is believed that the experimental blade angle is approximately consistent with this; however, it was not possible to confirm the experimental blade angular coordinate. Consistent with the steady-flow predictions, the mean values are well predicted; however, there are large differences in both the magnitude and phase of the unsteady component. This is especially true for the radial V component. Note the differences between the coarse and fine cross-sectional grid solutions. The fine cross-sectional grid solution is clearly a more detailed representation and is somewhat closer to the experimental trends. The trends shown by the calculations have already been described with reference to figure 32. The rotating body-force representation of the propeller simulates the thrust and torque characteristics of the rotating blades but is unable to capture all of the details of the complex blade-to-blade flow seen in the experimental data just downstream of the propeller trailing edge. The experimental data reveal many interesting features of the blade-to-blade flow, including radial variations resulting from the effects of the propeller loading, blade wakes, and tip vortices. In order to predict such effects a more detailed representation of the propeller is required.

These unsteady-flow calculations were also performed on the Prime 9950 minicomputer and took about 2 hours of cpu time per period for the coarse cross-sectional grid solution and 4.5 hours per period for the fine cross-sectional grid. Time relaxation was of course not used, but a relaxation factor of $\alpha_p = .3$ was used for the pressure in the wake.

VI. CONCLUDING REMARKS

A recently developed method for predicting propeller-hull interaction has been validated by performing comparisons between computational results and extensive available experimental data for propeller-shaft configurations. The steady-flow results are in excellent agreement with the experimental data and show that the present procedures are able to predict most of the details of the mean flow field. The dependence of the flow field on propeller loading, including the formation of the hub vortex, and the influence of hub length are accurately simulated. Also, the robustness of the present approach has been demonstrated by performing calculations for off-design (large-loading) conditions, including an extremely large-loading case. The results for the off-design conditions are quite realistic, but show differences from the experiments. It is believed that a large part of the descrepancy can be attributed to the difficulties in the experiments for large propeller angular velocities.

Based on the results from the present investigation and those obtained previously for rotationally-symmetric flow for DTNSRDC afterbody 1 and for three-dimensional flow for DTNSRDC 3:1 elliptical body, it is concluded that the present procedures can accurately simulate the steady part of the combined propeller-hull flow field and can be used with some confidence for predictions of thrust deduction and effective wake, as well as other flow quantities of interest.

Of course, much more work needs to be done, especially for three-dimensional flow, to extend the method to realistic ship geometries. Some of the issues that need to be addressed are as follows: optimum grid generation techniques in order to resolve the flow field for complex geometries including propeller-induced effects; improved turbulence modeling procedures, especially in the near-wall region; and the influence and interaction between the propeller-hull flow field and appendages such as the rudder.

The unsteady-flow results obtained with the rotating body-force representation of the propeller simulate the fanning action of a rotating finite-bladed propeller. Such a simulation should be useful for investigations of propeller-induced hull vibration. Note that methods for predicting unsteady cavitation (e.g., Stern, 1982) could be incorporated into the present procedures without too much difficulty to allow for the inclusion of this important influence on propeller-induced hull vibration. The comparison between the present results and the experimental data just downstream of the propeller trailing edge point out the limitations of the present approach for simulating the complex blade-to-blade flow. A more detailed representation of the propeller than the body force is required. Two alternative approaches need to be investigated. The first, is the velocity-field interaction method as described by Stern et al. (1985), which is similar to the present approach, in that different methods are used for the propeller and viscous flow and the complete solution is obtained iteratively and interactively. The second, is the development of a method in which the actual propeller is embedded in a viscous-flow method and the no-slip condition is satisfied on the surface of the rotating blades. It should be recognized that both of these approaches will involve substantial computer times and the use of a supercomputer. Also, some critical issues that need to be addressed in the latter approach are grid generation techniques such as the use of rotating grids as well as turbulence modeling and flow field resolution considerations.

Validation of the computational results is made difficult by the lack of detailed experimental data for combined propeller-hull flow fields. This is especially true for turbulence quantities, the slipstream velocity field, and the entire flow field for three-dimensional bodies. Of particular interest are detailed measurements of both the velocity and turbulence profiles upstream and downstream of the propeller, including mean and phase-averaged values. Special attention should be given to the flow in the immediate vicinity of the propeller in order to explicate the nature of the unsteady flow and the evolution of the blade wakes in the propeller slipstream. An experimental project is also underway at the Iowa Institute of Hydraulic Research in cooperation with the Universities of Osaka and Osaka Prefecture of Japan with the goal of obtaining such data.

REFERENCES

Aron, A., (1960), "Decay of Turbulent Wakes Behind a Propeller", M.S. Thesis, Dept. of Mech. and Hydraulics, University of Iowa.

Billet, M.L. and Davis, T.J., (1983), "Propeller Velocity and Pressure Field Measurements - Part II", ARL/PSU TM 83-174.

Chen, H.C. and Patel, V.C., (1985), "Calculation of Trailing-Edge, Stern and Wake Flows by a Time-Marching Solution of the Partially-Parabolic Equations", Iowa Inst. Hydraulic Research, IIHR Report No. 285.

Cousteix, J., (1986), "Three-Dimensional and Unsteady Boundary Layer Computations", Annual Review of Fluid Mechanics, Vol. 18, pp. 173-196.

Greeley, D.S. and Kerwin, J.E., (1982), "Numerical Methods for Propeller Design and Analysis in Steady Flow", Trans. SNAME, Vol. 90, pp. 415-453.

Gupta, A.K., Lilley, D.G., and Syred, W., (1984), "Swirl Flows", Abacus Press, Tunbridge Wells, England.

Jessup, S.D., Schott, C., Jeffers, M., Kobayashi, S., (1984), "Local Propeller Blade Flows in Uniform and Sheared Onset Flows Using LDV Techniques", Proc. 15th ONR Sym. Naval Hydrodynamics, Hamburg, pp. 221-237.

Kerwin, J.E. and Lee, C.S., (1978), "Prediction of Steady and Unsteady Marine Propeller Performance by Numerical Lifting-Surface Theory", Trans. SNAME, Vol. 86, pp. 218-253.

Kobayashi, S., (1981), "Experimental Methods for the Prediction of the Effect of Viscosity on Propeller Performance", MIT, Dept of Ocean Eng., Report No. 81-7.

Kotb, M.A. and Schetz. J.A., (1986), "Measurements of Three-Dimensional Turbulent Flow Behind a Propeller in a Shear Flow", AIAA Journal, Vol. 24, pp. 570-577.

Liu, C.-Y., (1971), "Wake of an Axially Symmetrical Body With Spinning", Proc. 9th Int. Symp. on Space Tech. and Sci., Tokyo, p. 373.

Lohmann, R.P., (1976), "The Response of a Developed Turbulent Boundary Layer to Local Transverse Surface Motion", Trans. ASME, J. Fluids Eng., Vol. 98, pp. 354-363.

Min, K.S., (1978), "Numerical and Experimental Methods for the Prediction of Field Point Velocities Around Propeller Blades", MIT, Dept. of Ocean Eng., Report no. 78-12.

Moyer, R.S. and Billet, M.L., (1982), "Propeller Velocity and Pressure Field Measurements - Part 1", ARL/PSU TM 82-240.

Okamura, N., (1983), "Experimental Analysis of the Flow Field Around a Screw Propeller", IHI Eng. Review, Vol. 16, No. 4.

Patel, V.C., (1982), "Some Aspects of Thick Three-Dimensional Boundary Layers", Proc. 14th ONR Sym. Naval Hydrodynamics, Ann Arbor, pp. 999-1040.

Ravindranath, A. and Lakshminarayana, B., (1981), "Structure and Decay Characteristics of Turbulence in the Near and Far-Wake of a Moderately Loaded Compressor Rotor-Blade", ASME, J. Eng. Power, Vol. 103, pp. 131-140.

Reynolds, A.J., (1962), "Similarity in Swirling Wakes and Jets", J. Fluid Mech., Vol. 14, p. 241.

Rose, W.G., (1962), "A Swirling Round Turbulent Jet", J. Appl. Mech., Vol. 29, p. 616.

Schetz, J.A. and Jakubowski, A.K., (1975), "Experimental Studies of the Turbulent Wake behind Self-Propelled Slender Bodies", AIAA Journal, Vol. 13, pp. 1568-1575.

Schetz, J.A. and Favin, S., (1977), "Numerical Solution for the Near Wake of a Body with Propeller", AIAA, J. Hydronautics, Vol. 11, pp. 136-141.

Schetz, J.A. and Favin, S., (1979), "Numerical Solution of a Body-Propeller Combination Flow Including Swirl and Comparisons with Data", AIAA, J. Hydronautics, Vol. 13, pp. 46-51.

Stern, F., (1982), "Comparison of Computational and Experimental Unsteady Cavitation", Proc. 14th ONR Sym. Naval Hydrodynamics, Ann Arbor, MI, pp. 613-652.

Stern, F., Patel, V.C., Chen, H.C. and Kim, H.T., (1985), "The Interaction Between Propeller and Ship-Stern Flow", Proc. Osaka Int. Colloq. on Ship Visc. Flow, pp. 468-495.

Stern, F., Kim, H.T., Patel, V.C.and Chen, H.C., (1986), "Viscous-Flow Computations of Propeller-Hull Interaction", Proc. 16th ONR Sym. Naval Hydrodynamics, Berkely, CA.

Telionis, D.P., (1981), "Unsteady Viscous Flow", Springer-Verlag, New York.

Wang, M.H., (1985), "Hub Effects in Propeller Design and Analysis", MIT Dept. of Ocean Eng., Report no. 85-14.

Wang, M.H., (1986), private communication.

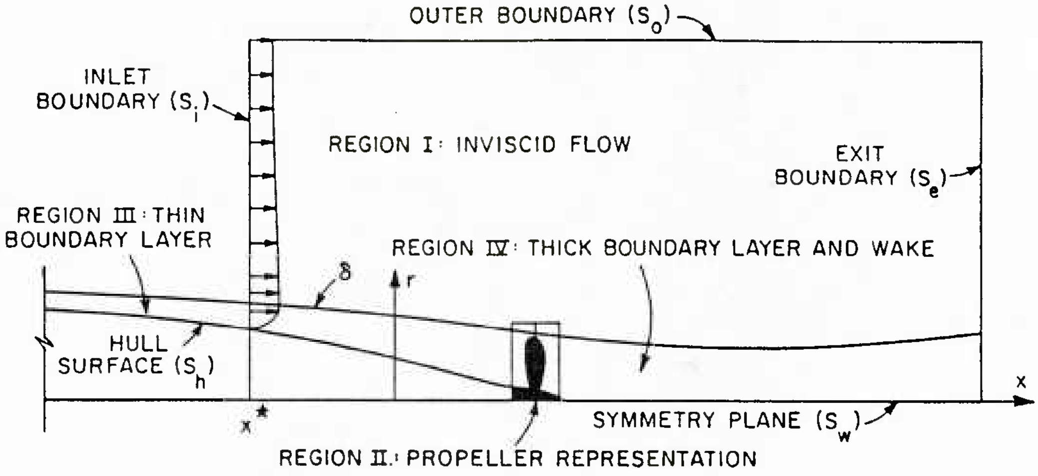

Figure 1. Definition sketch of the flow-field regions

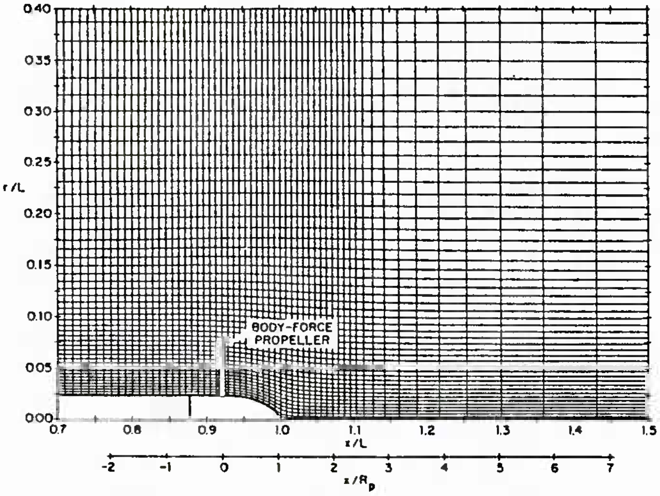

Figure 2. P4660 fine grid (partial view)

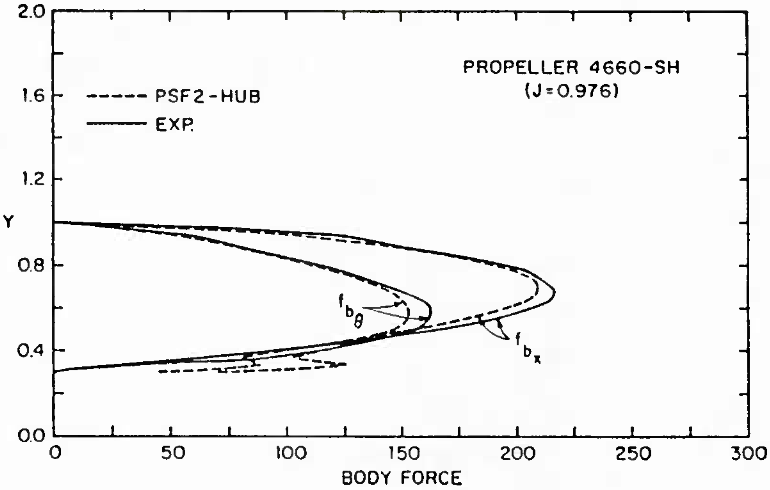

Figure 3. Body-force distributions

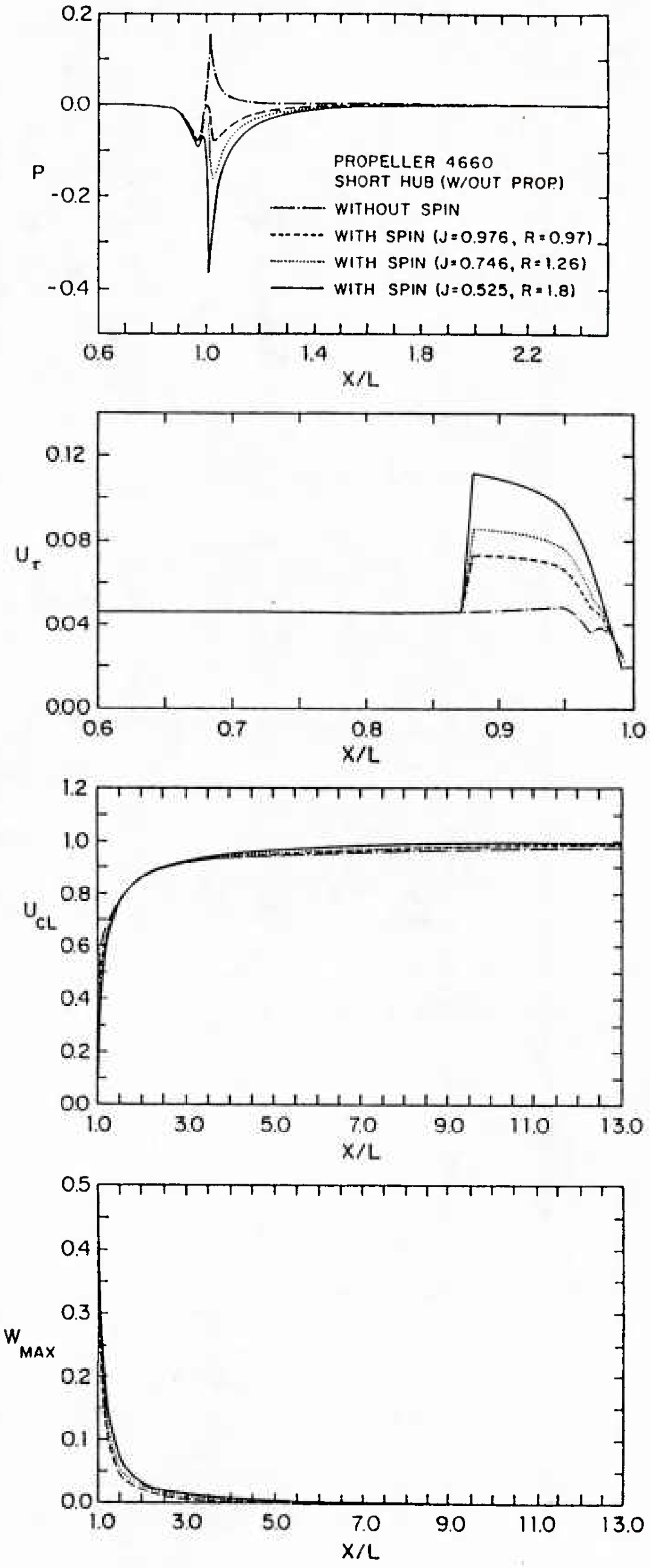

Figure 4. Body surface and wake centerline pressure, and wall-shear, wake centerline, and maximum swirl velocities (without propeller)

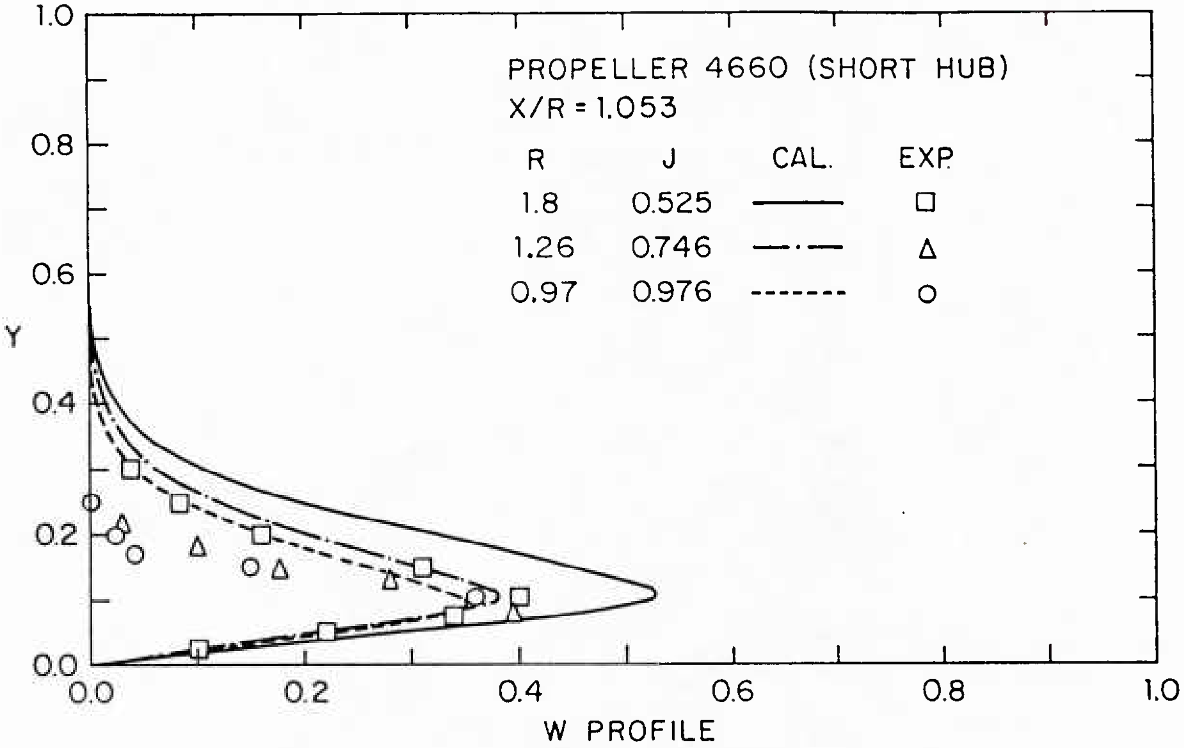

Figure 5. Swirl velocity profile (without propeller)

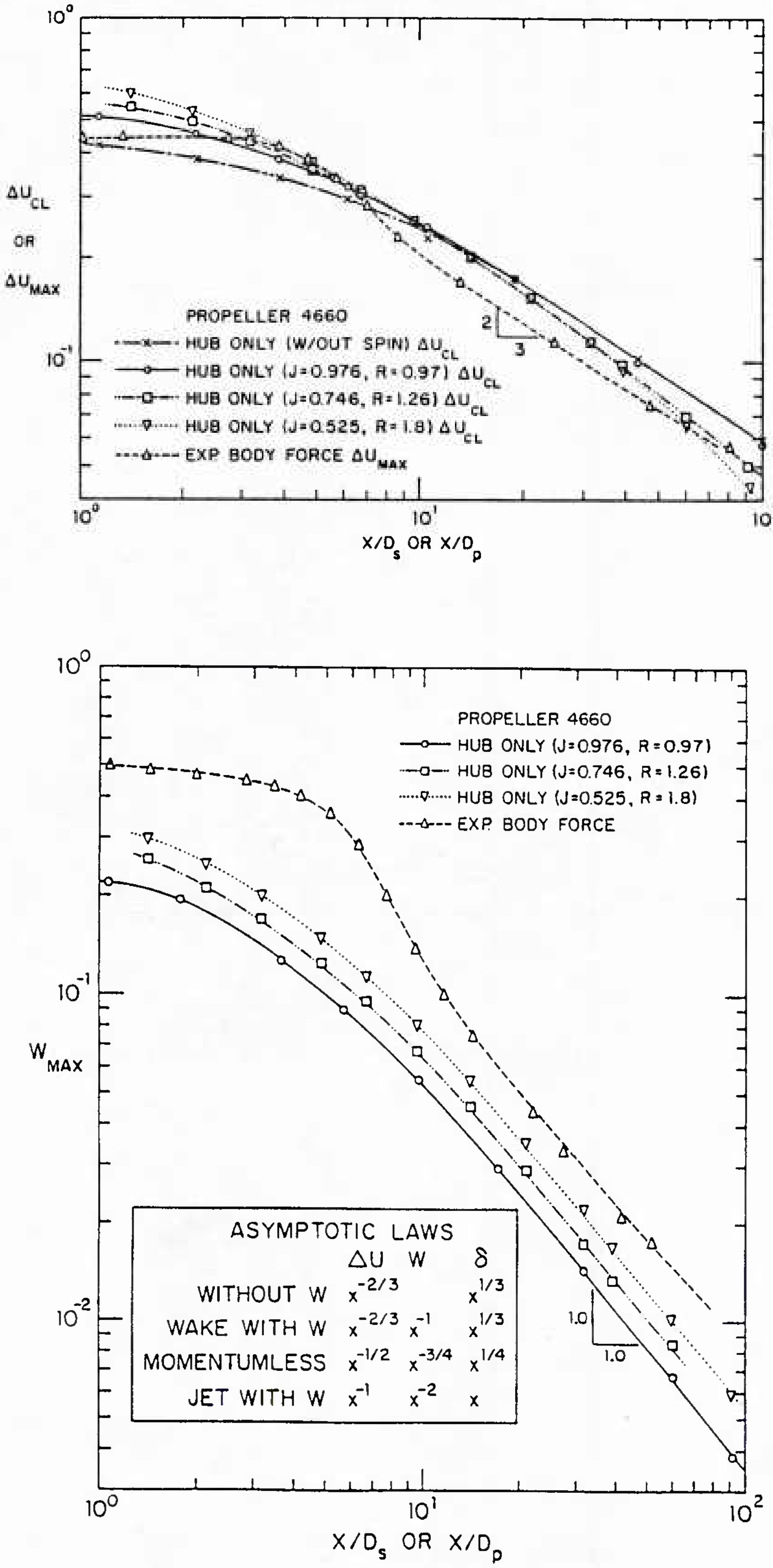

Figure 6. Far wake asymptotic forms

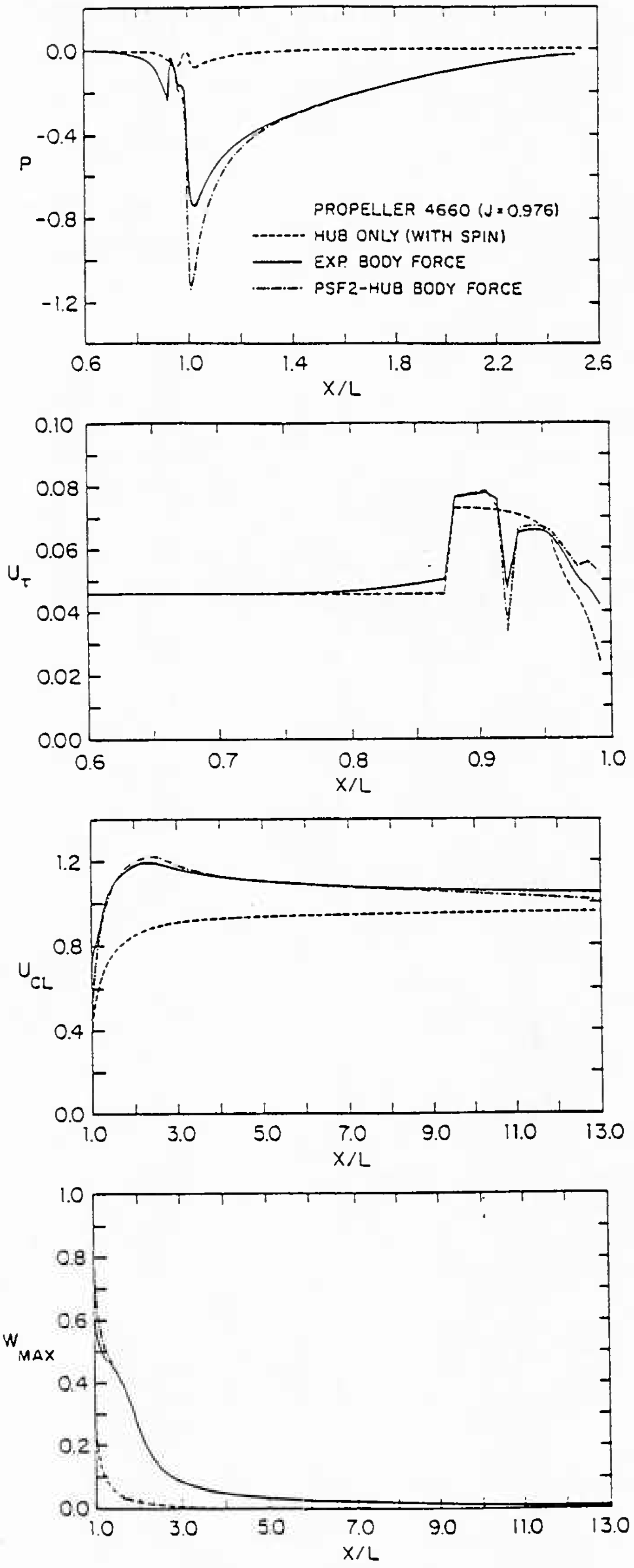

Figure 7. Body surface and wake centerline pressure, and wall-shear, wake centerline, and maximum swirl velocities (with propeller)

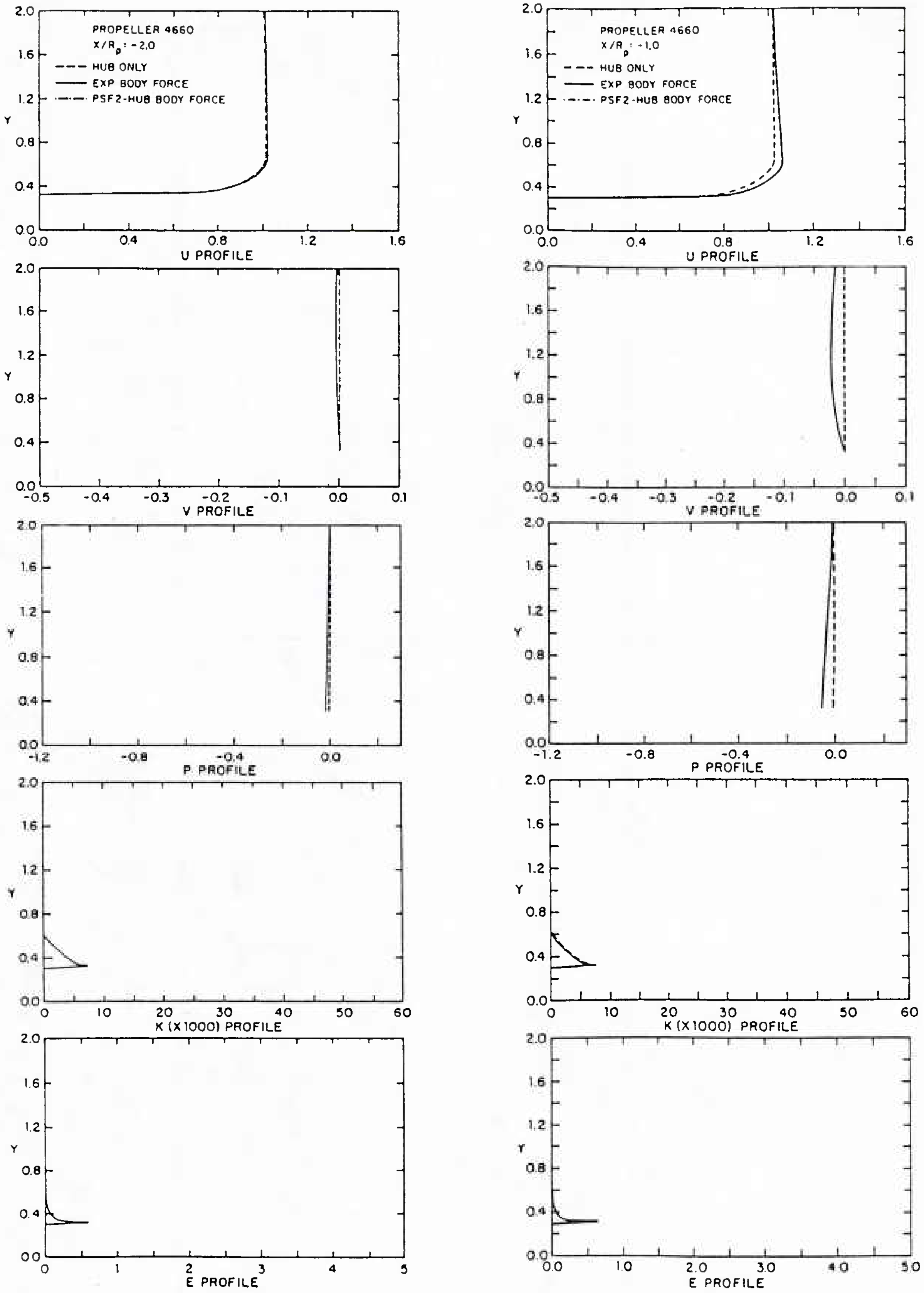

(a)

(b)

Figure 8. Velocity, pressure, and turbulence parameter profiles (with propeller)

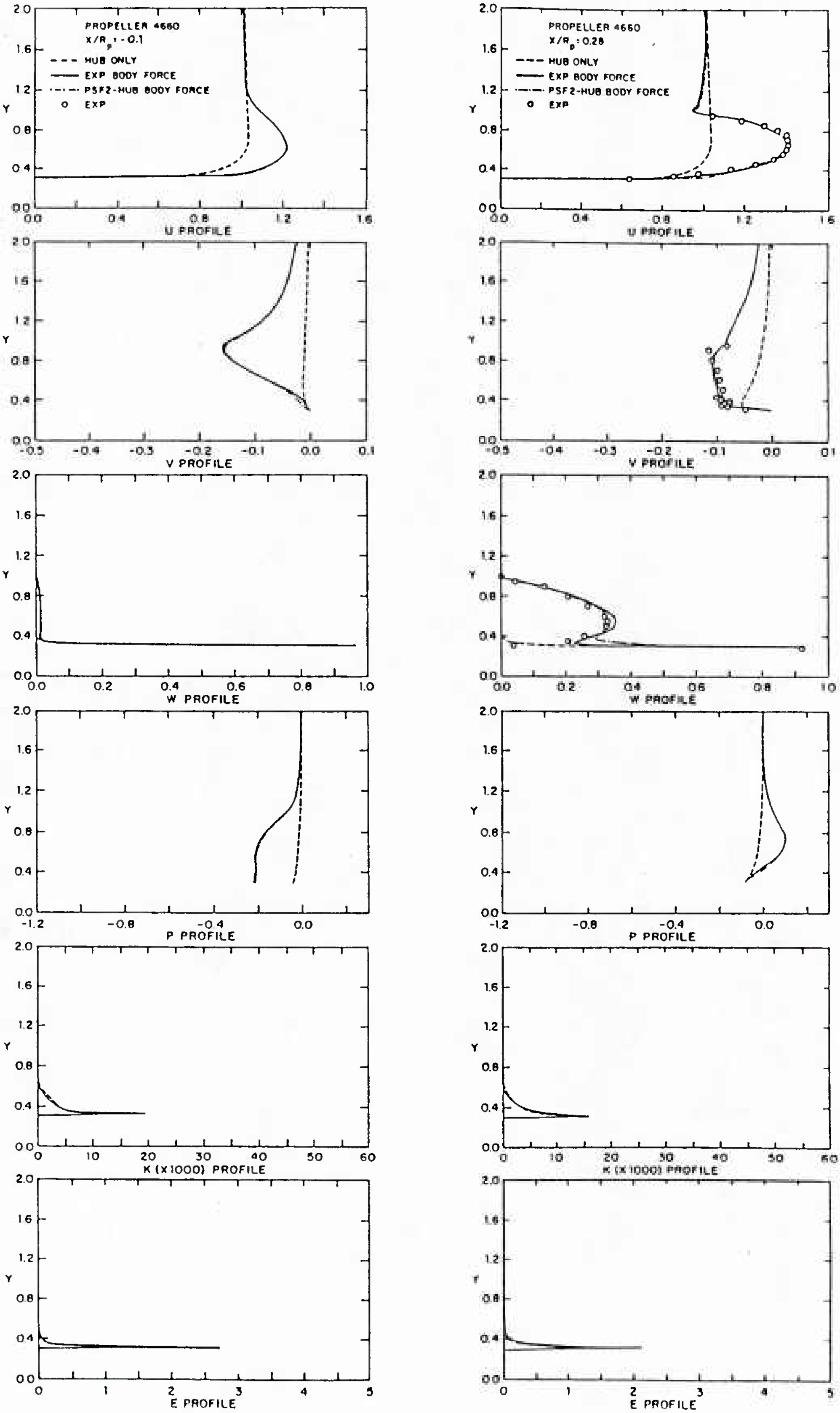

(c) (d)

Figure 8. (continued)

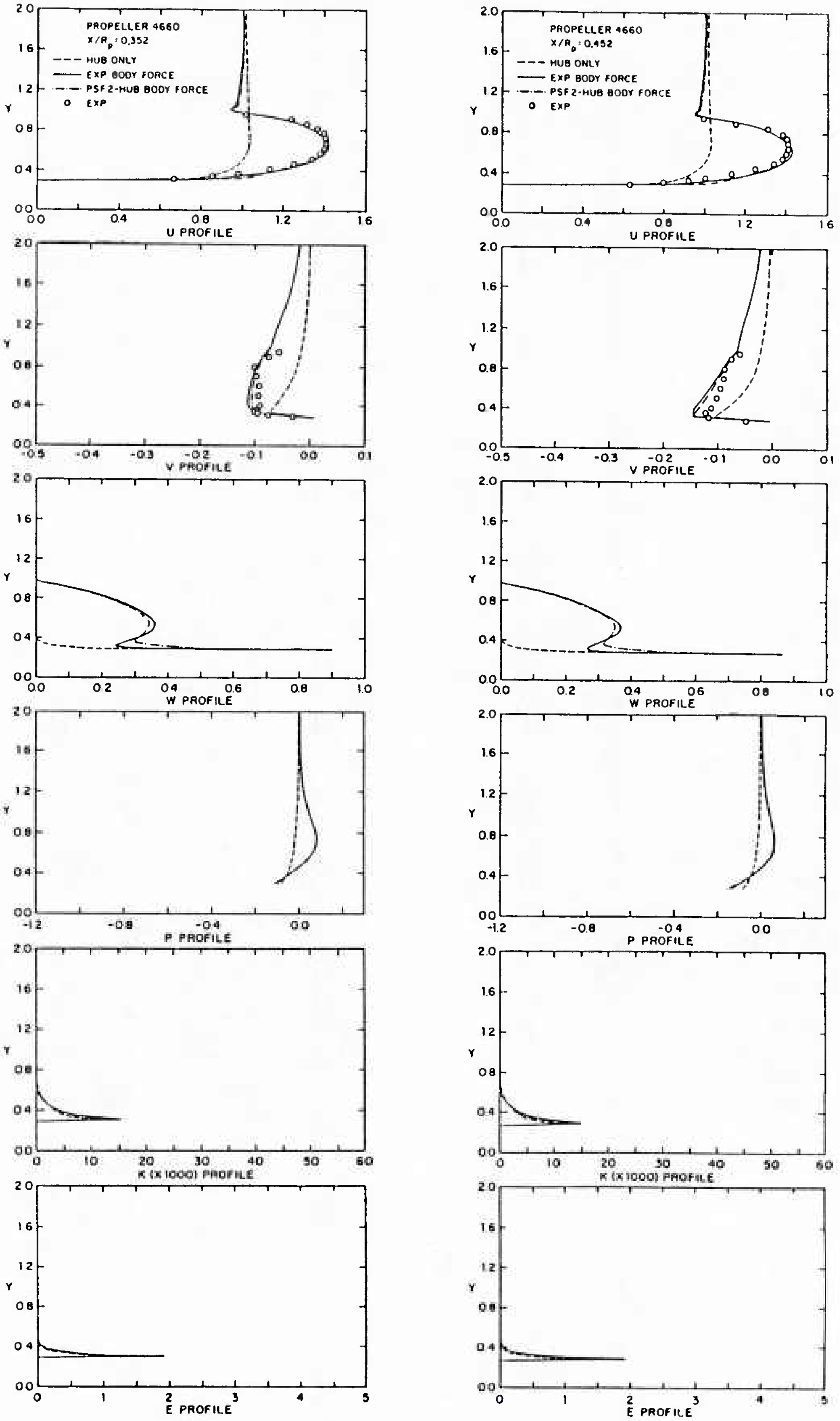

(e)

(f)

Figure 8. (continued)

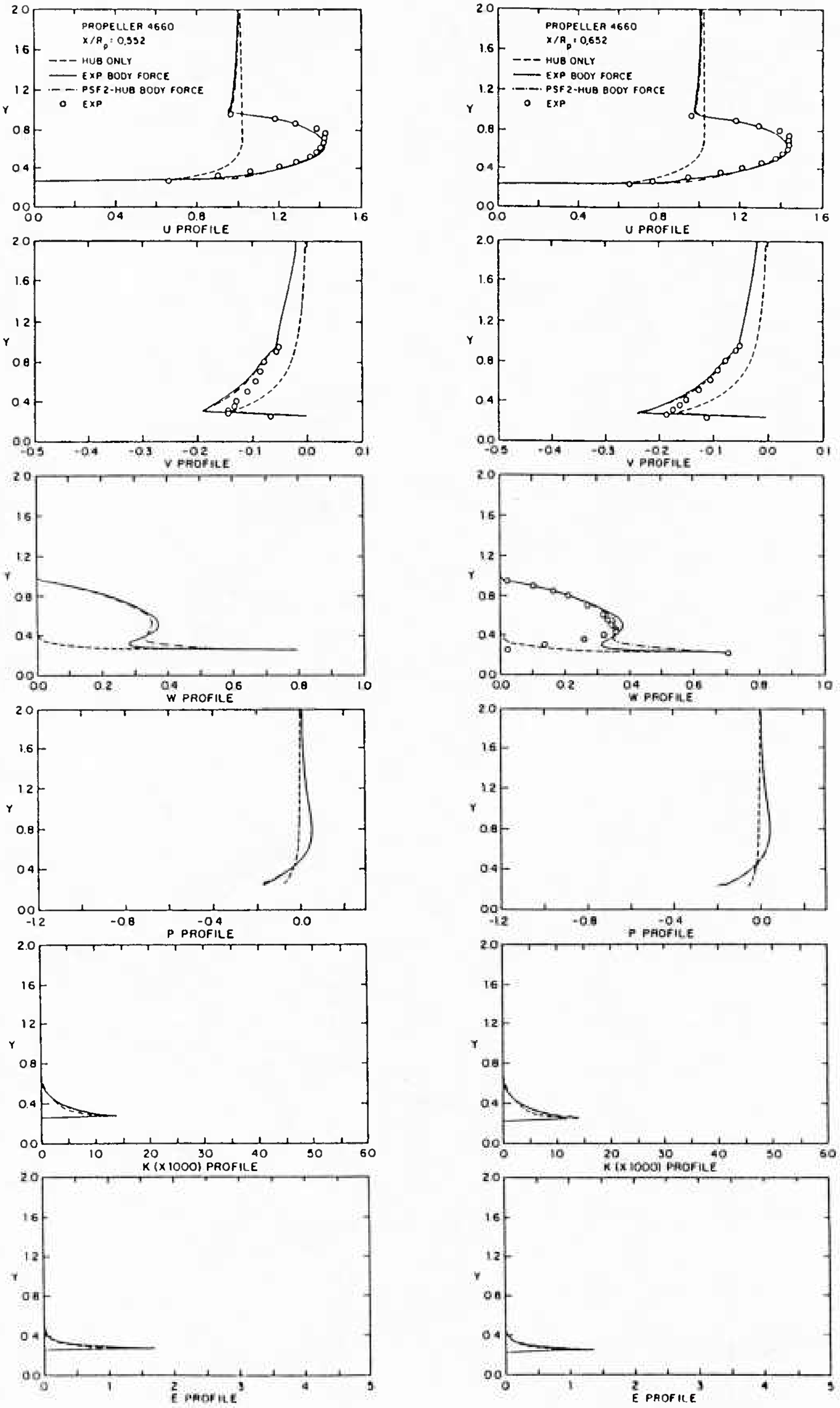

(g) (h)

Figure 8. (continued)

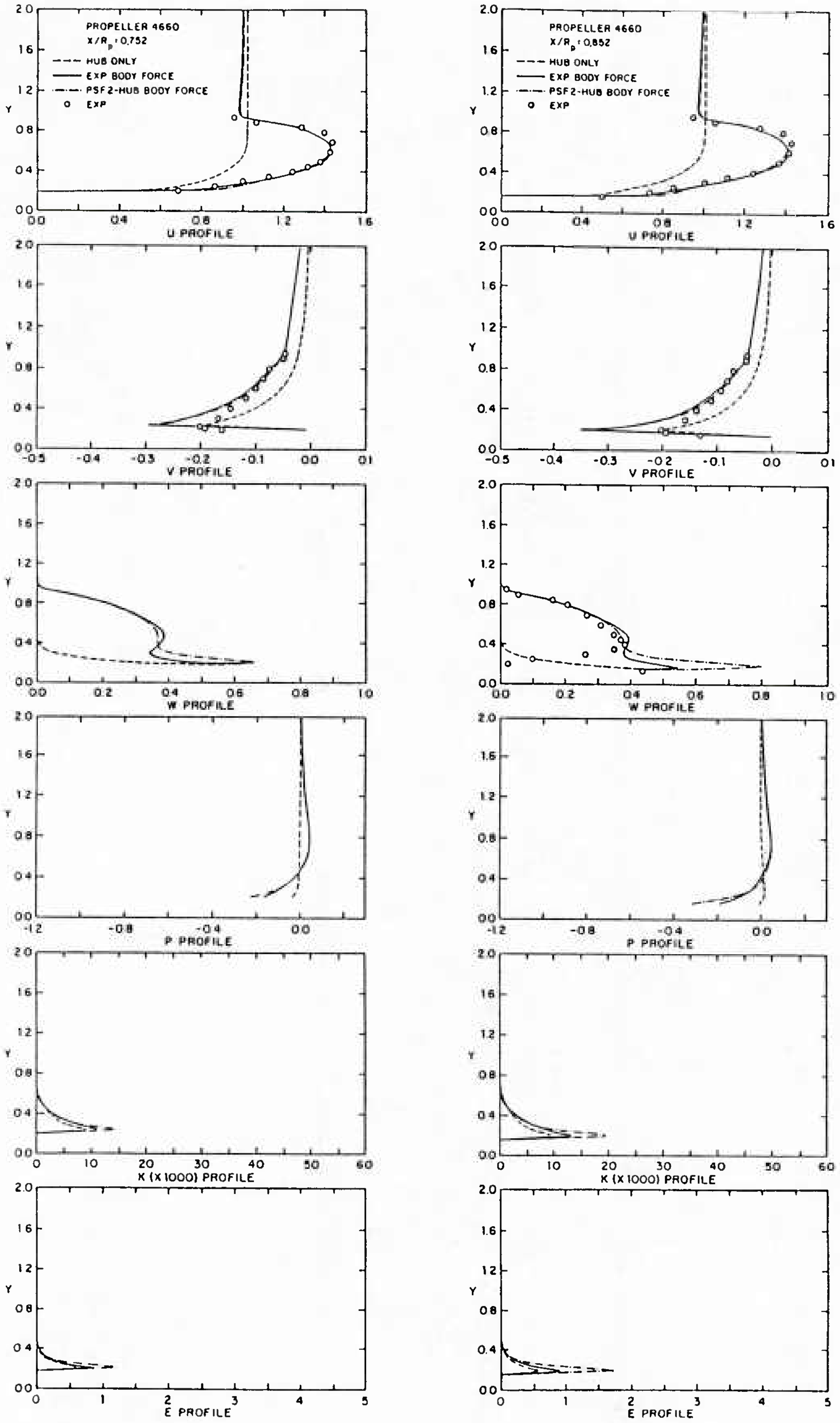

(i)

(j)

Figure 8. (continued)

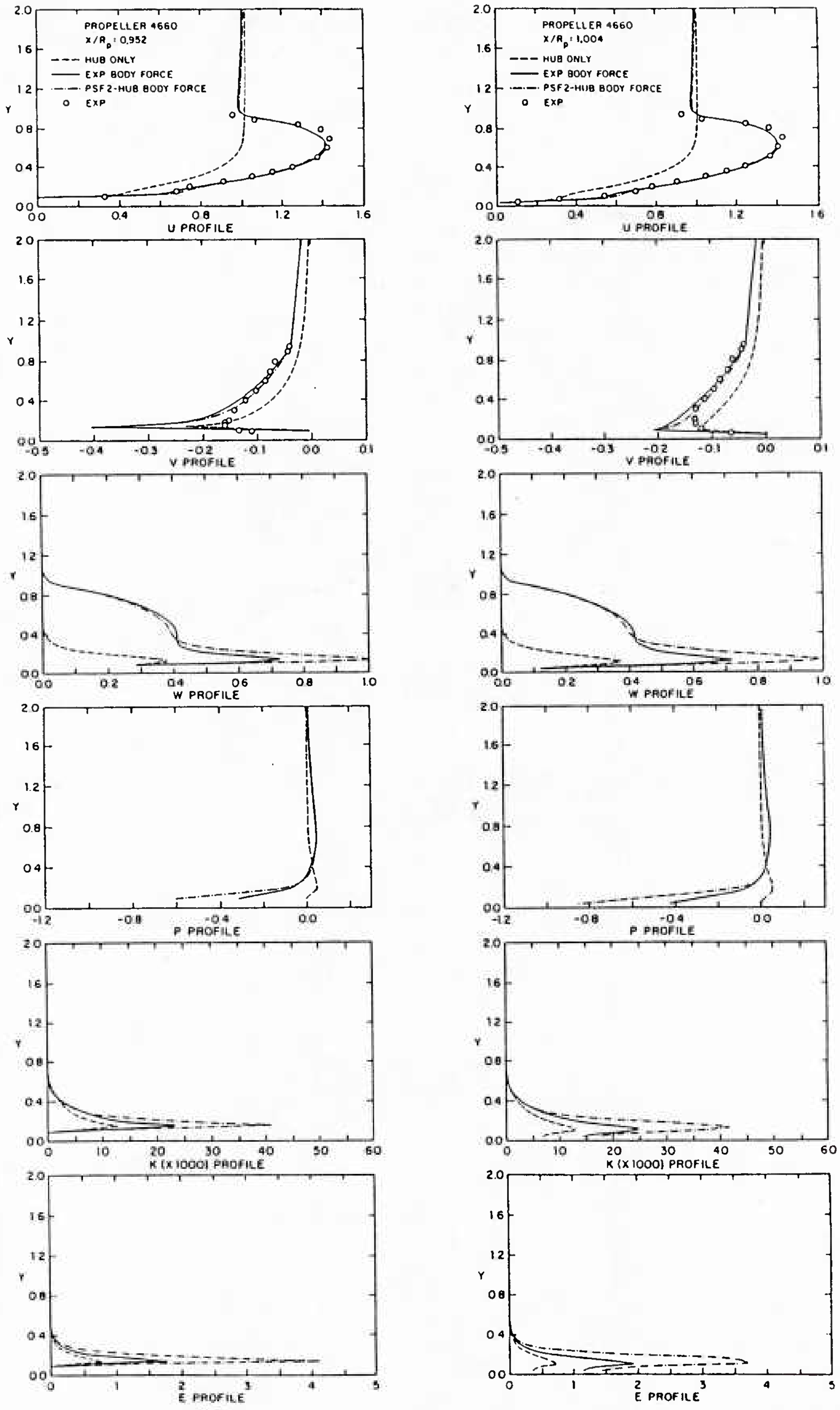

(k)

(l)

Figure 8. (continued)

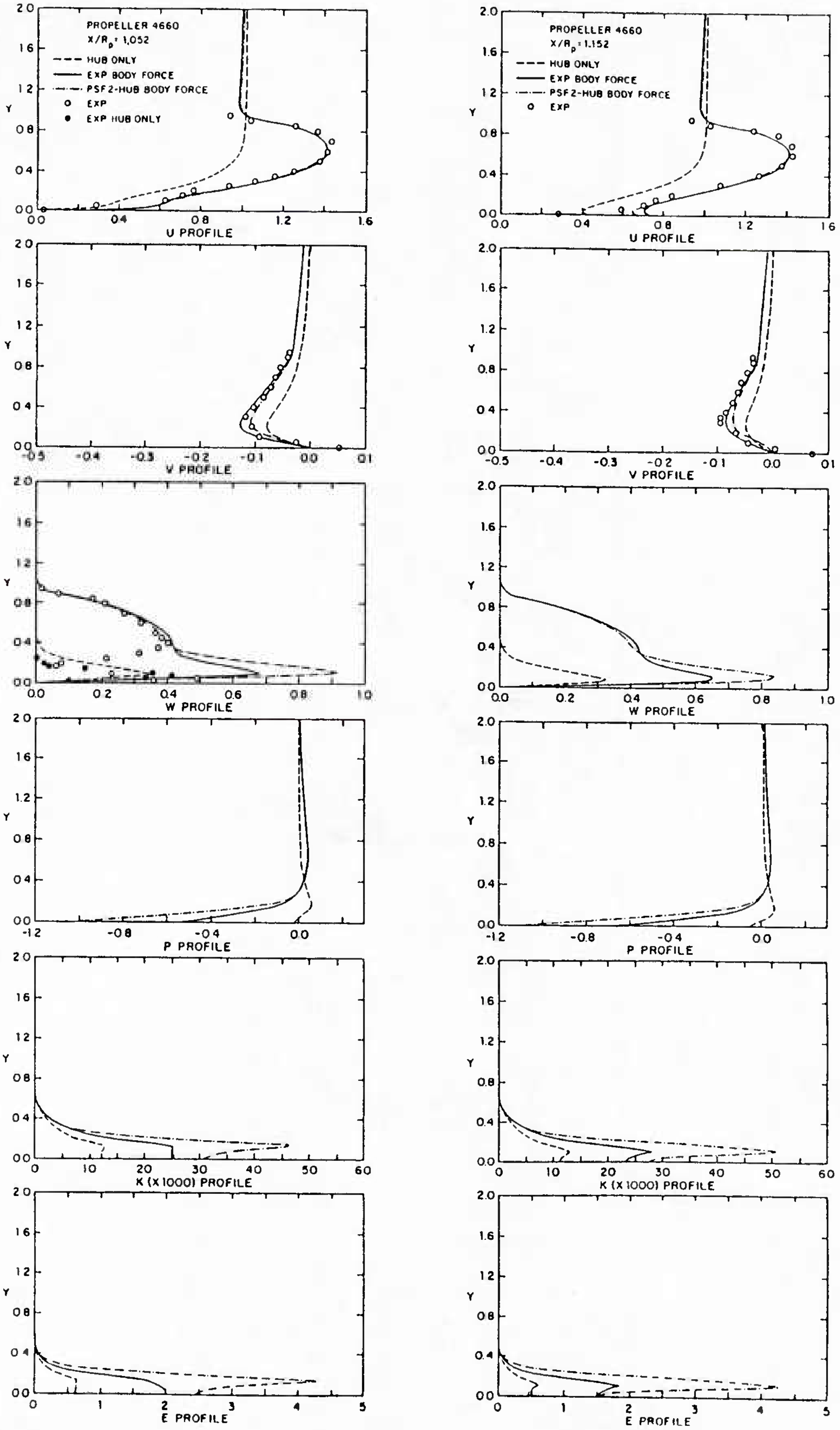

(m)

(n)

Figure 8. (continued)

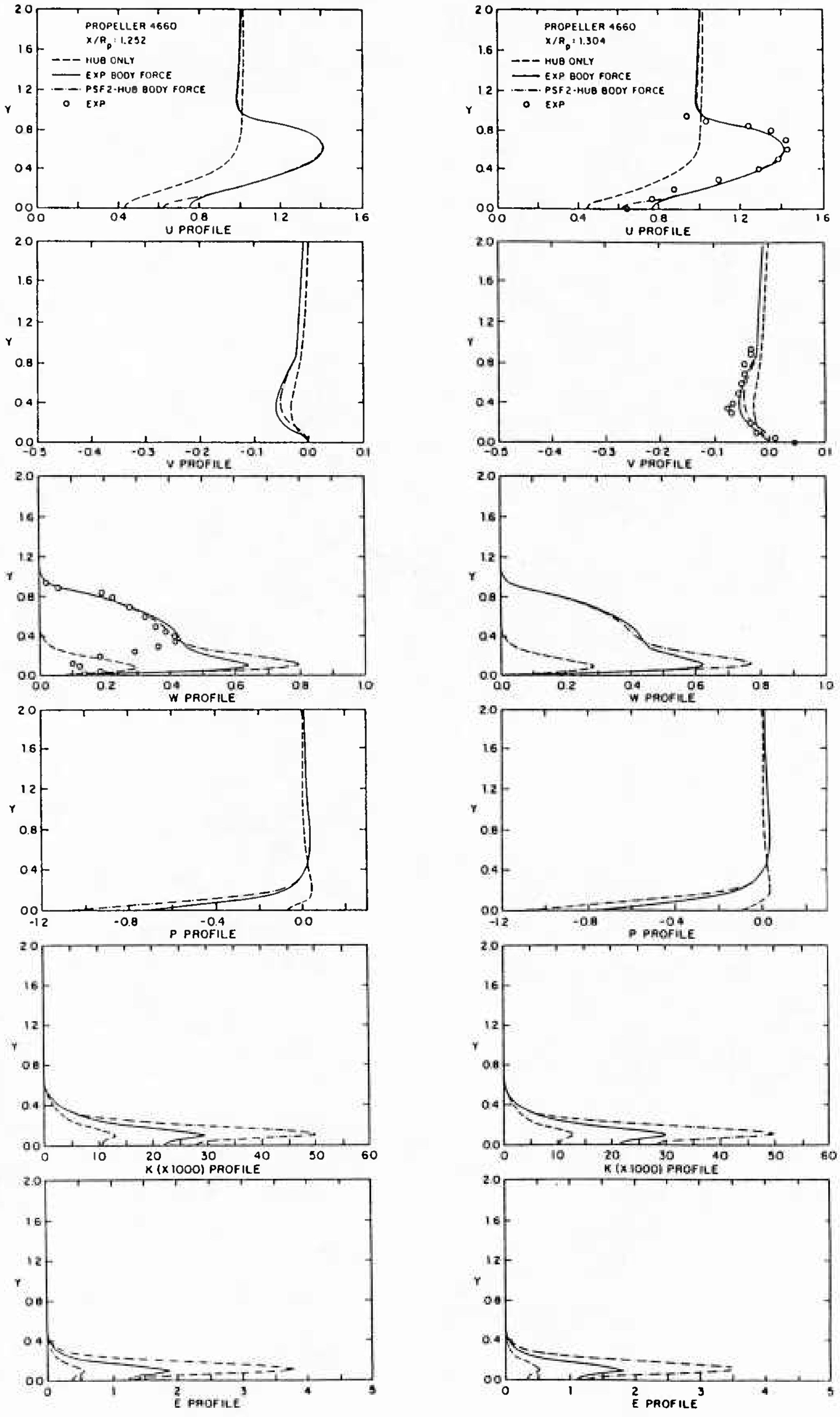

(o) (p)

Figure 8. (continued)

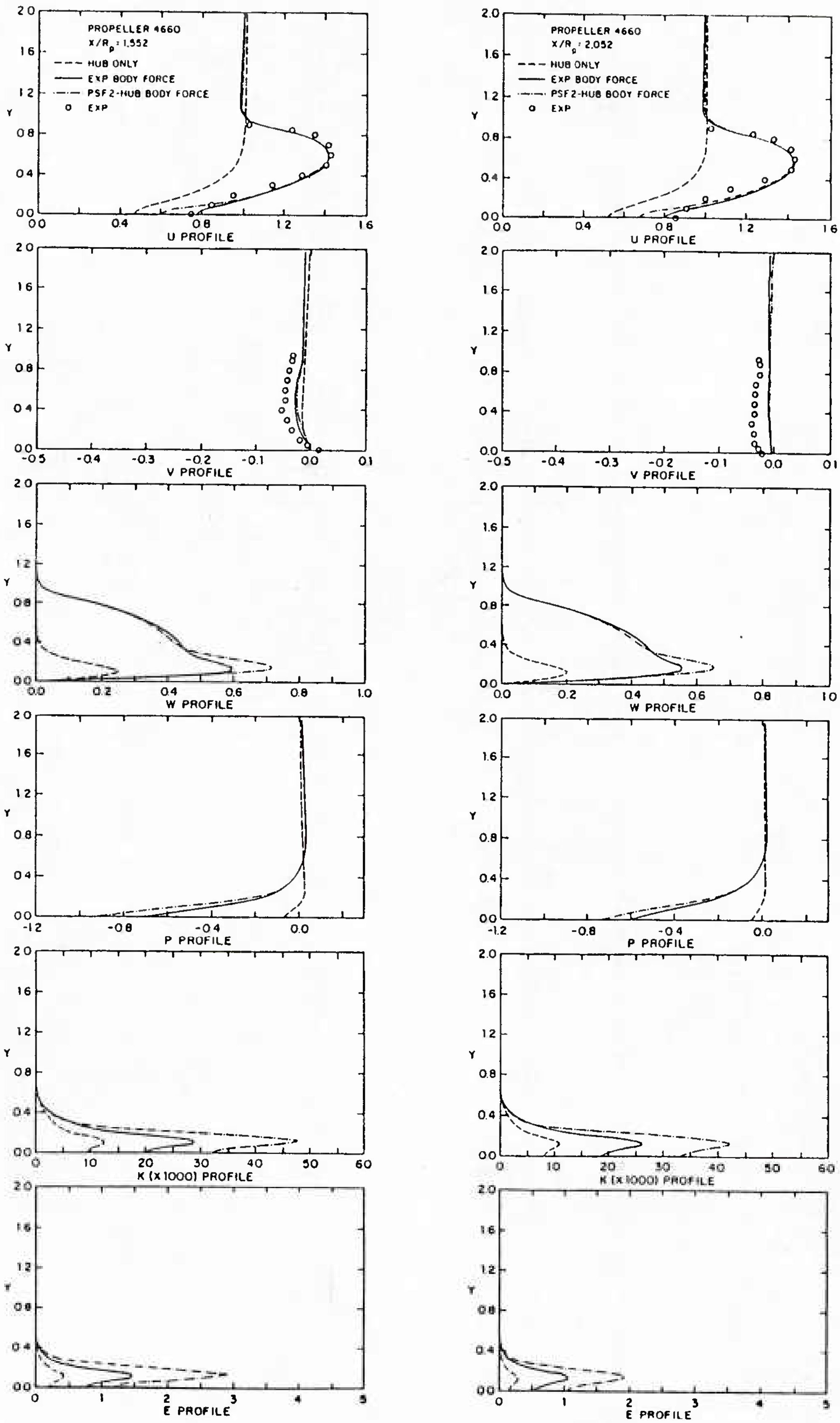

(q)

(r)

Figure 8. (continued)

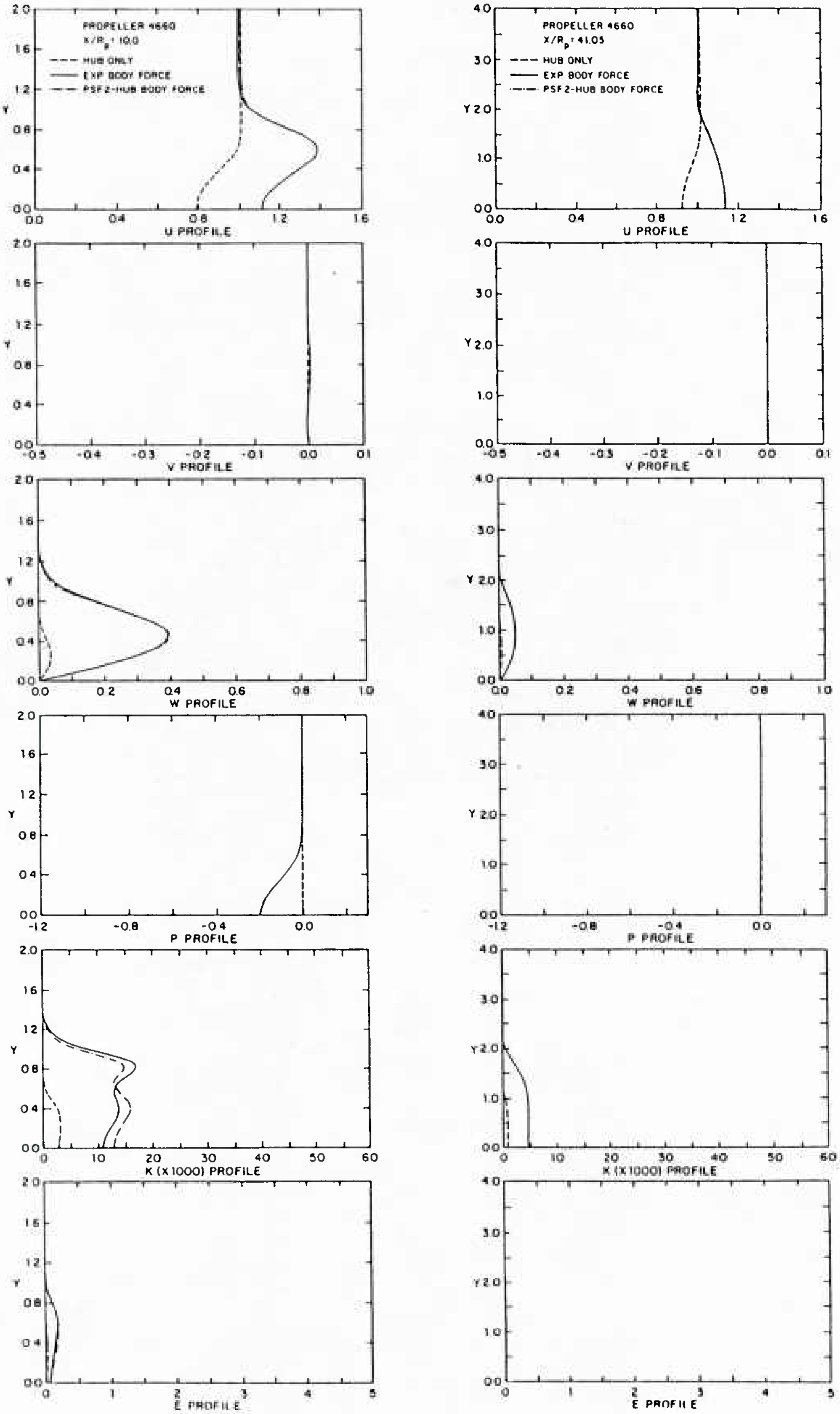

(s) (t)

Figure 8. (continued)

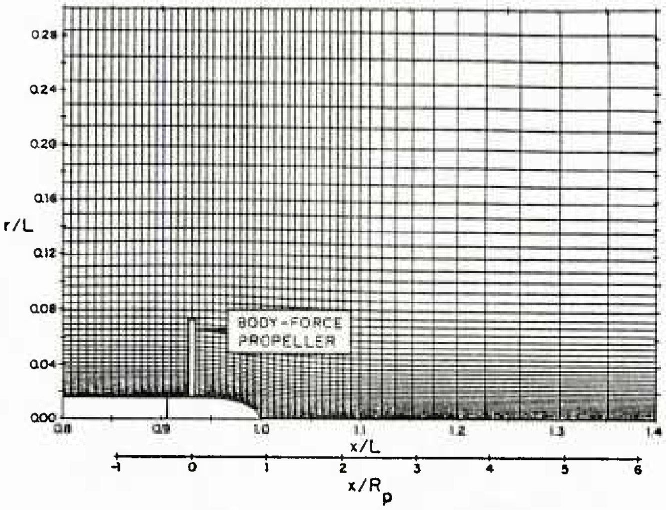

Figure 9. P4498 fine grid (partial view)

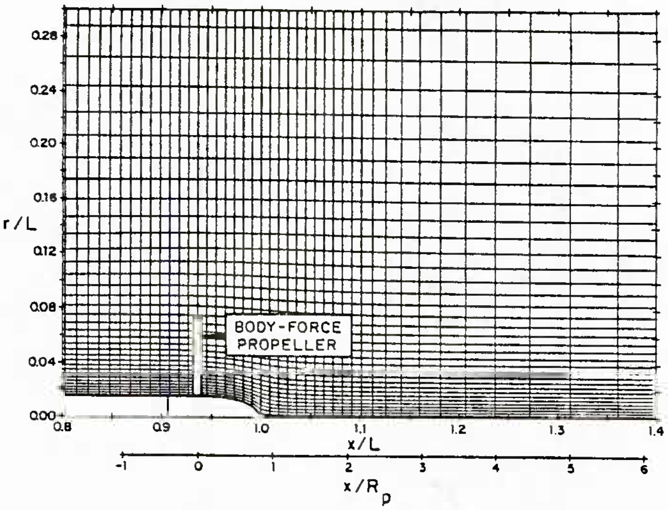

Figure 10. P4498 coarse grid (partial view)

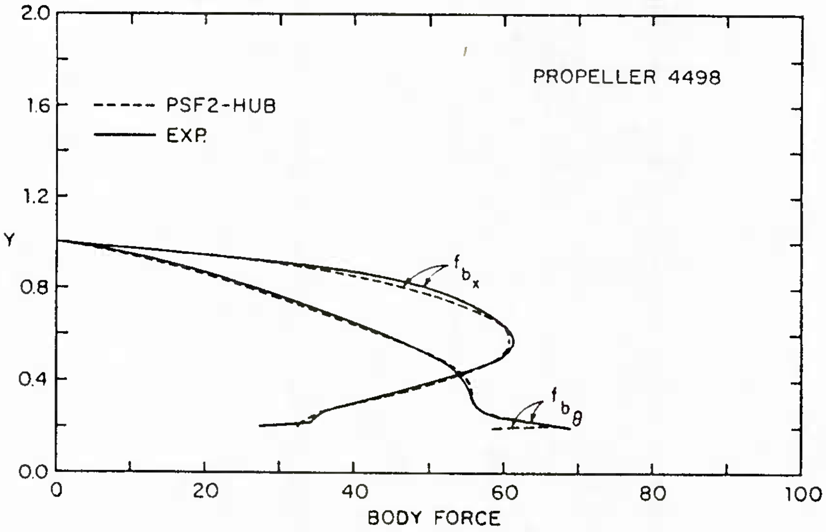

Figure 11. Body-force distributions

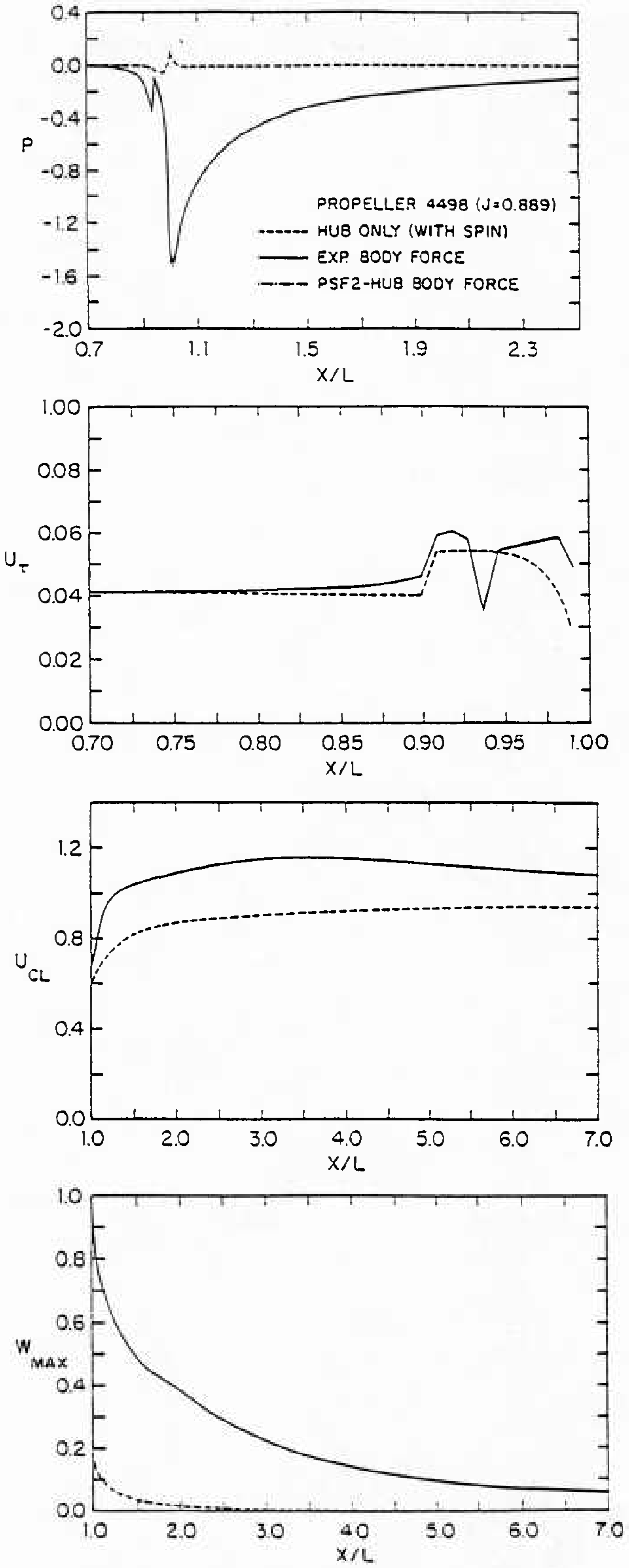

Figure 12. Body surface and wake centerline pressure, and wall-shear, wake centerline, and maximum swirl velocities (with propeller)

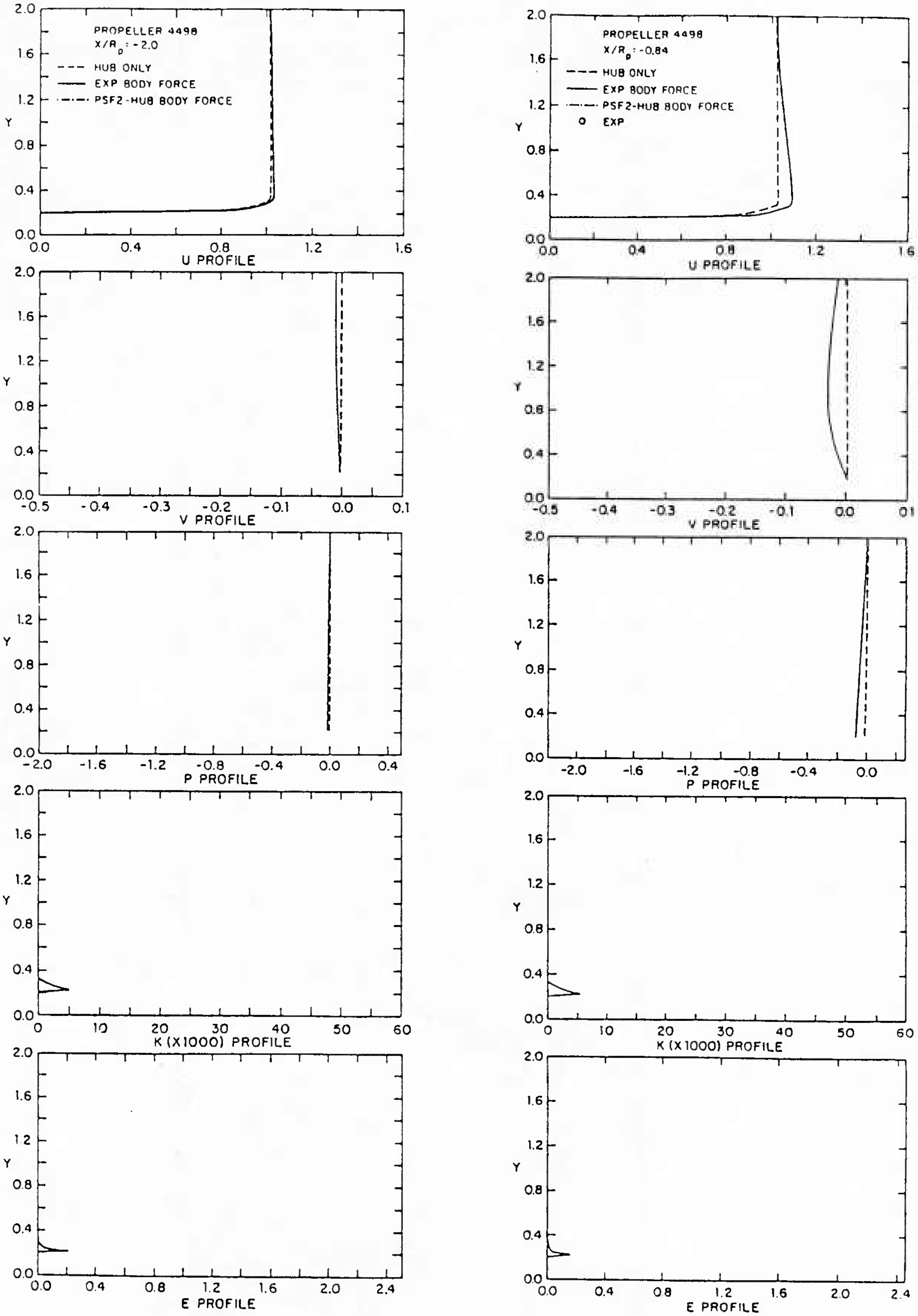

(a)

(b)

Figure 13. Velocity, pressure, and turbulence parameter profiles (with propeller)

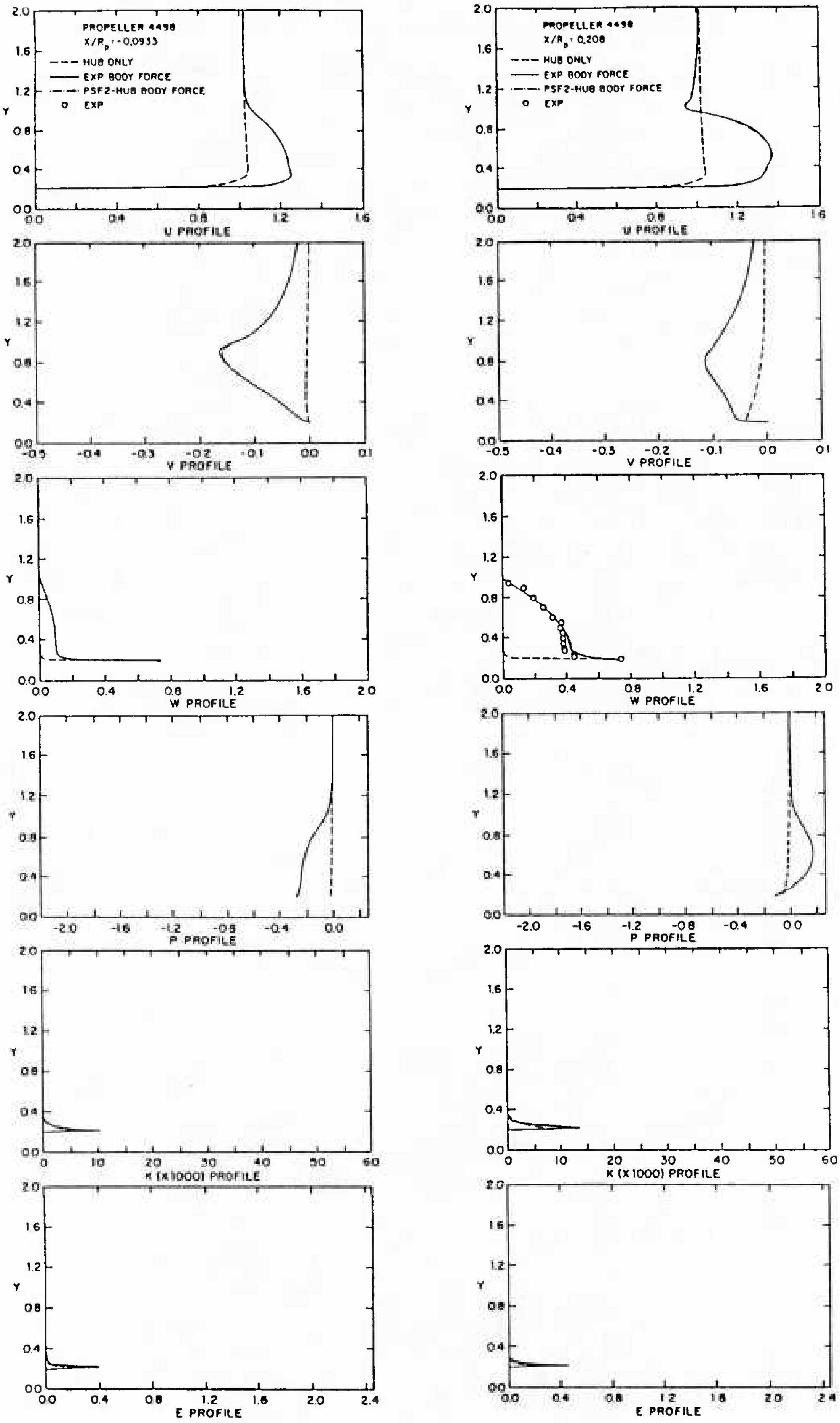

(c) (d)

Figure 13. (continued)

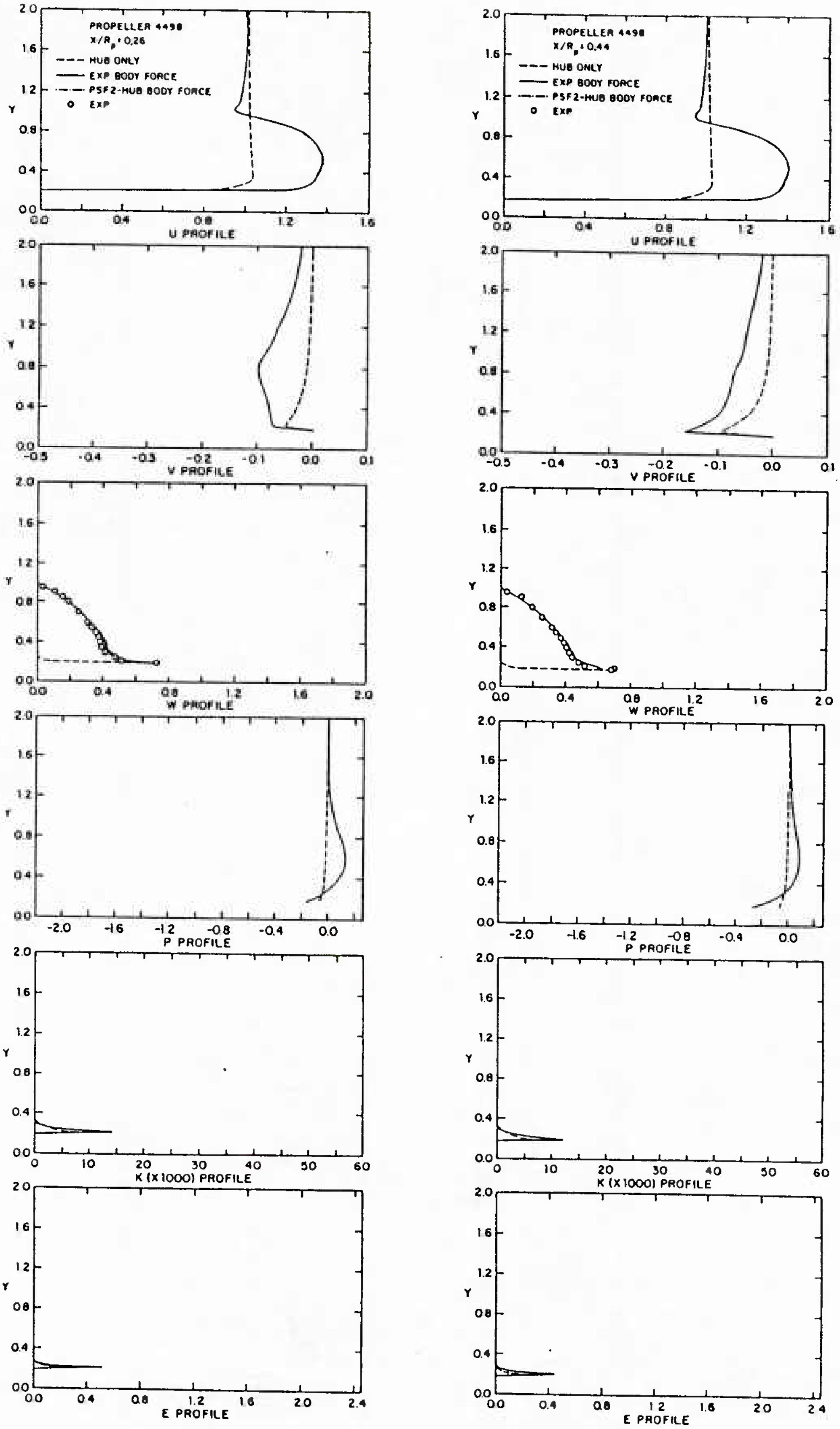

(e)

(f)

Figure 13. (continued)

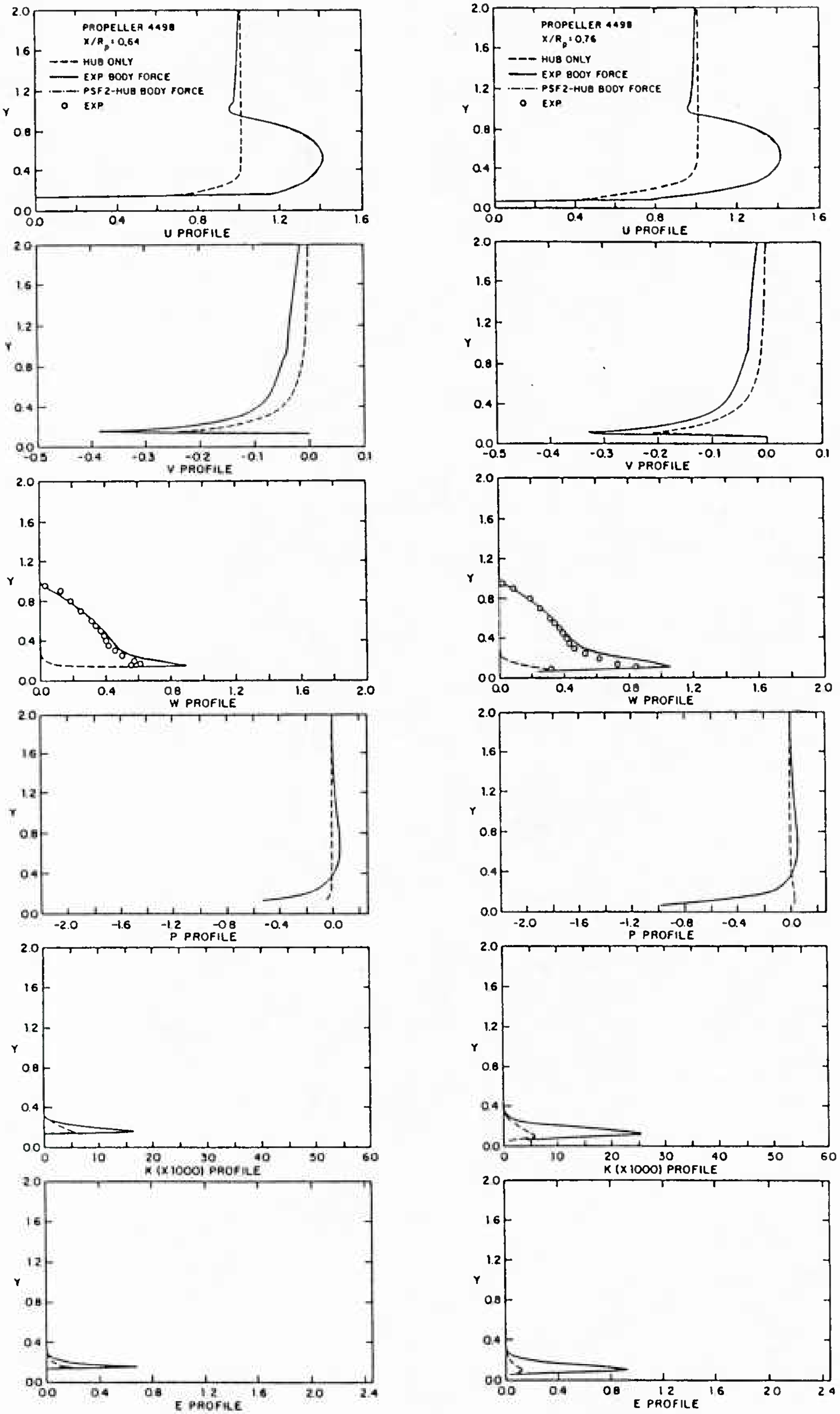

(g) (h)

Figure 13. (continued)

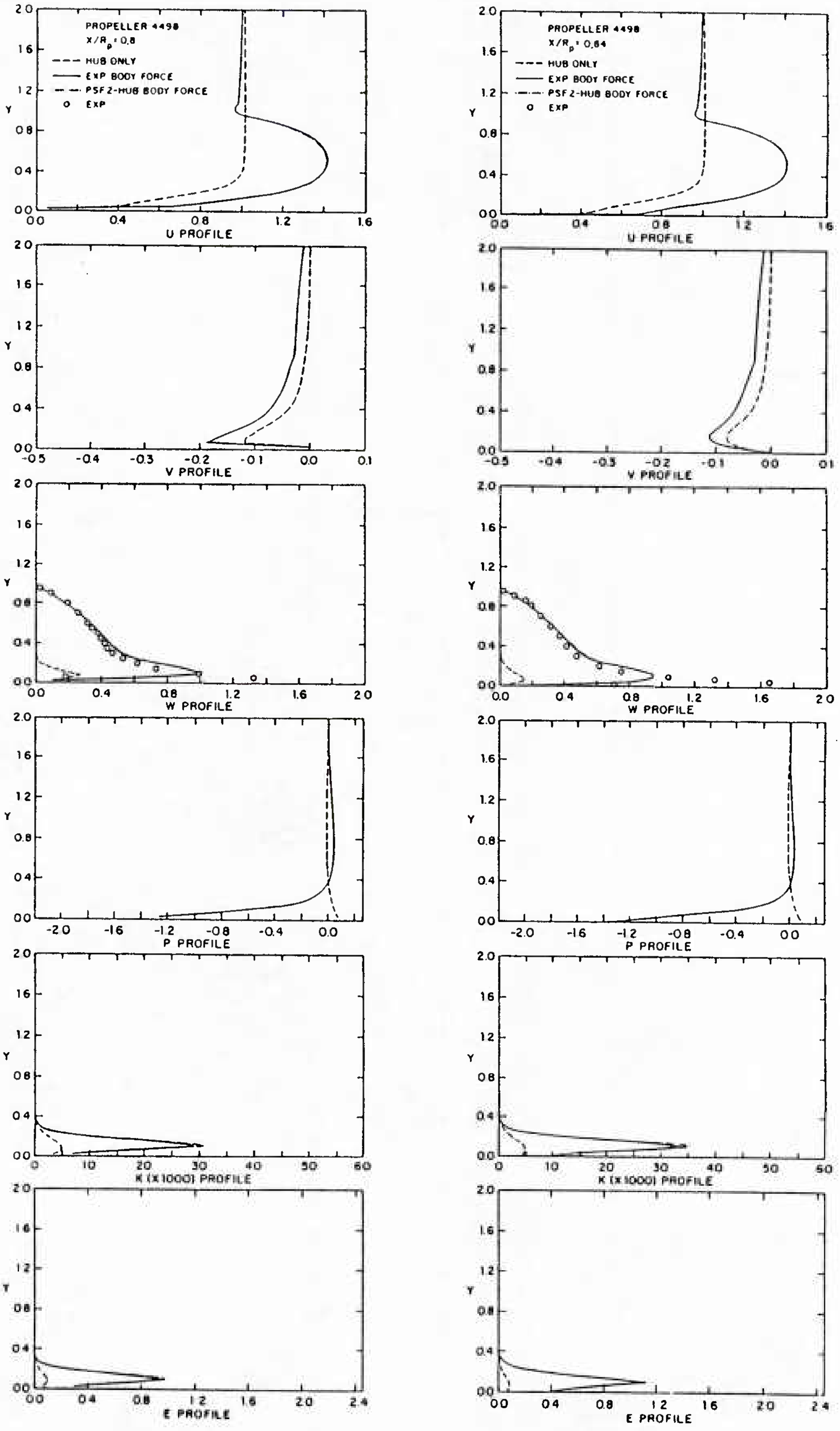

(i) (j)

Figure 13. (continued)

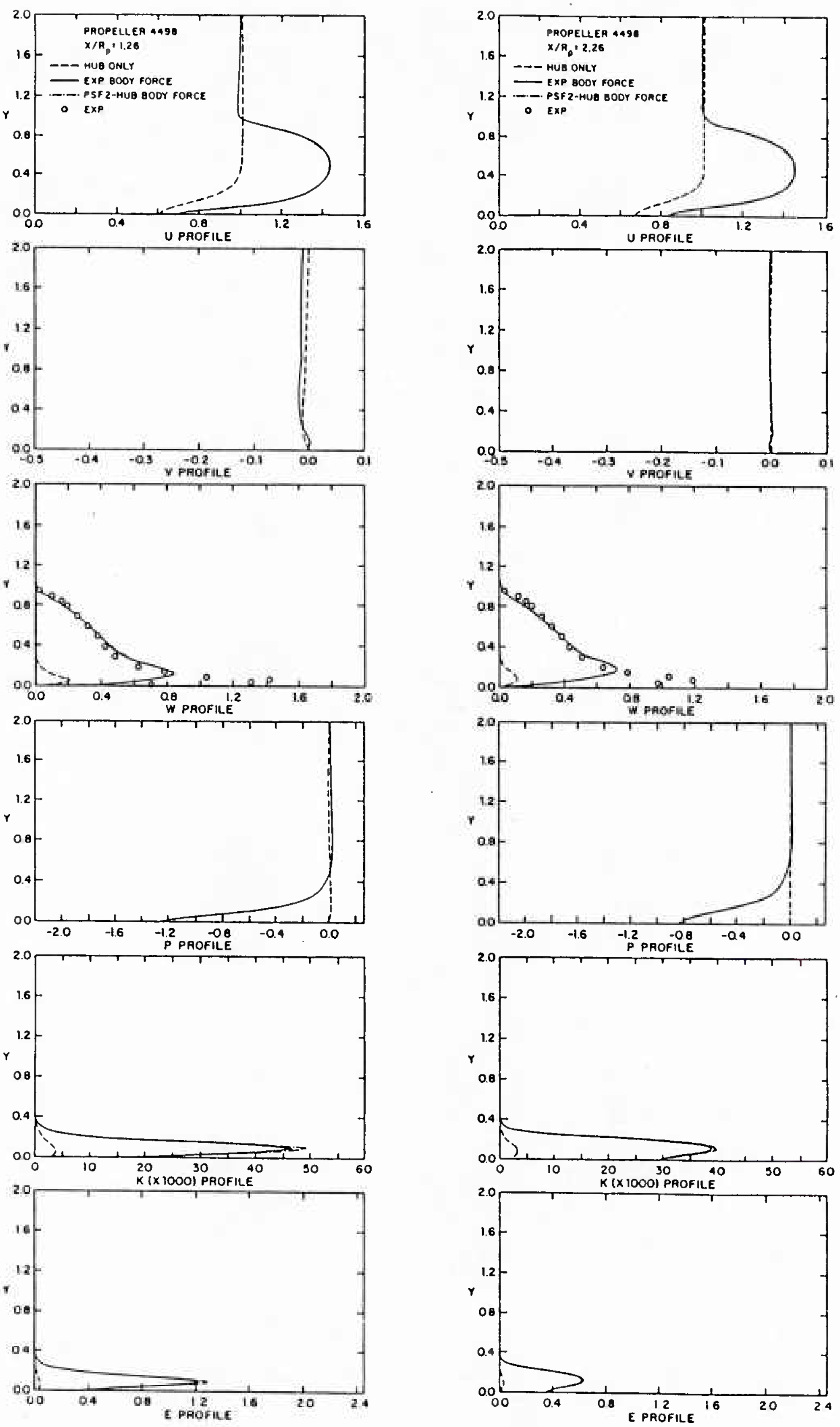

(k)

(l)

Figure 13. (continued)

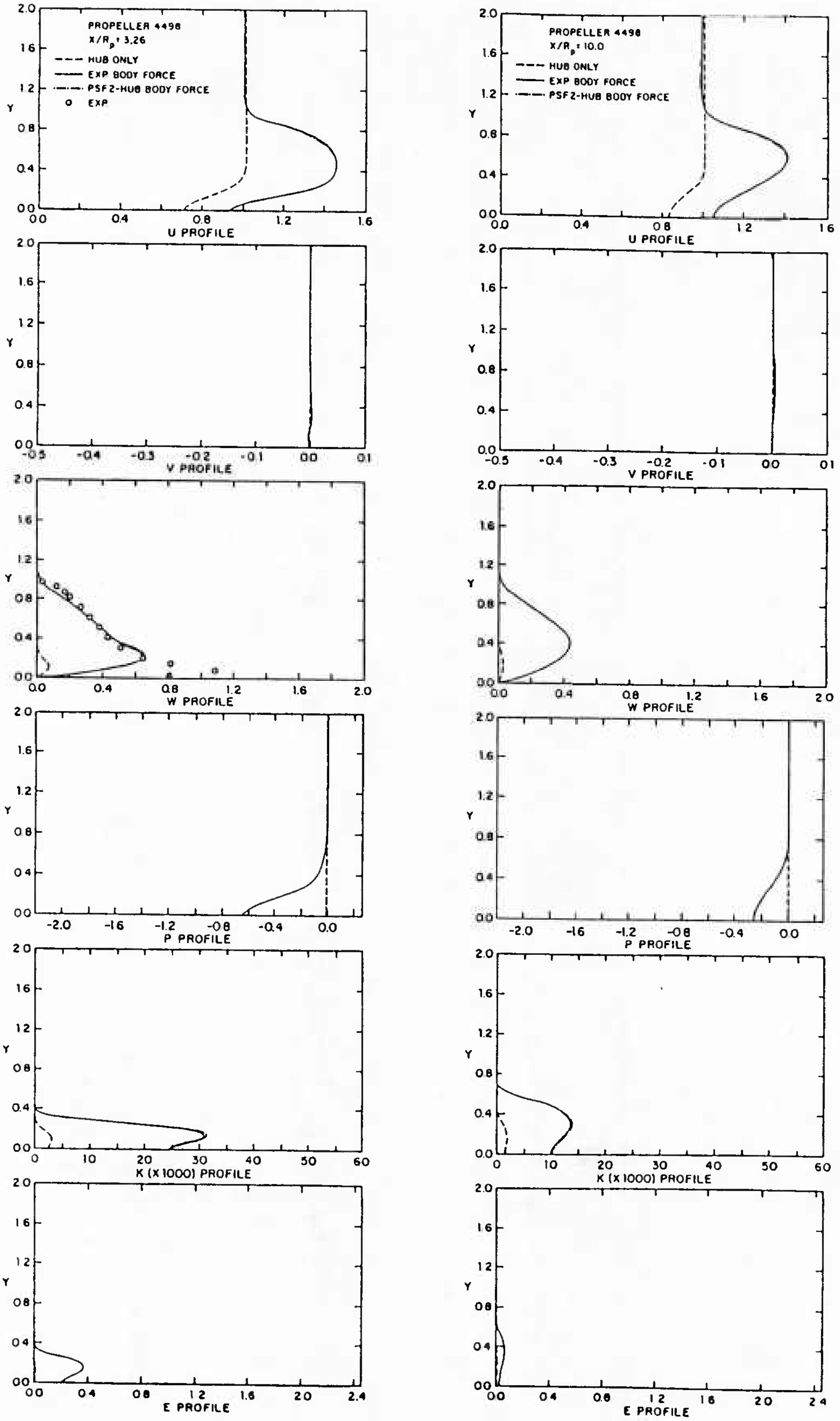

(m)

(n)

Figure 13. (continued)

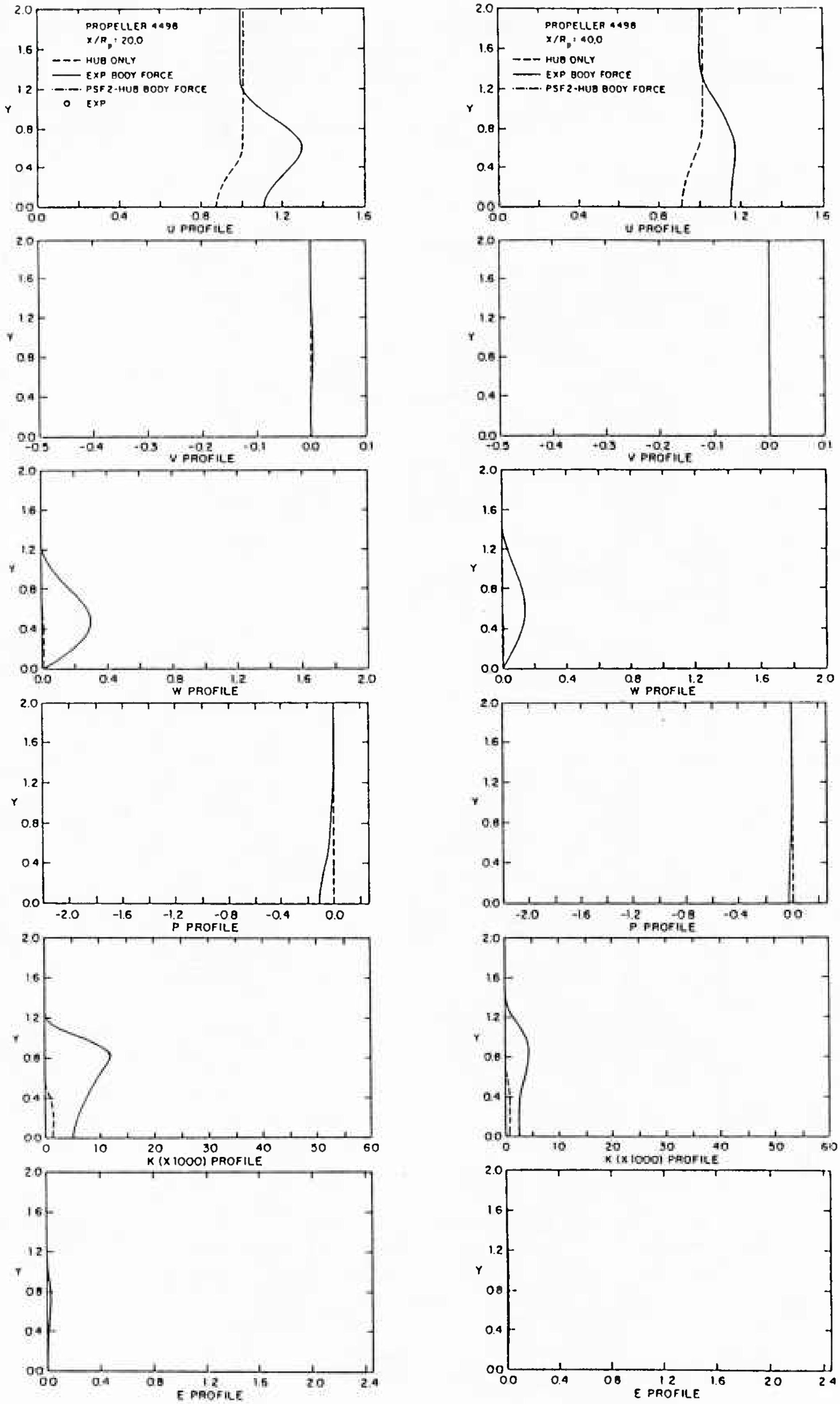

(o)

(p)

Figure 13. (continued)

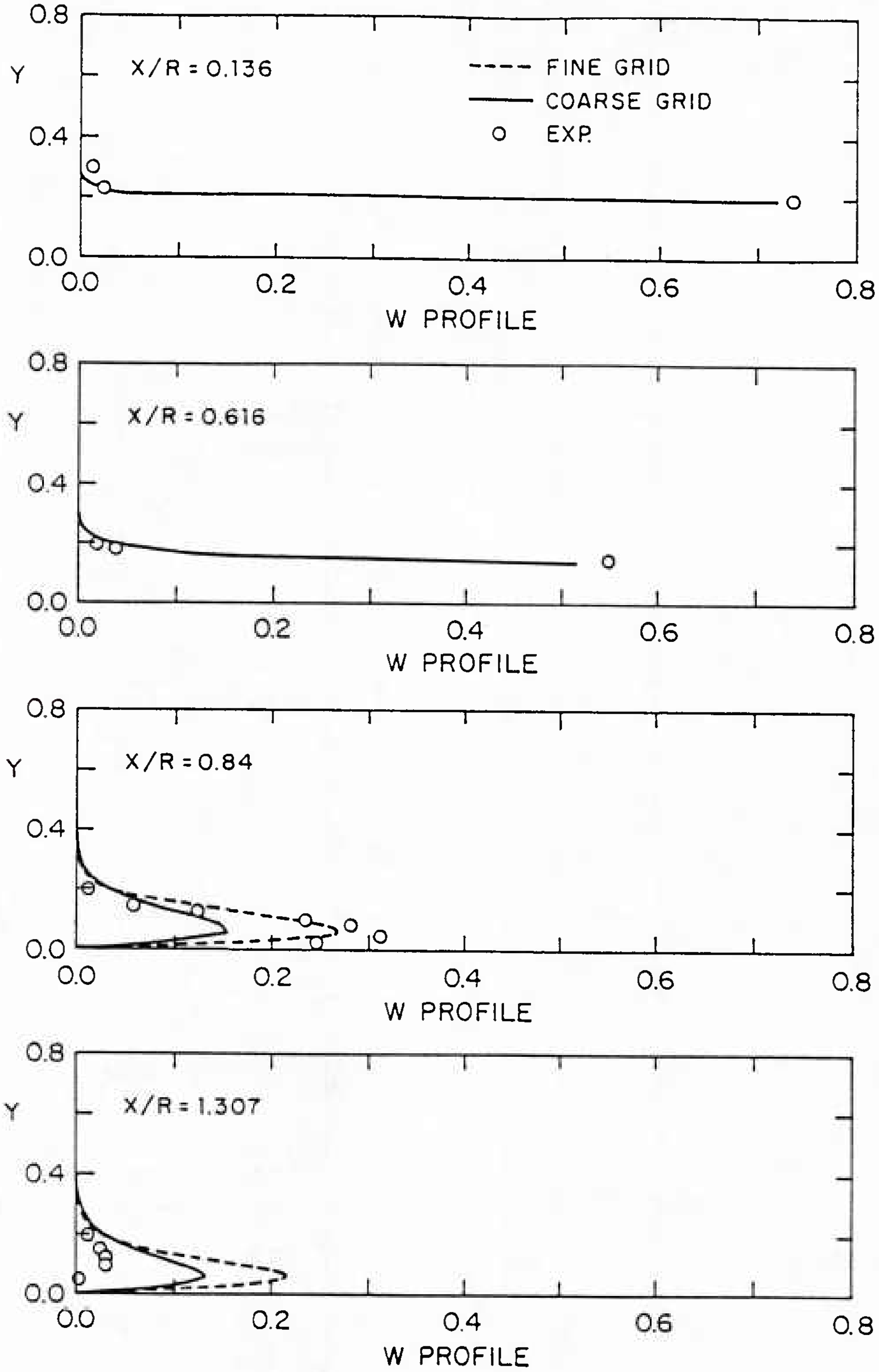

Figure 14. Swirl velocity profile (without propeller)

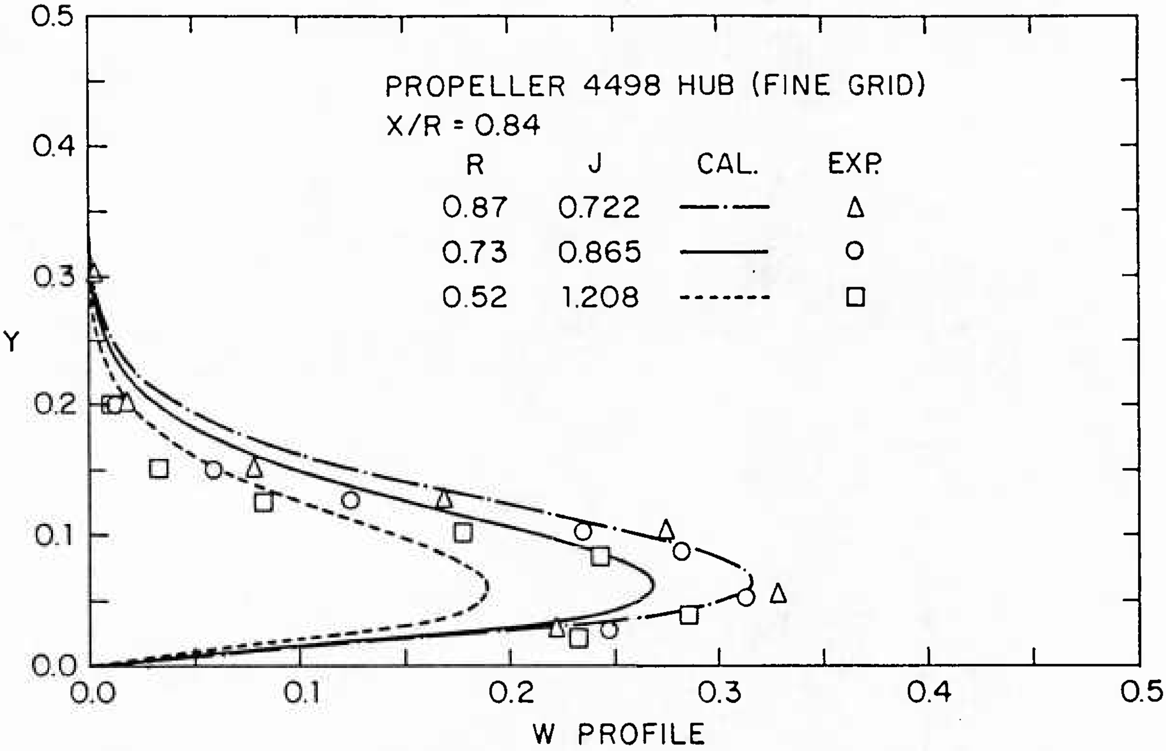

Figure 15. Swirl velocity profile (without propeller)

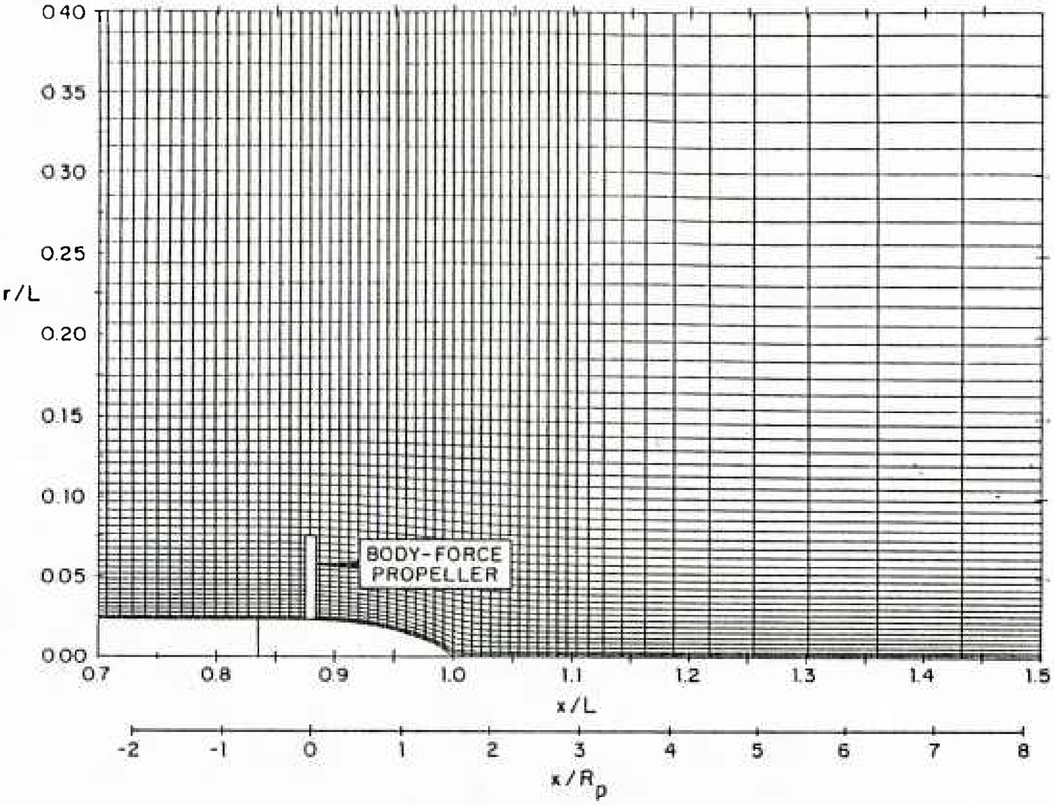

Figure 16. P4660 medium hub grid (partial view)

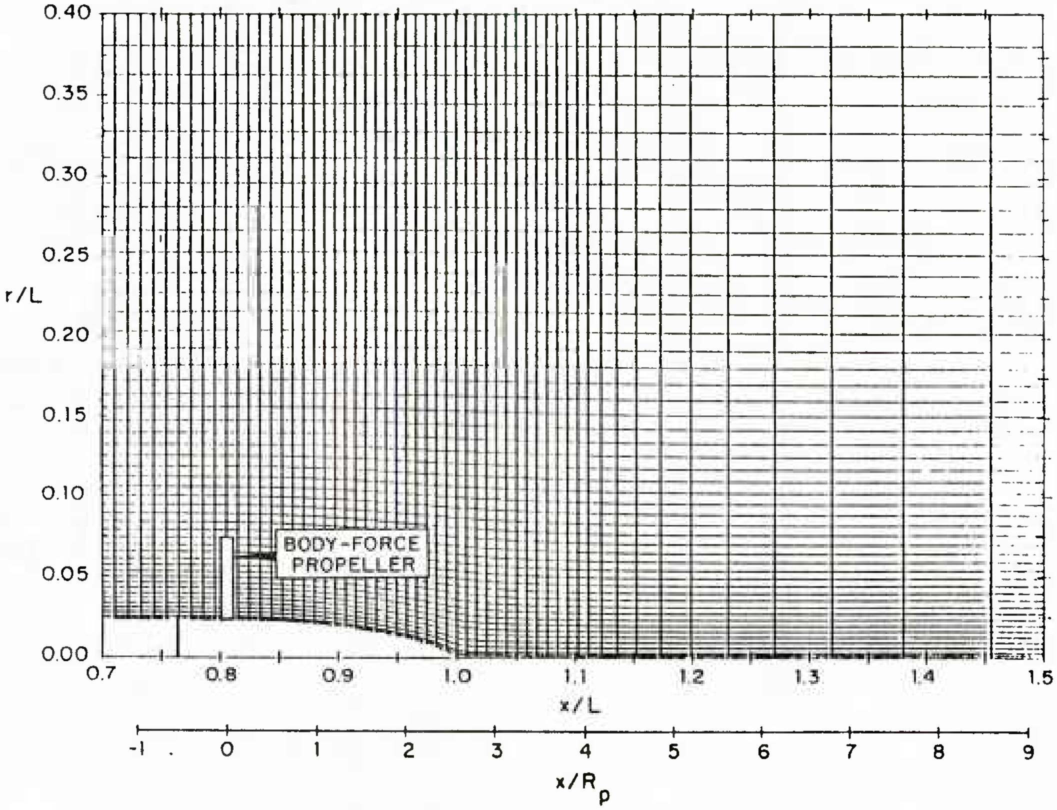

Figure 17. P4660 long hub grid (partial view)

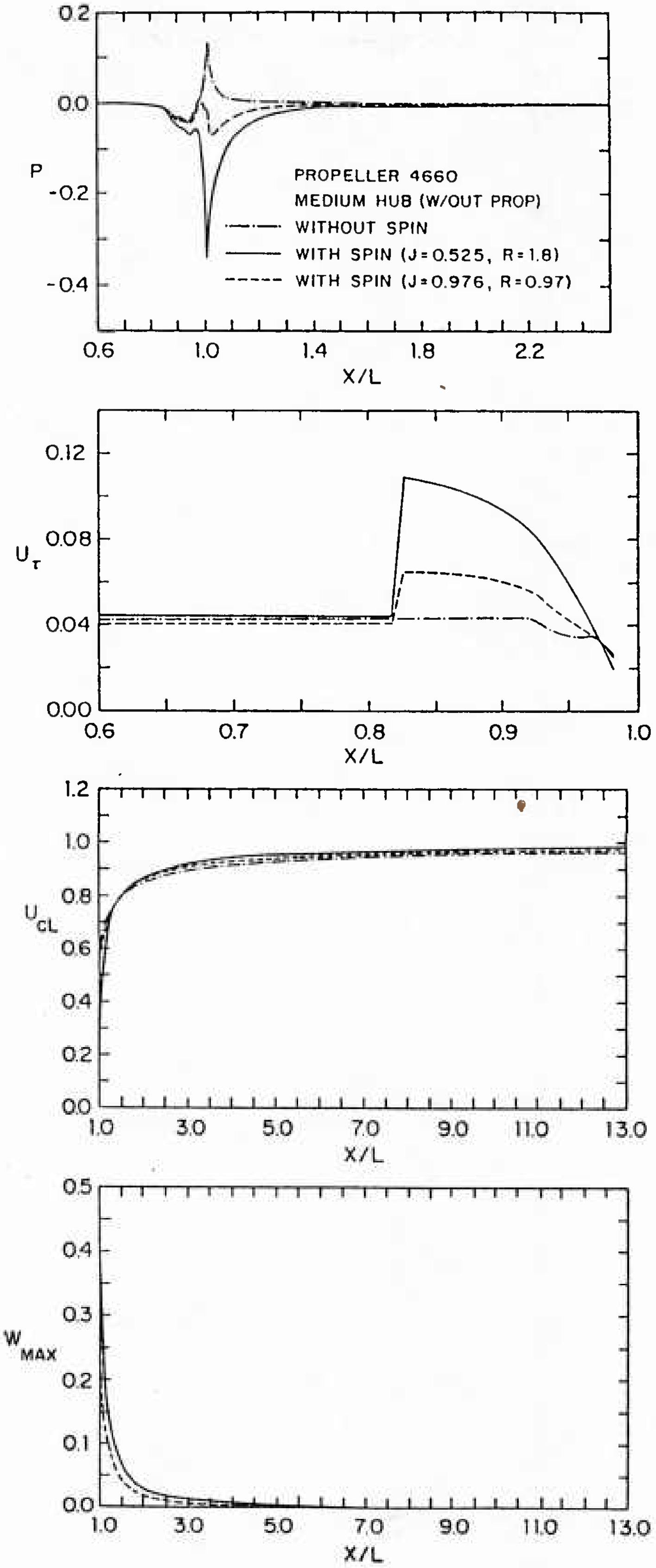

Figure 18. Body surface and wake centerline pressure, and wall-shear, wake centerline, and maximum swirl velocities (without propeller)

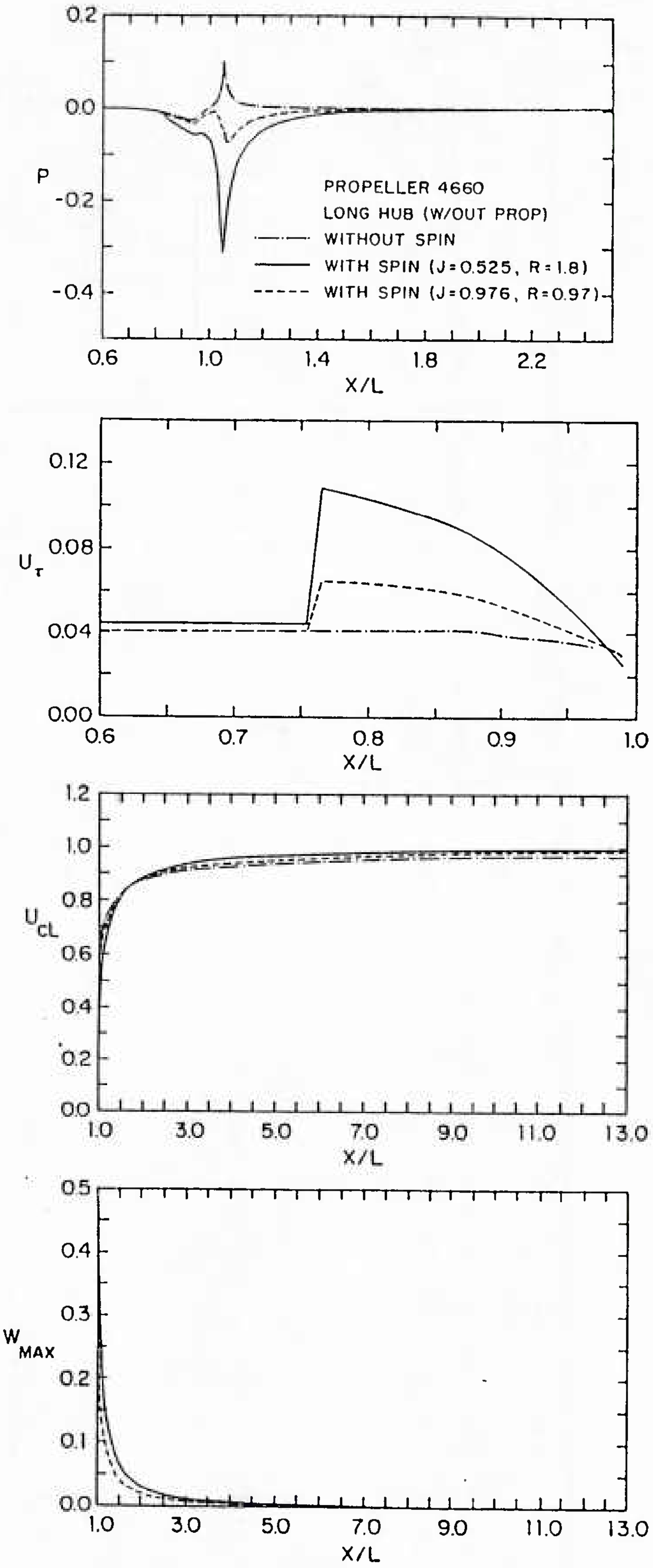

Figure 19. Body surface and wake centerline pressure, and wall-shear, wake centerline, and maximum swirl velocities (without propeller)

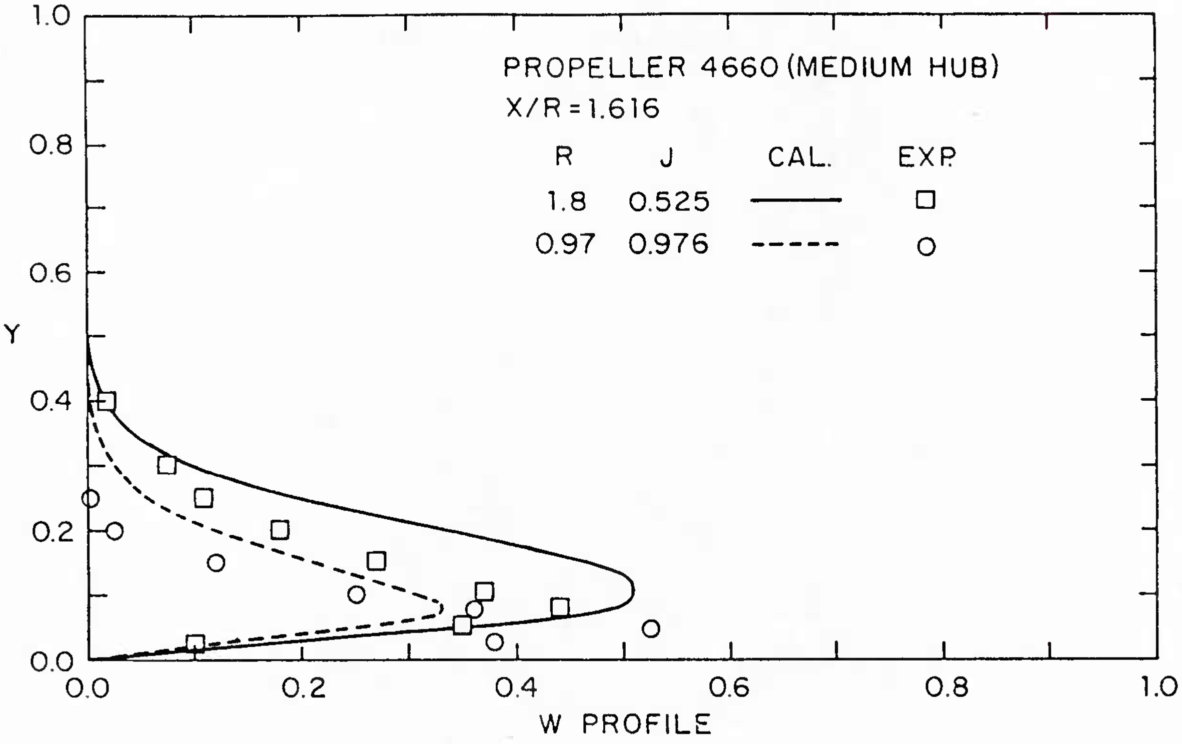

Figure 20. Swirl velocity profile (without propeller)

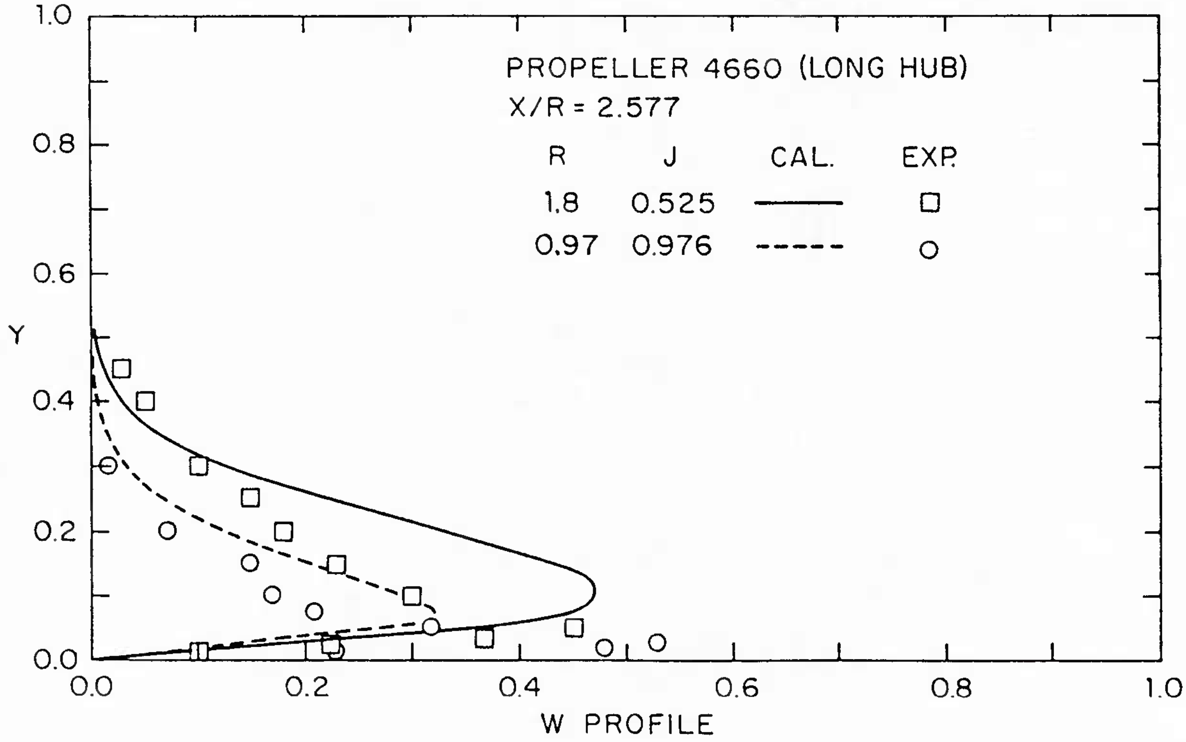

Figure 21. Swirl velocity profile (without propeller)

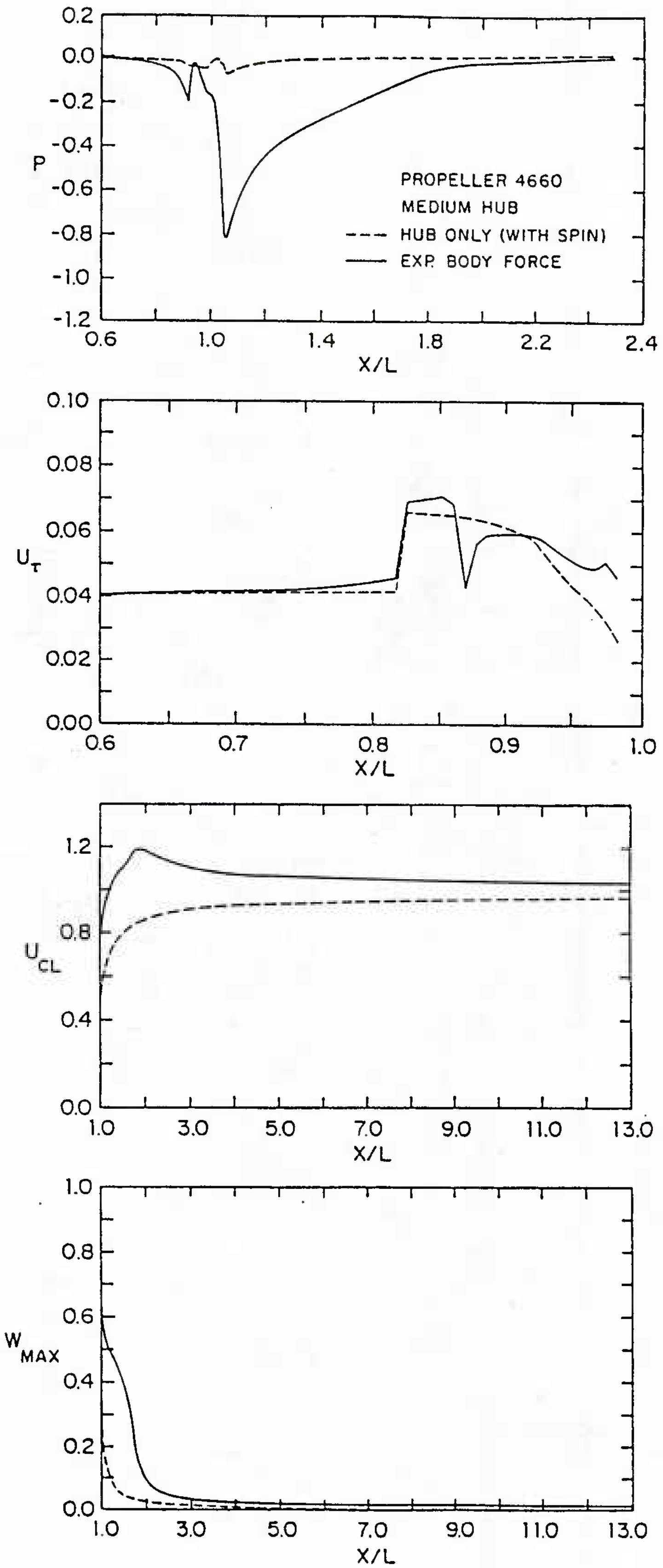

Figure 22. Body surface and wake centerline pressure, and wall-shear, wake centerline, and maximum swirl velocities (with propeller)

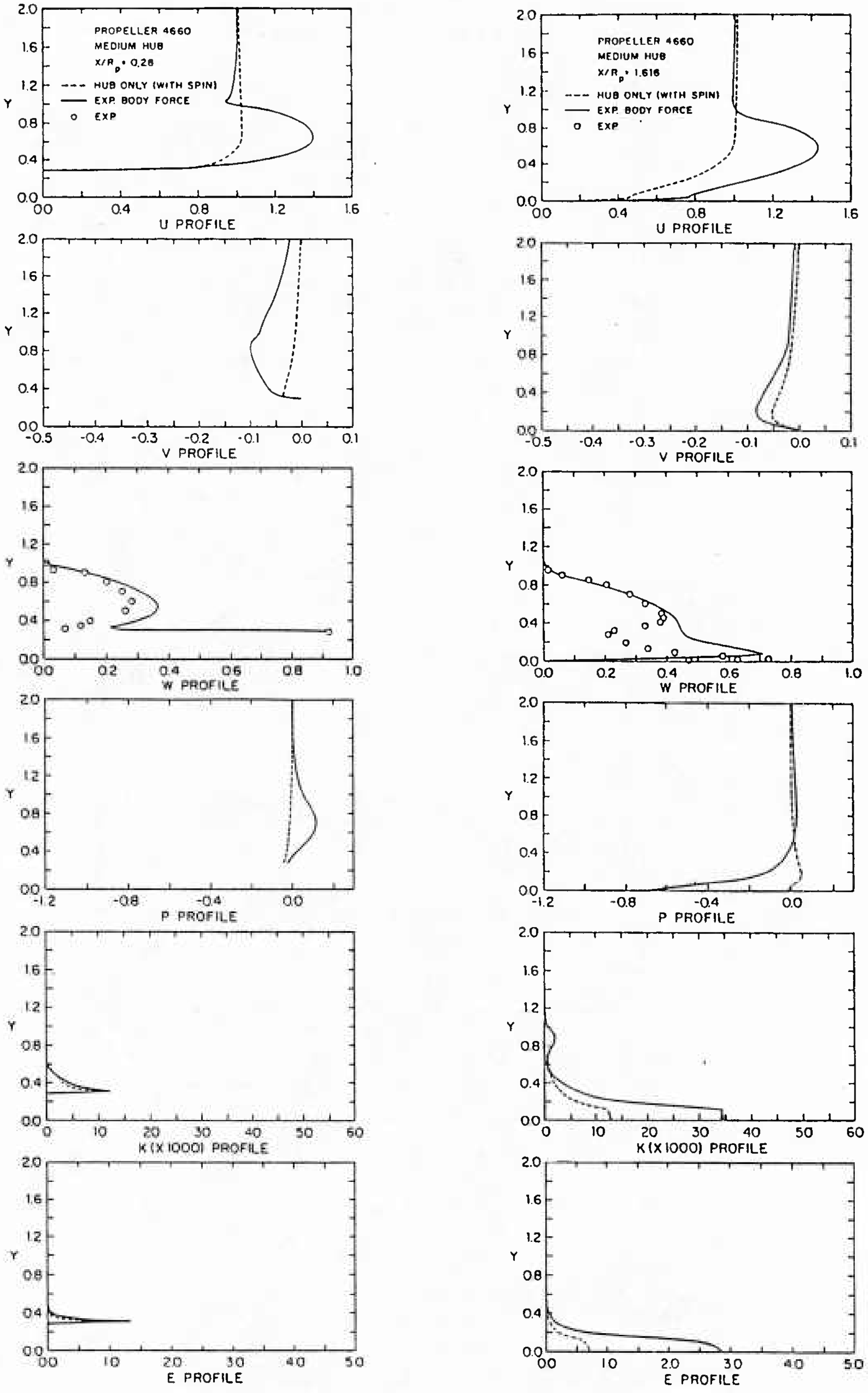

(a)

(b)

Figure 23. Velocity, pressure, and turbulence parameter profiles (with propeller)

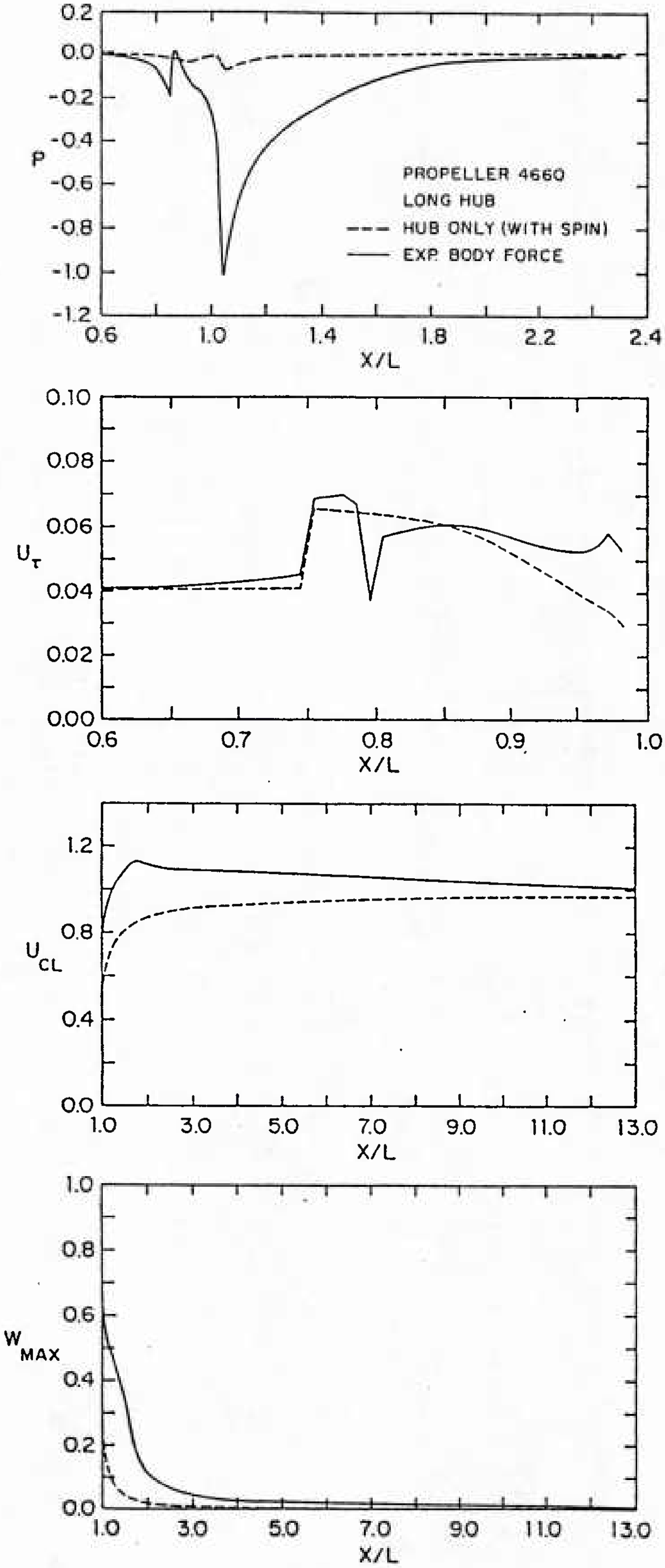

Figure 24. Body surface and wake centerline pressure, and wall-shear, wake centerline, and maximum swirl velocities (with propeller)

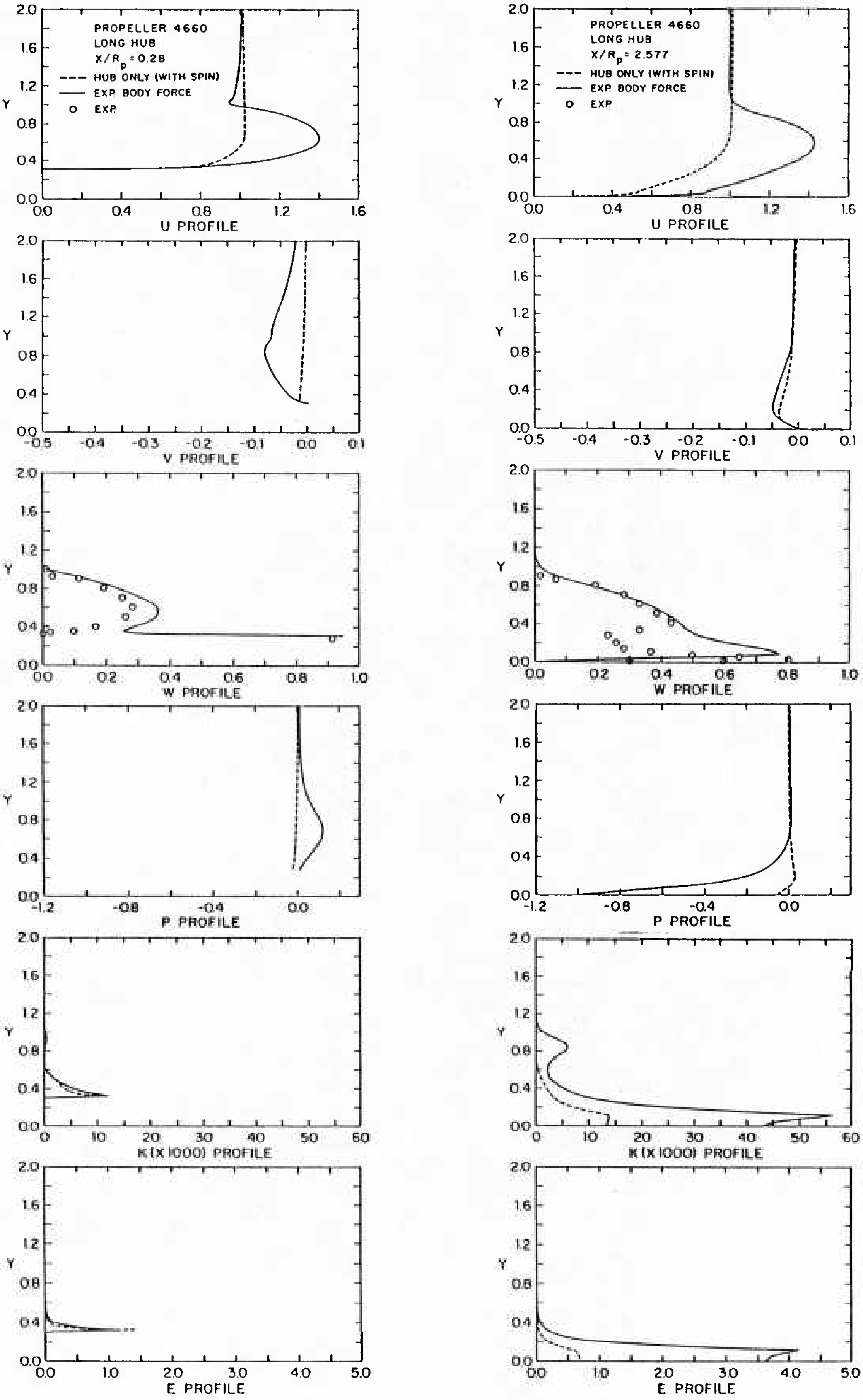

(a) (b)

Figure 25. Velocity, pressure, and turbulence parameter profiles (with propeller)

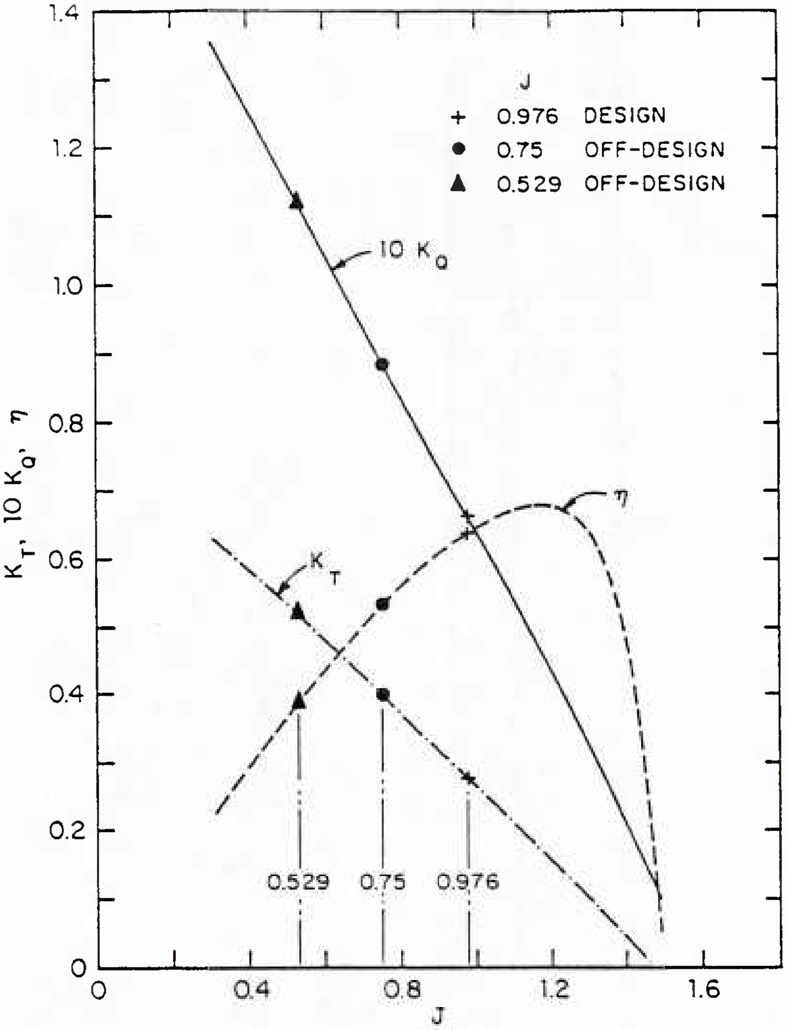

Figure 26. Propeller P4660 open-water curves

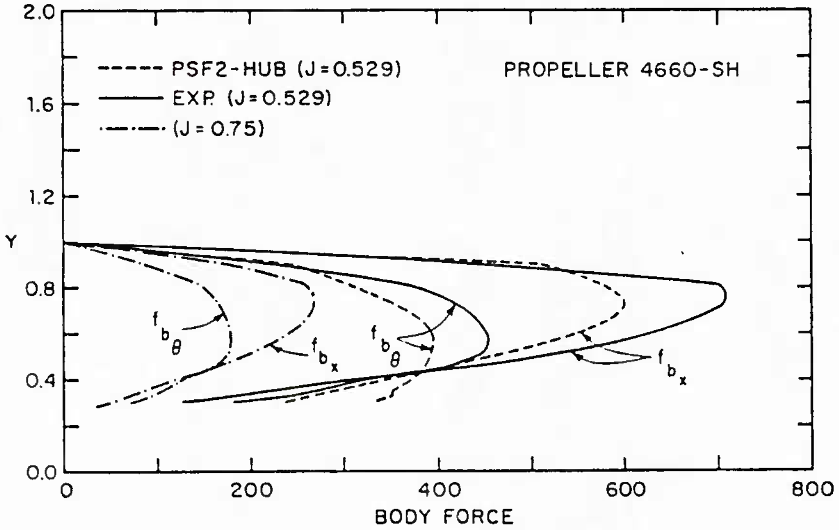

Figure 27. Body-force distributions

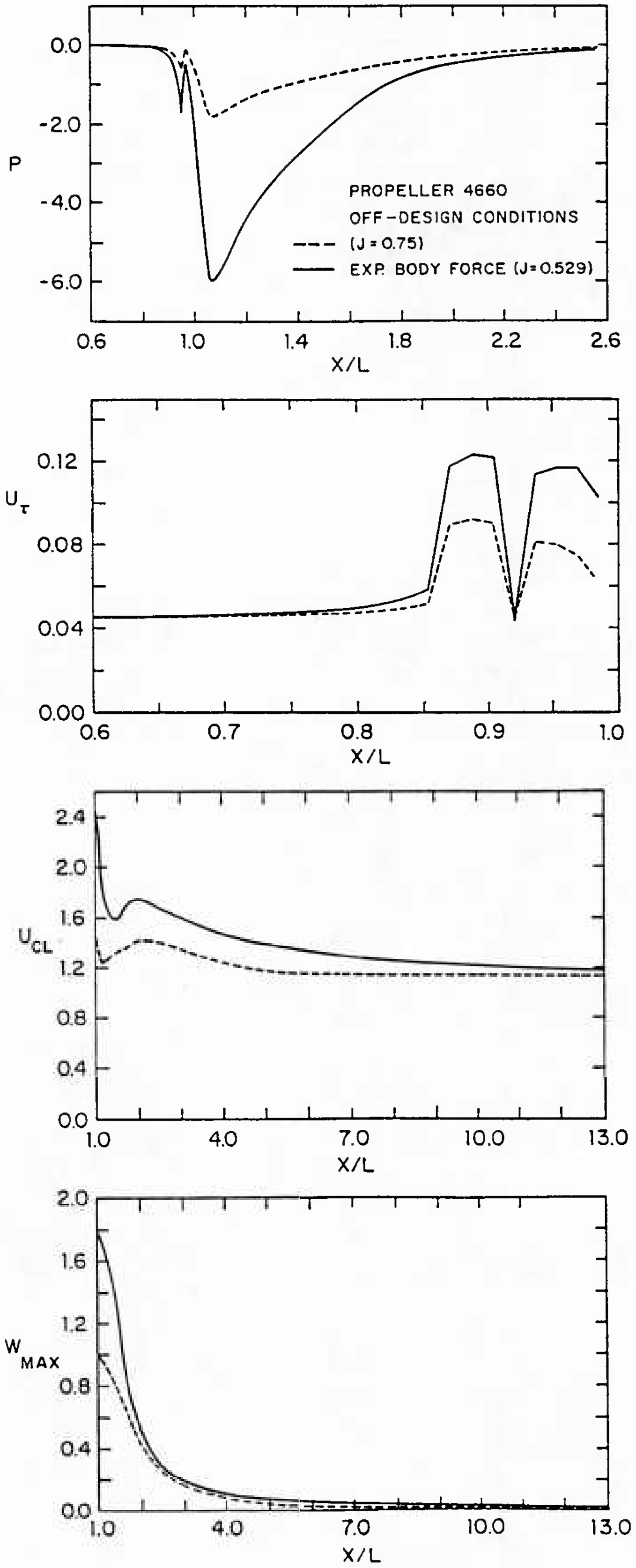

Figure 28. Body surface and wake centerline pressure, and wall-shear, wake centerline, and maximum swirl velocities (with propeller)

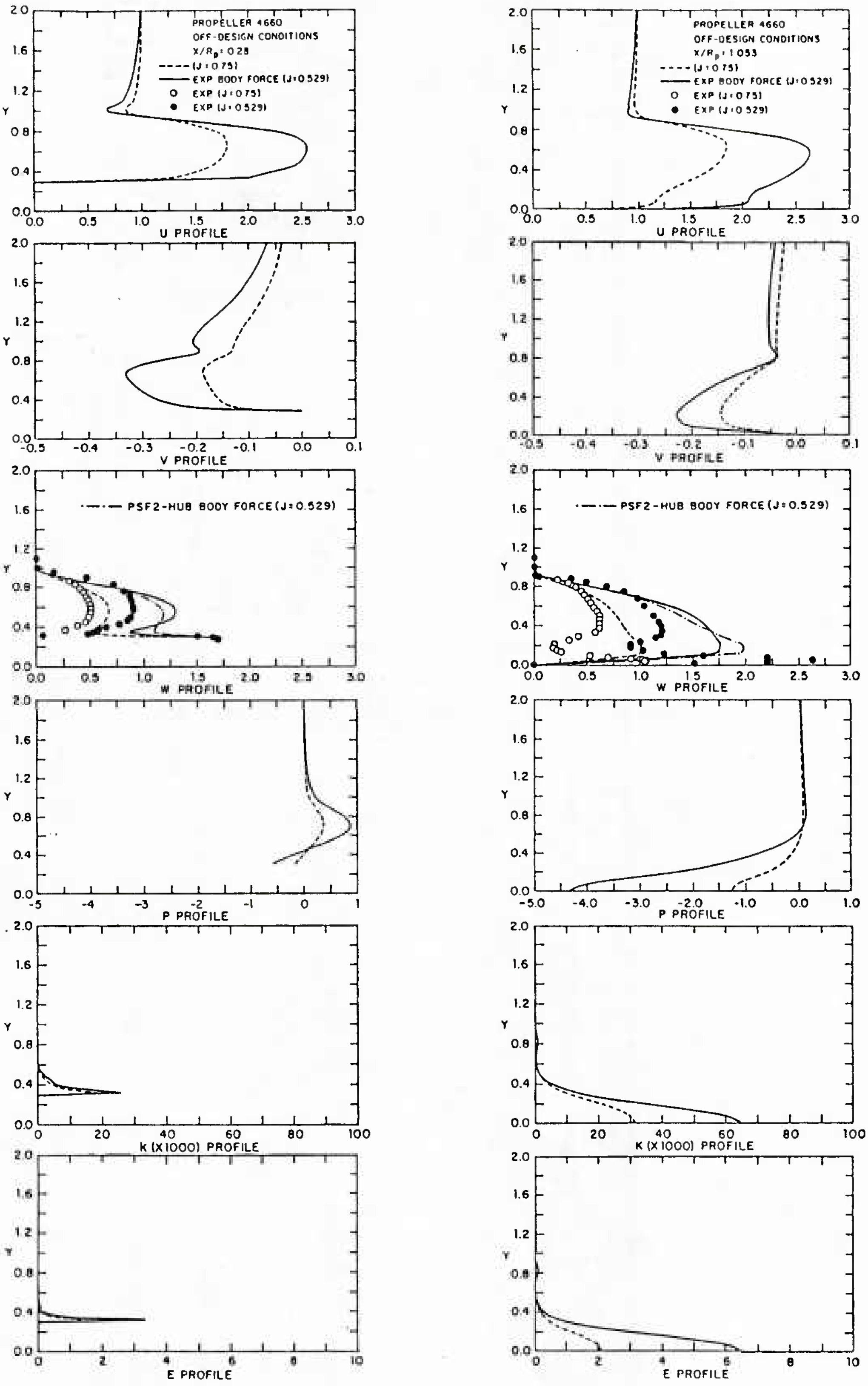

(a)

(b)

Figure 29. Velocity, pressure, and turbulence parameter profiles (with propeller)

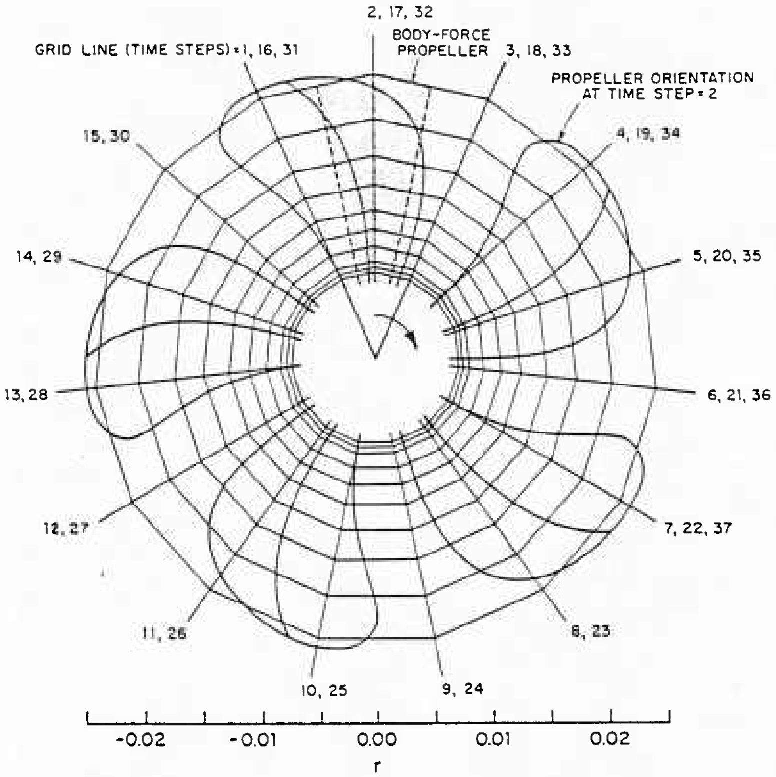

Figure 30. Unsteady-flow coarse cross-sectional grid and propeller representation (partial view)

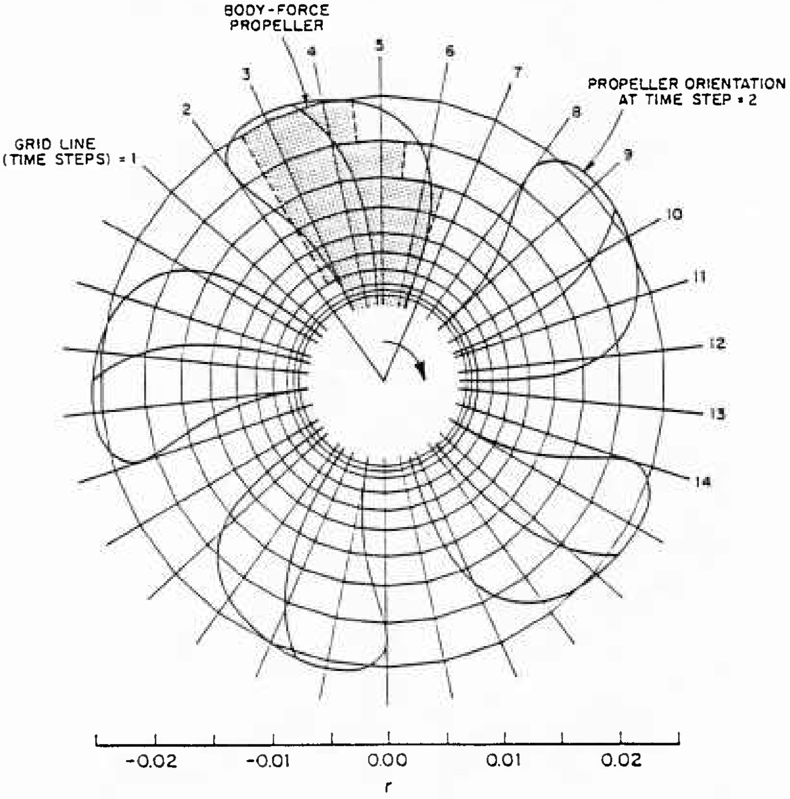

Figure 31. Unsteady-flow fine cross-sectional grid and propeller representation (partial view)

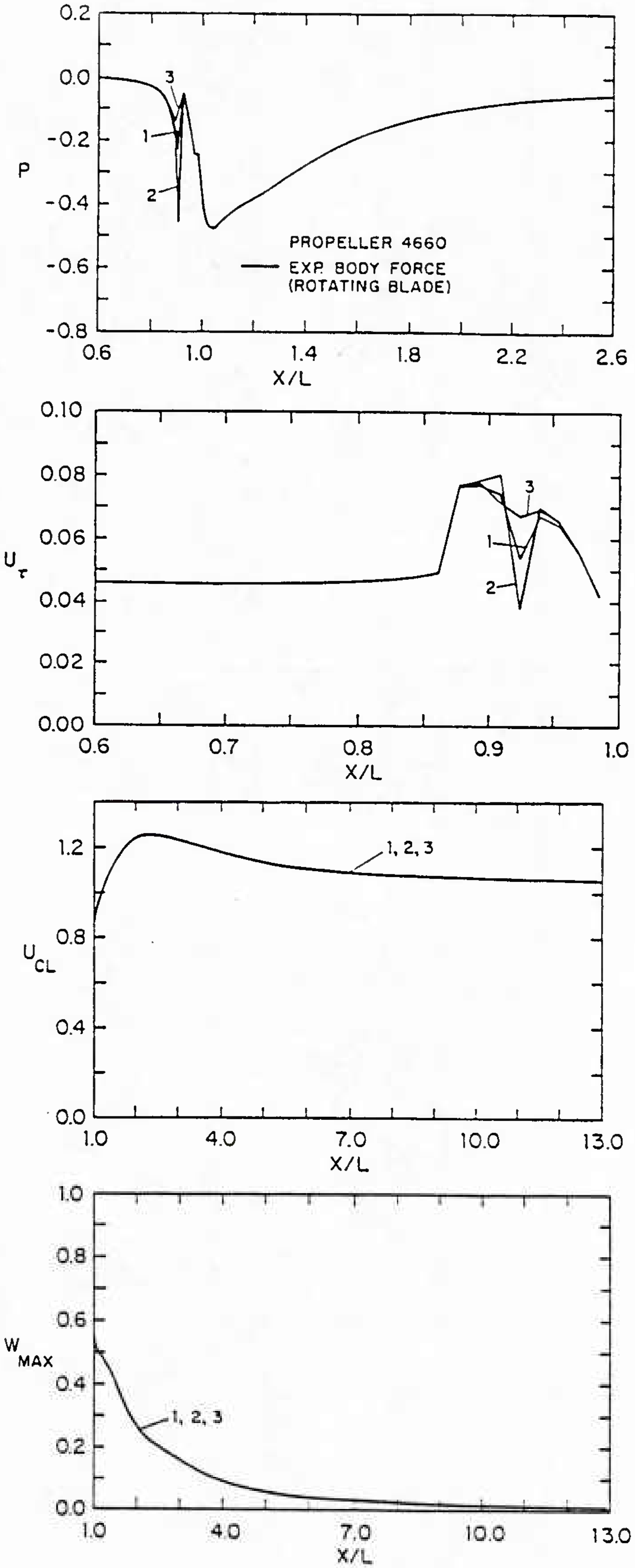

Figure 32. Body surface and wake centerline pressure, and wall-shear, wake centerline, and maximum swirl velocities (with propeller)

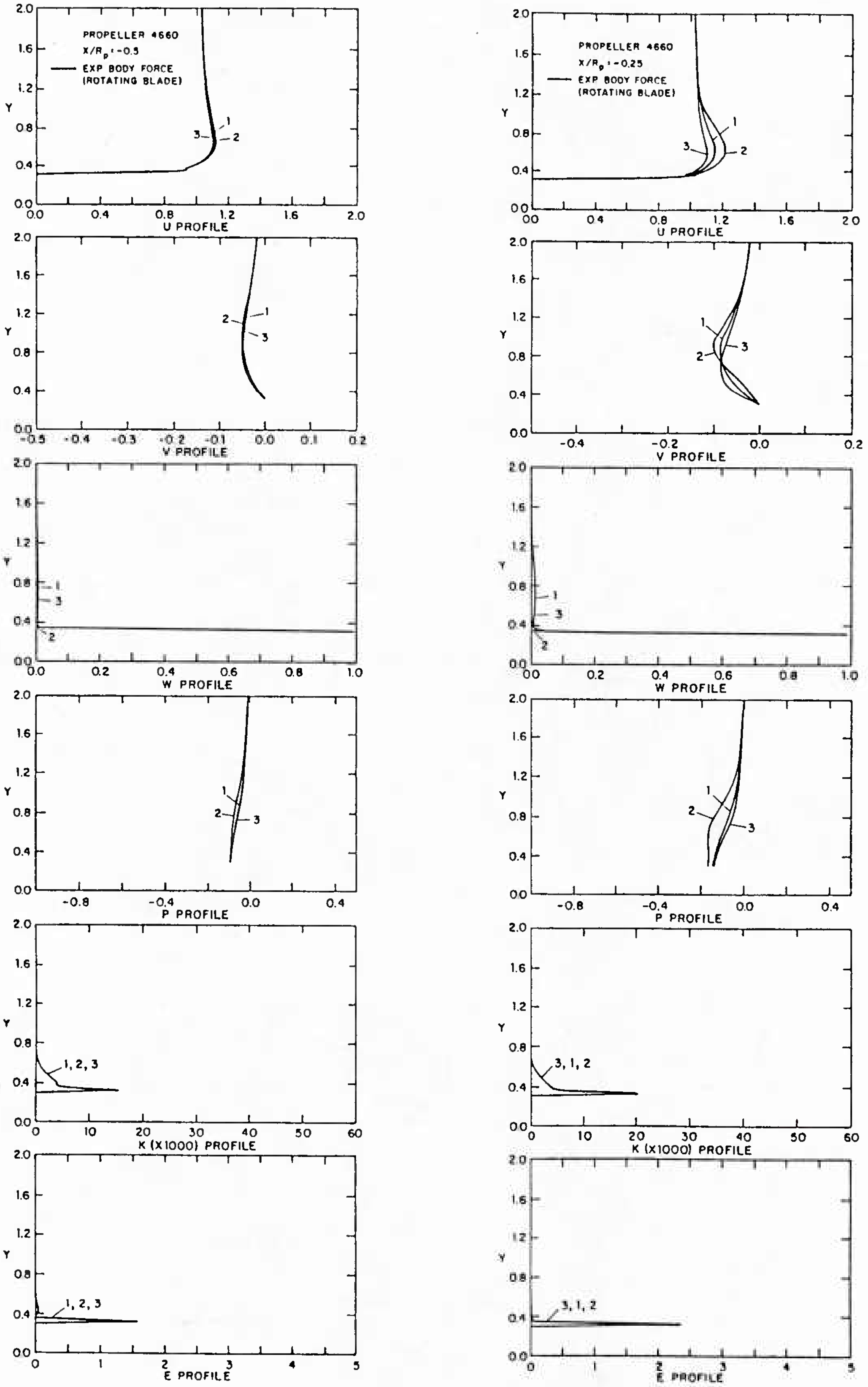

(a)

(b)

Figure 33. Velocity, pressure, and turbulence parameter profiles (with propeller)

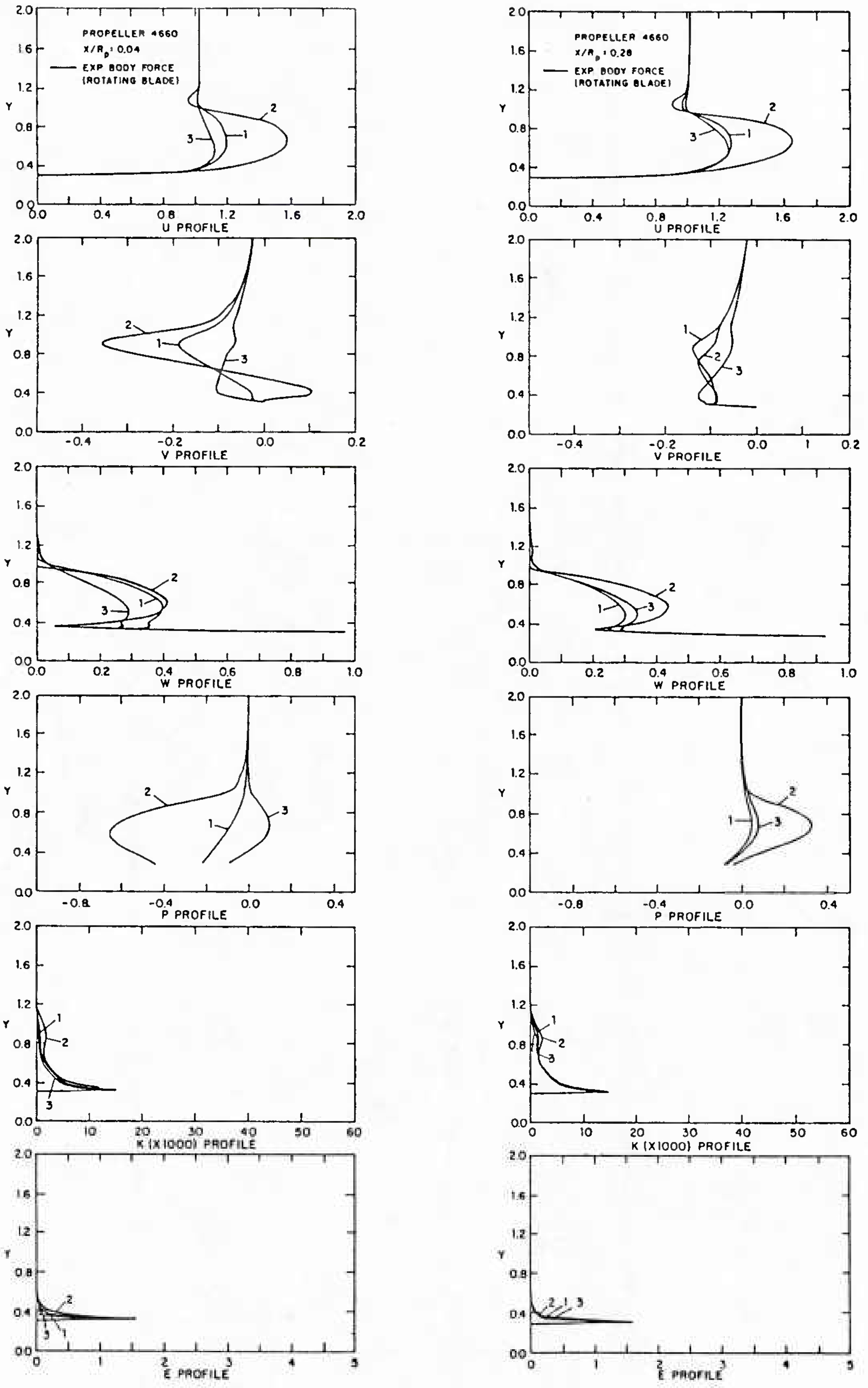

(c)

(d)

Figure 33. (continued)

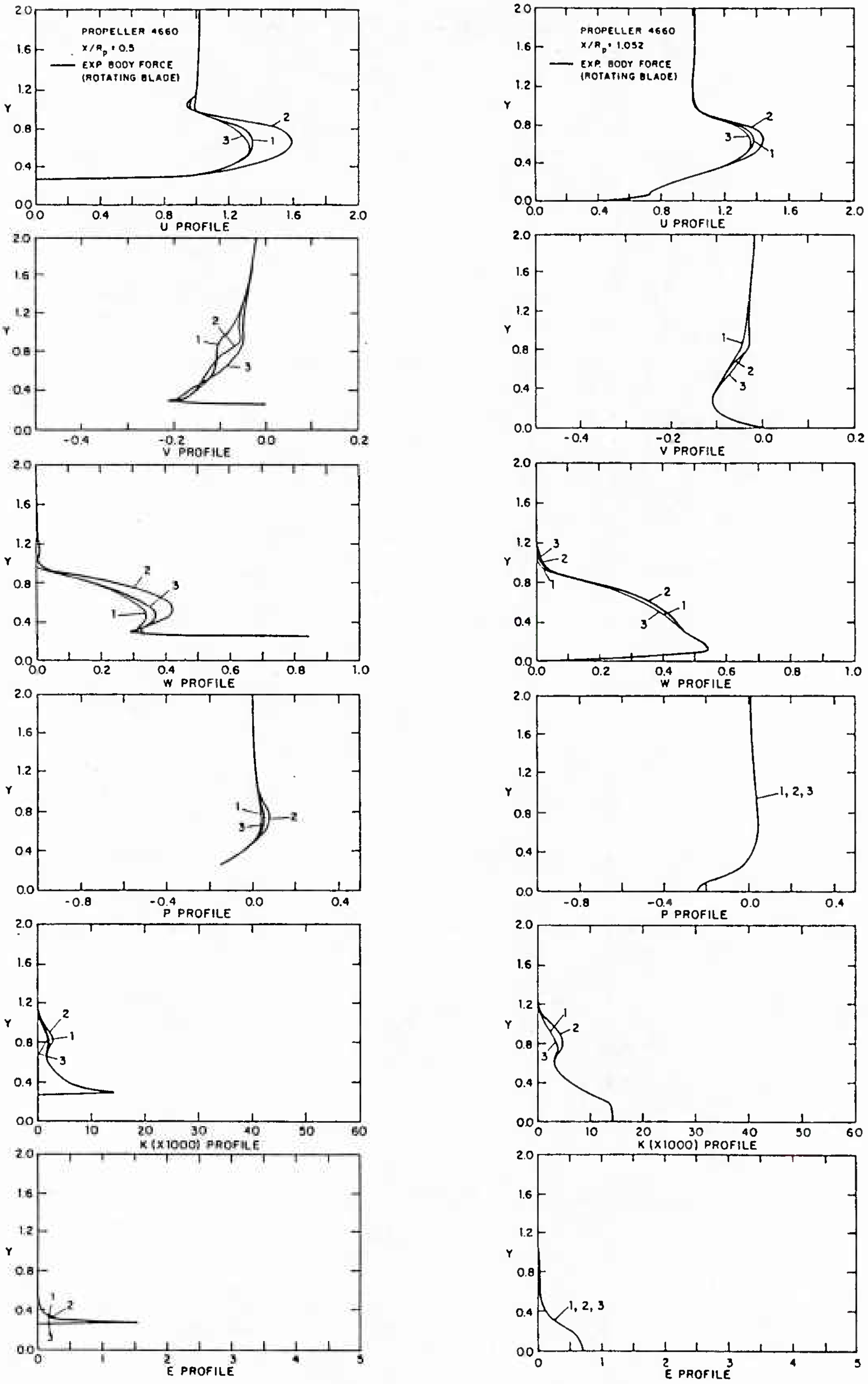

(e)

(f)

Figure 33. (continued)

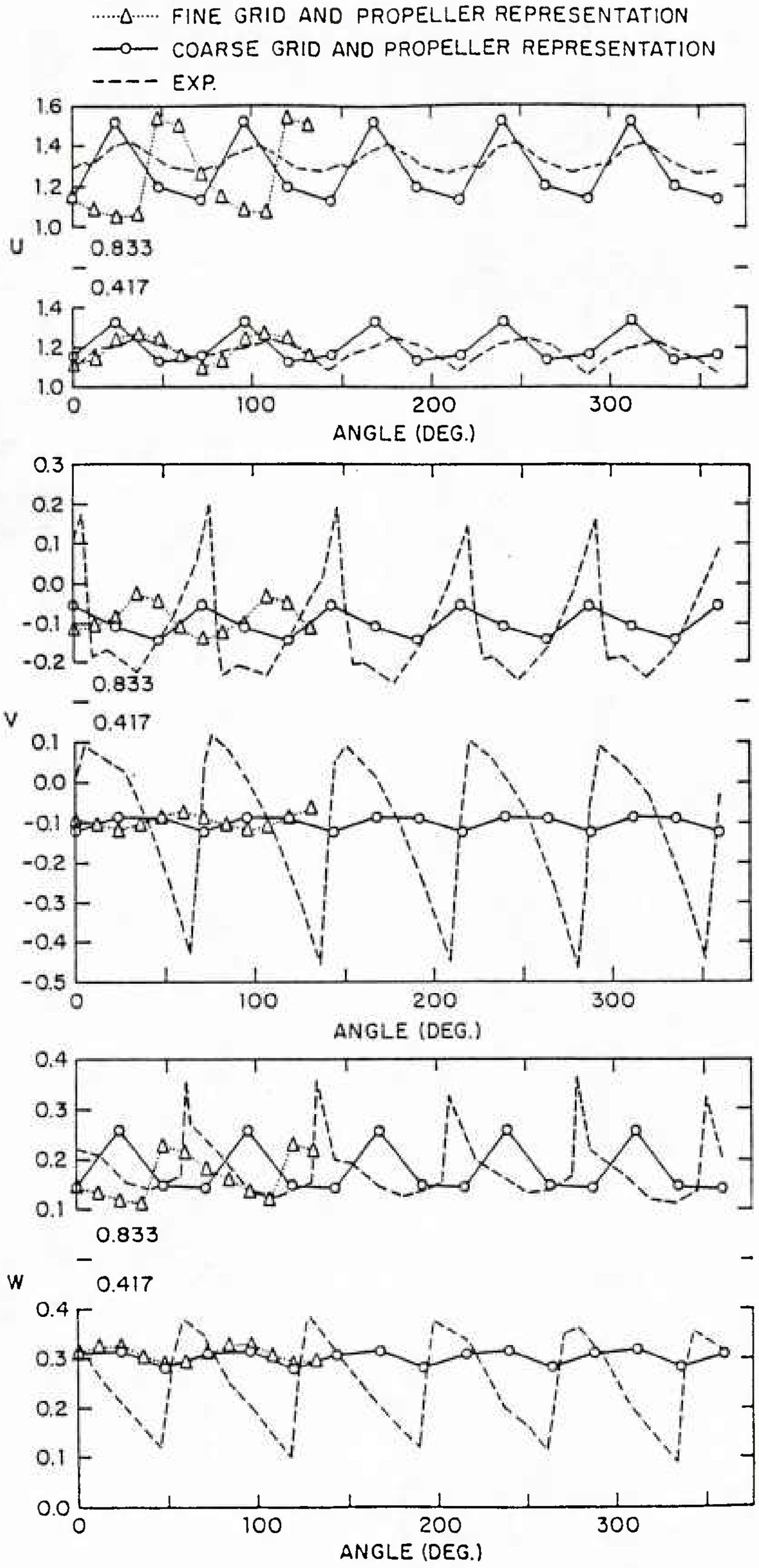

Figure 34. Time history of the velocity components at $x/r_p = .28$

DISTRIBUTION LIST FOR TECHNICAL REPORTS
ONR FLUID DYNAMIC PROGRAM (HYDRODYNAMICS)

Defense Technical Information Center
Information Facility
Alexandria, VA 22314
12 copies

NASA Scientific and Technical
Information Facility
P.O. Box 8757
Baltimore/Washington International Airport
Maryland 21240

Office of Naval Research
Code 432F
800 N. Quincy Street
Arlington, VA 22217
3 copies

Librarian
University of California
Department of Naval Architecture
and Offshore Engineering
Berkeley, CA 94720

Professor Bruce Johnson
U.S. Naval Academy
Hydromechanics Laboratory
Annapolis, MD 21402

Library
David Taylor Naval Ship Research
and Development Center
Code 522.1
Bethesda, MD 20084

Library
U.S. Naval Academy
Annapolis, MD 21402

The Society of Naval Architects and
Marine Engineers
One World Trade Center, Suite 1369
New York, NY 10048

Technical Library
Webb Institute of Naval Architecture
Glen Cove, NY 11542

Technical Library
Naval Coastal System Center
Panama City, FL 32401

Library
Stevens Institute of Technology
Davidson Laboratory
Castle Point Station
Hoboken, NJ 07030

Technical Library
Naval Ship Engineering Center
Philadelphia Division
Philadelphia, PA 19112

R.E. Gibson Library
The Johns Hopkins University
Applied Physics Laboratory
Johns Hopkins Road
Laurel, MD 20810

Editor
Applied Mechanics Review
Southwest Research Institute
8500 Culebra Road
San Antonio, TX 78206

Lorenz G. Straub Library
University of Minnesota
St. Anthony Falls Hydraulic Laboratory
Minneapolis, MN 55414

Technical Library
Naval Ocean Systems Center
San Diego, CA 92152

Library
Naval Postgraduate School
Monterey, CA 93940

Librarian
Naval Surface Weapons Center
White Oak Laboratory
Silver Spring, MD 20910

Technical Library
Naval Underwater Systems Center
Newport, RI 02840

Library
Department of Ocean Engineering
Massachusetts Institute of Technology
Cambridge, MA 01778

Engineering Societies Library
345 East 47th Street
New York, NY 10017

Library
Department of Naval Architecture
and Marine Engineering
University of Michigan
Ann Arbor, MI 48109

Librarian Station 5-2
Coast Guard Headquarters
NASSIF Building
400 Seventh Street, SW
Washington, DC 20591

Library
Applied Research Laboratory
The Pennsylvania State University
P.O. Box 30
State College, PA 16801

Library of Congress
Science and Technology Division
Washington, DC 20540

Library
Marine Physical Laboratory
Scripps Institution of Oceanography
University of California @ San Diego
San Diego, CA 92152

Dr. A.L. Slafkosky
Scientific Advisor
Commandant of the Marine Corps
Code AX
Washington, DC 20380

Library
Applied Research Laboratories
University of Texas at Austin
Austin, TX 78712

Maritime Administration
Office of Maritime Technology
14th & E Streets, NW
Washington, DC 20230

Library
Woods Hole Oceanographic Institution
Woods Hole, MA 02543

Maritime Administration
Division of Naval Architecture
14th & E Streets, NW
Washington, DC 20230

Professor Robert E. Falco
Michigan State University
Department of Mechanical Engineering
East Lansing, MI 48824

Naval Research Laboratory
Code 2627
Washington, DC 20375

Mr. Dennis Bushnell
NASA Langley Research Center
Langely Station
Hampton, VA 23365

Library
Naval Sea Systems Command
Code 09GS
Washington, DC 20362

Dr. A.K.M. Fazle Hussain
University of Houston
Department of Mechanical Engineering
Houston, TX 77004

Library
Institute of Hydraulic Research
The University of Iowa
Iowa City, IA 52242

Professor John L. Lumley
Cornell University
Sibley School of Mechanical and Aerospace
Engineering
Ithaca, NY 14853

Library
Southwest Research Institute
8500 Culebra Road
San Antonio, TX 78228

Professor W.W. Willmarth
The University of Michigan
Department of Aerospace Engineering
Ann Arbor, MI 48109

Professor A. Roshko
California Institute of Technology
Graduate Aeronautical Laboratories
Pasadena, CA 91125

Professor Stanley Corrsin
The Johns Hopkins University
Department of Chemical Engineering
Baltimore, MD 21218

Professor J.T.C. Liu
Brown University
Division of Engineering
Providence, RI 02912

Professor Patrick Leehey
Massachusetts Institute of Technology
Department of Ocean Engineering
Cambridge, MA 02139

Dr. W.C. Lin
Code 152
DTNSRDC
Bethesda, MD 20084

Professor Eli Reshotko
Case Western Reserve University
Department of Mechanical and
Aerospace Engineering
Cleveland, OH 44106

Mr. J.H. McCarthy
Code 154
DTNSRDC
Bethesda, MD 20084

Dr. Steven A. Orszag
Cambridge Hydrodynamics, Inc.
P.O. Box 1403
Princeton, NJ 08542

Mr. D.S. Cieslowski
Code 156
DTNSRDC
Bethesda, MD 20084

Professor Tuncer Cebeci
California State University
Mechanical Engineering Department
Long Beach, CA 90840

Mr. V.J. Monacella
Code 1504
DTNSRDC
Bethesda, MD 20084

Dr. C.W. Hirt
University of California
Los Alamos Scientific Laboratory
P.O. Box 1663
Los Alamos, NM 87544

Dr. B. Yim
Code 154.1
DTNSRDC
Bethesda, MD 20084

Dr. Hans Lugt
Code 1802
DTNSRDC
Bethesda, MD 20084

Dr. H. Haussling
Code 1843
DTNSRDC
Bethesda, MD 22084

Mr. W.C. Sandberg
Code 55W33
Naval Sea Systems Command
Washington, DC 20362

Prof. Marshall P. Tulin
Department of Mechanical and
Environmental Engineering
University of California at Santa Barbara
Santa Barbara, CA 93106

Mr. E.N. Comstock
Code 55W3
Naval Sea Systems Command
Washington, DC 20362

Prof. Jin Wu
College of Marine Studies
University of Delaware
Lewes, DE 19958

Dr. R.J. Hansen
Code 5844
Naval Research Laboratory
Washington, DC 20375

Prof. S.G. Rubin
Department of Aerospace Engineering
and Applied Mechanics
University of Cincinnati
Cincinnati, OH 45221

Dr. O.M. Griffin
Code 5841
Naval Research Laboratory
Washington, DC 20375

Professor S.F. Shen
Sibley School of Mechanical and
Aerospace Engineering
Cornell University
Ithaca, NY 14850

Dr. T.F. Zien
Code R44
Naval Surface Weapons Center
White Oak Lab.
Silver Spring, MD 20910

Prof. J.E. Kerwin
Department of Ocean Engineering
Massachusetts Institute of Technology
Cambridge, MA 01778

Dr. W.K. Blake
Code 1905.1
DTNSRDC
Bethesda, MD 20854

Prof. C.M. Ho
Department of Aerospace Engineering
University of Southern California
University Park
Los Angeles, CA 90007
2 copies

Dr. Do C. Kwak
Applied Computational Aerodynamics
Branch
NASA Ames Research Center
M/S 202A-14
Moffet Field, CA 94035

Prof. V.C. Patel
Institute of Hydraulic Research
The University of Iowa
Iowa City, IA 52242
2 copies

Prof. P.G. Saffman
Department of Applied Mathematics
California Institute of Technology
Pasadena, CA 91125

Dr. N. Salvesen
Science Applications, Inc.
134 Holiday Court, Suite 318
Annapolis, MD 21401

Prof. O.M. Phillips
Dept. of Earth & Planetary Science
Johns Hopkins University
Baltimore, MD 21218

Prof. P.M. Naghdi
Dept. of Mechanical Engineering
University of California
Berkeley, CA 94720

Dr. T.D. Taylor
Applied Physics Laboratory
Johns Hopkins University
Baltimore, MD 21218

Dr. T.T. Huang
Code 1542
DTNSRDC
Bethesda, MD 20084

Prof. W.G. Tiederman
School of Mechanical Engineering
Purdue University
West Lafayette, IN 47907

Prof. R.W. Yeung
Dept. of Naval Architecture
and Offshore Engineering
University of California
Berkeley, CA 94720
3 copies

Prof. R.L. Street
Dept. of Civil Engineering
Stanford University
Stanford, CA 94305

Prof. W.R. Schowalter
Dept. of Chemical Engineering
Princeton University
Princeton, NJ 08540

Prof. T. Maxworthy
Dept. of Mechanical Engineering
University of Southern California
University Park
Los Angeles, CA 90089-0192

Prof. J. Schetz
Dept. of Aerospace & Ocean Engineering
Virginia Polytechnic Institute and
State University
Blacksburg, VA 24061
2 copies

Prof. D. Rockwell
Dept. of Mechanical Engineering
and Mechanics
Lehigh University
Bethlehem, PA 18015

Dr. E.P. Rood
Code 1543
DTNSRDC
Bethesda, MD 20084

Prof. J.B. Keller
Dept. of Mathematics
Stanford University
Stanford, CA 94305

Prof. A.J. Acosta
Dept. of Mechanical Engineering
California Institute of Technology
Pasadena, CA 91125

Prof. J.N. Newman
Dept. of Ocean Engineering
Massachusetts Institute of Technology
Cambridge, MA 01778

Prof. J.E. Kerwin
Dept. of Ocean Engineering
Massachusetts Institute of Technology
Cambridge, MA 01778

Dr. S.J. Shamroth
Scientific Research Associates, Inc.
P.O. Box 498
Glastonburg, CT 06033

Prof. W.S. Vorus
Dept. of Naval Architecture and
Marine Engineering
University of Michigan
Ann Arbor, MI 48109

Prof. A.H. Nayfeh
Dept. of Engineering Sciences & Mechanics
Virginia Polytechnic Institute and
State University
Blacksburg, VA 24061

Prof. T.Y. Wu
Dept. of Engineering Science
California Institute of Technology
Pasadena, CA 91125

Prof. C.C. Mei
Dept. of Civil Engineering
Massachusetts Institute of Technology
Cambridge, MA 02139

Prof. S.A. Berger
Dept. of Mechanical Engineering
University of California
Berkeley, CA 94720

Prof. J.W. Miles
Dept. of Geophysics
University of California
La Jolla, CA 92093

Dr. J.H. Duncan
Flow Research Company
1320 Fenwick Lane, Suite 401
Silver Spring, MD 20910

Prof. C.E. Brennen
Dept. of Mechanical Engineering
California Institute of Technology
Pasadena, CA 91125

Prof. R.F. Beck
Dept. of Naval Architecture and
Marine Engineering
University of Michigan
Ann Arbor, MI 48109

Prof. T. Sarpkaya
Dept. of Mechanical Engineering
Code 69-SL
Naval Postgraduate School
Monterey, CA 93940

Dr. D. Savitsky
Davidson Laboratory
Stevens Institute of Technology
Hoboken, NJ 07030
2 copies